Dipl.–Ing. Thomas Wiener

Analysis of Cardiac Near Field Signals

DISSERTATION

zur Erlangung des akademischen Grades eines Doktors der technischen Wissenschaften

erreicht an der

Technischen Universität Graz

Univ.–Prof. Dipl.–Ing. Dr.techn. Georg Brasseur
Institut für Elektrische Meßtechnik und Meßsignalverarbeitung
Technische Universität Graz

Ao. Univ.–Prof. Dipl.–Ing. Dr.techn. Ernst Hofer
Institut für Biophysik
Medizinische Universität Graz

Graz, im März 2012

Kurzfassung

Das kardiale elektrische Nahfeld (CNF) ist ein zeitvariantes elektrisches Feld, das sich aus Potentialdifferenzen an der Herzoberfläche ergibt. Diese Potentialdifferenzen entstehen durch die elektrische Erregung des darunter liegenden Gewebes. Extrazelluläre Potentialdifferenzen, nahe der Herzoberfläche mit hoher räumlicher und zeitlicher Auflösung gemessen, sogenannte CNF-Signale, ermöglichen die Charakterisierung des Erregungsmusters. Damit können Regionen mit mikrostrukturellen Heterogenitäten, welche potentielle Substrate für die Entstehung von Herzrhythmusstörungen darstellen, identifiziert werden. Das Ziel dieser Arbeit ist die Charakterisierung lokaler Erregungsausbreitung anhand der Analyse von CNF-Signalen, die in elektrophysiologischen in-vitro Experimenten mit Herzpräparaten aufgenommen werden. Spezielles Augenmerk wird auf die Analyse fraktionierter CNF-Signale gelegt, welche auf heterogene Struktur des darunter liegenden Herzgewebes hindeuten. Algorithmen für die Analyse von CNF-Signalen werden mithilfe von Signalverläufen aus Computersimulationen von virtuellem Herzgewebe entwickelt. Um deren Robustheit zu testen, wird Rauschen mit der gleichen Charakteristik wie unter experimentellen Bedingungen hinzugefügt. Die wichtigsten Ergebnisse sind die zuverlässige Berechnung der lokalen Ausbreitungsgeschwindigkeit, die Einführung eines quantitativen Maßes für die Fraktionierung von CNF-Signalen und die Zerlegung fraktionierter Signale in nichtfraktionierte Komponenten. Abschließend wird ein neuartiger Ansatz zur Klassifikation von kardialer Fibrose basierend auf der Analyse von CNF-Signalen präsentiert.

Abstract

The cardiac electric near field (CNF) is a time-varying electric field formed by potential differences at the surface of the heart muscle, which result from the sequence of electrical activation in the underlying tissue. Extracellular potentials measured close to the surface of the heart tissue with high spatial and temporal resolution, termed CNF signals, enable characterizing the pattern of activation. This may allow the identification of regions containing microstructural heterogeneities which are seen as potential substrates for the genesis of arrhythmias. The aim of this work is the characterization of local propagation of activation by analysis of CNF signals recorded during electrophysiological in-vitro experiments with heart preparations. Special emphasis is placed on the analysis of fractionated CNF signals which are attributed to heterogeneous structure in the underlying heart tissue. Algorithms for the processing of CNF signals are developed using waveforms obtained from computer simulations of virtual heart tissue. To test their robustness, noise of the same characteristics as observed under experimental conditions was added. The main findings are the reliable computation of local conduction velocity, the introduction of a quantitative measure of CNF signal fractionation, and the decomposition of fractionated signals into nonfractionated components. Moreover, a novel approach to the classification of cardiac fibrosis through the analysis of CNF signals is presented.

Contents

Nomenclature

Abbreviations

ADC	analog-to-digital converter
ANR	amplitude-to-noise ratio
AP	action potential
APD	action potential duration
CNF	cardiac electric near field
CV	conduction velocity
DAQ	data acquisition
HARMS	high performance arrhythmia research measurement system
LAT	local activation time
LCV	local conduction velocity
LP	longitudinal elliptic propagation
MAP	monophasic action potential
OP	oblique elliptic propagation
PLA	planar propagation
PSD	power spectral density
SNR	signal-to-noise ratio
TP	transverse elliptic propagation

Operators, Functions, and Indices

$\nabla(\dots)$	nabla operator
$y = f(x)$	y is a function of x
$\hat{\boldsymbol{x}}$, $\boldsymbol{x}_p$, $\boldsymbol{x}_{max}$, $\max \boldsymbol{x}$	maximum of vector $\boldsymbol{x}$
$\boldsymbol{x}_{min}$, $\min \boldsymbol{x}$	minimum of vector $\boldsymbol{x}$
$\boldsymbol{x}_{pp}$	peak-to-peak amplitude of vector $\boldsymbol{x}$
$\dot{\boldsymbol{x}}$	derivative of $\boldsymbol{x}$ with respect to time
$\ddot{\boldsymbol{x}}$	second derivative of $\boldsymbol{x}$ with respect to time
$\mathrm{\|x\|}$	absolute value of x
$\Delta\mathrm{x}$	difference between two values of x, e.g. $\Delta\mathrm{x} = \mathrm{x}_1 - \mathrm{x}_2$
$\Delta\boldsymbol{x}$	range of vector $\boldsymbol{x}$, $\Delta\boldsymbol{x} = \max \boldsymbol{x} - \min \boldsymbol{x}$
$\boldsymbol{x}^T$	transposed of vector $\boldsymbol{x}$

Greek Letters

α, β	deflection angle
α	crossing angle of two muscle fibers
ζ	phase angle of power line interference
θ	magnitude of the velocity of main propagation
θ_l	magnitude of the longitudinal local conduction velocity
θ_t	magnitude of the transversal local conduction velocity
$\boldsymbol{\theta}$	vector of local conduction velocity
μ	arithmetic mean
ξ	normalized range
σ	standard deviation
φ	angle of the main propagation
Φ	electric potential
Φ_{exp}	Φ obtained from experiment
Φ_m	Φ obtained from analytic signal model
Φ_{sim}	Φ obtained from computer simulation
$\boldsymbol{\Phi}$	multivariate cardiac near field signal
$\tilde{\Phi}$	power line interference signal

Symbols

a, b, c, d	parameters of analytic signal model
a, b	symmetry factor
A, B	peak-to-peak amplitude of Φ
A	amplifier gain
acc	classification accuracy
d	distance
d	measurement grid length
DD	diagonal inter-electrode distance
e	deviation
$\boldsymbol{E}$	vector of electric field strength
E_x	x-component of $\boldsymbol{E}$
E_y	y-component of $\boldsymbol{E}$
f	frequency
f_C	filter cutoff frequency
f_S	sampling frequency
g_I	intracellular conductivity
M	interpolation factor
M	number of stimulus sites
n	number of iterations of the decomposition procedure
n	sample size
N	window length
q	voltage resolution of ADC
r	Pearson product-moment correlation coefficient
s	distance
sse	sum of the squared errors
t	time
t_{dep}	depolarization time
t_W	window duration
T_S	sampling interval
V_m	transmembrane voltage
$\boldsymbol{V}_m$	multivariate transmembrane voltage
x, x	distance, usually in fiber direction
y, y	distance, usually perpendicular to fiber direction
z	distance from the surface of the tissue

Chapter 1

Introduction

1.1 Motivation

Cardiac arrhythmias are widespread life-threatening diseases and their prevalence is expected to increase with increasing life expectancy. They arise from impaired generation of electrical activation or disturbances in its propagation through the heart muscle. Increased heterogeneity in the microscopic structure of the heart muscle causes complex local propagation which promotes arrhythmogenesis. The study of microscopic propagation of electrical activation in the heart muscle (micropropagation) has therefore been an important topic in basic research and is very likely to get increased importance in clinical application.

One approach to the investigation of micropropagation is the measurement and analysis of extracellular potentials acquired in the electric field close to the surface of the heart, the so-called *cardiac electric near field* (CNF). Computer simulation studies have demonstrated that these CNF signals can provide information about the micropropagation in the tissue beneath the recording point.

The aim of this work is to examine and characterize micropropagation through CNF signals recorded during electrophysiological in-vitro experiments with heart preparations.

1.2 Overview of the Following Chapters

The work is divided into two parts. Part I comprises the electrophysiological and technical background of the analysis of cardiac near field signals and the description of experimental and computer simulation setups.
In Chapter 2, the electrophysiological background of cardiac activation and its propagation across the heart muscle is outlined. Methods for measurement and computer simulation

of cardiac impulse propagation are presented.
A description of origin and properties of CNF signals is given in Chapter 3. Parameters extracted from CNF signals are specified and the class of fractionated local electrograms is introduced.
Chapter 4 gives a description of the experimental setup and applied methods.
Based on the state-of-the-art in cardiac near field technique, aims of this work are specified in Chapter 5.

In Part II, the performed studies on analysis of CNF signals are specified. This Part is divided into Introduction (Chapter 6), Methods (Chapter 7), Results (Chapter 8), and Discussion (Chapter 9).
The last Chapter (10) summarizes the main findings and gives an outlook on possible further research in this field.

Part I

Background

Chapter 2

Propagation of Activation in Myocardium

This Chapter gives an overview of basic principles of cardiac electrophysiology and introduces electrophysiological terms used throughout this work. First, it is described how cardiac muscle cells are electrically activated and how this activation propagates across the heart muscle (myocardium). Electrical signals which represent these processes are introduced and methods to measure them are presented and compared. Finally, it is shown how computer models are being utilized to simulate cardiac activation and impulse propagation.

2.1 Cardiac Activation and Impulse Propagation

The contraction of a heart muscle cell (cardiomyocyte) is triggered by an electrical impulse[1]. The propagation of this activation and the following contraction and recovery of the cardiomyocytes in a controlled sequence results in the pumping function of the heart. A normal heart beat is initiated in the sinoatrial node, the primary pacemaker area located in the right atrium[2]. The impulse spreads from cell-to-cell activating the working myocytes of the atria and is conducted via the atrioventricular node[3] and the specialized cardiac conduction system to the ventricles from where the activation propagates across the working myocytes of the ventricles. The specialized cardiac conduction system consists of the His-bundles and the Purkinje fibers which ensure the fast conduction of the

---

[1] In electrophysiological literature, the transient alteration in transmembrane voltage (see Figure 2.1) is referred to as *impulse*.

[2] Recent anatomical and electrophysiological studies have proven that the sinoatrial node is a rather elongated area spreading across the terminal crest. [1, 2, 3].

[3] The atrioventricular node is the only electrical connection between atria and ventricles. There, the impulse propagation is delayed to allow the contraction of the atria to fill the ventricles with blood. Furthermore, the frequency of ventricular activation in case of atrial arrhythmias is limited.

activation impulse to many locations in the ventricles. Then the activation spreads across the working myocardium from cell-to-cell.

2.1.1 Activation of a Single Cardiomyocyte

The heart consists of the following types of excitable myocytes: working muscle cells, specialized conduction cells, and pacemaker cells. Cardiac myocytes have an elongated cylindric shape with a length of 50-120 μm and a diameter of approximately 5-25 μm. The size of the cells varies for different regions of the heart but the length-to-width ratio of about 5 is fairly constant [4]. Each cardiomyocyte is enclosed by a phospholipid bilayer membrane which electrically separates the inside from the outside of the cell. The membrane can electrically be considered as a parallel plate capacitor with only about 75 Å distance between the plates and hence a high capacitance of approximately 1 μF/cm^2 [5]. The intracellular (cytoplasm) and extracellular fluids contain ions at different concentrations. For each ion type, the concentration gradient from higher to lower ion concentration causes a diffusion force. The difference between extracellular and intracellular ion charge causes a transmembrane voltage V_m across the charge separating membrane capacitor. The sum of these two forces is called electrochemical potential gradient [6, p.13]. The cell membrane contains proteins which form ionic channels and ionic pumps. Ionic channels can be considered as leaks through which ions can pass the membrane down their concentration gradient, whereas ionic pumps continuously transform metabolic energy to pass ions against their concentration gradient through the membrane and thus maintain the concentration differences that allow activation to occur. The types of ions that carry most of the current flow across cardiac cell membranes are sodium (Na^+), calcium (Ca^{2+}), potassium (K^+), and chloride (Cl^-) [6, p.10]. Ionic channels can switch their state between open and closed. The process of change of the channel state, called channel gating, can depend on the transmembrane voltage (voltage-gated), the binding of chemical messengers (ligand-gated) [7, p.160ff.], or mechanical properties (stretch activated) [8]. Most of the ionic channels are selectively permeable to one single type of ions. The probability of open channels for a certain ion type is represented by an electrical conductivity. Ionic currents are classified depending on ion type, channel-gating, and properties concerning the respective conductivity dependent on time (slow vs. fast channels) or voltage (e.g. rectification). The properties of ionic channels and pumps as well as of transmembrane ionic currents have extensively been studied. Mathematical models representing the membrane kinetics have been introduced and consequently refined to reflect physiological and pathophysiological behavior of cardiac myocytes (see Section 2.3).

The value and time course of the transmembrane voltage V_m reflect the activation state of a cardiomyocyte.

Resting Potential

In the absence of electrical activation the value of V_m is termed *resting potential* [4] (RP). The resting potential of a cardiac myocyte is approximately $\mathrm{RP} = -90\,\mathrm{mV}$ [5].

To trigger the activation of a cardiomyocyte, its transmembrane voltage needs to be elevated above the specific threshold level which is about $V_{m_{th}} = -60$ to $-75\,\mathrm{mV}$ in working myocytes and about $V_{m_{th}} = -40$ to $-60\,\mathrm{mV}$ in pacemaker cells of the sinoatrial and atrioventricular nodes [10]. In pacemaker cells this happens spontaneously, working myocytes are activated due to propagated activation from a neighboring cell or by artificial electrical stimulation. The complicated interaction between electrochemical potential gradient and channel gating generates a characteristic transient alteration in V_m, termed *action potential* (AP).

Cardiac Action Potential

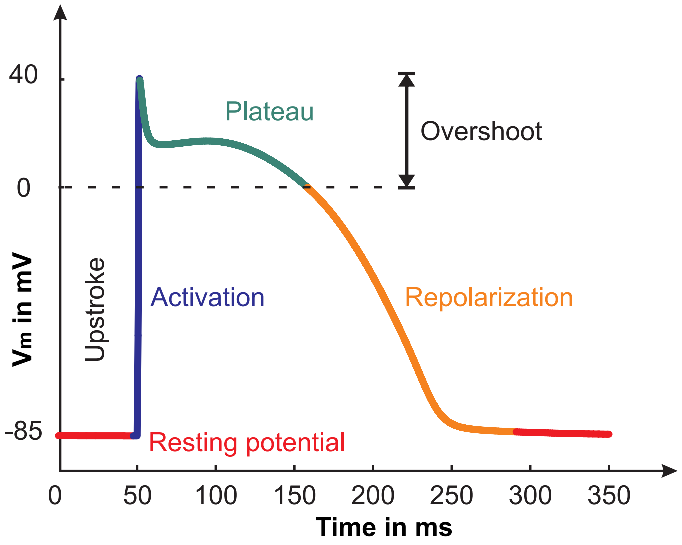

Figure 2.1: Action potential of a ventricular myocardial cell generated with the *Mahajan-Shiferaw* membrane kinetics model [11]. Provided by F. Campos (Medical University of Graz, Institute of Biophysics, 2011).

Figure 2.1 shows the action potential $V_m(t)$ of a ventricular myocardial cell as a func-

---

[4] In electrophysiological literature, the term ”potential” is often used without definition of the reference potential. In case of the ”resting potential” it means the transmembrane voltage, in case of the ”action potential” it means the transient alteration of transmembrane voltage over time. To stay consistent with literature, this physically incorrect nomenclature is adopted throughout this work.

[5] This value roughly corresponds to the Nernst potential of potassium, because at rest the membrane is mainly permeable to potassium. More accurately, the RP can be determined using the Goldman-Hodgkin-Katz equation which takes other ion types into consideration [9, p.106].

tion of time. Starting from the resting potential of about $V_m = -90\,\mathrm{mV}$, an upstroke reaching a peak of approximately $V_m = +40\,\mathrm{mV}$ characterizes the short depolarization phase with a duration of $\Delta t_0 < 1\,\mathrm{ms}$. In most[6] excitable heart muscle cells, the depolarization is generated by an inflow of sodium ions [6, p.43]. After the overshoot, the depolarization phase abruptly ends because of the closure of the sodium channels. V_m slowly approaches zero during the relatively long plateau phase, before it falls back on the resting potential during the repolarization phase. The time interval from the onset of the depolarization phase and the return of V_m to the resting potential[7] is termed *action potential duration* (APD).

The shape of the AP considerably differs for myocytes from different regions in the heart as well as for different species [12]. AP's of atrial myocytes in general show a shorter plateau phase and a reduced APD compared to those of ventricular myocytes.

During a certain phase within the activation process a myocardial cell is unreceptive to new stimulation. This *refractory time* prevents from reentrant activation waves within the heart[8]. In healthy myocardium there is a close temporal relationship between refractory time and APD. Hence, APD may be used as estimate of refractory time, and vice versa [13].

2.1.2 Propagation of Activation

Each heart muscle cell is connected to several neighboring cells (on average 6 in the terminal crest[9] in the right atrium, 11 in the left ventricle [4]). The voltage gradient from an activated to a quiescent neighboring cell causes a current via low electrical resistance channels, so-called *gap junctions*. The local current circuit is closed through the low resistance in the extracellular space, the so-called *volume conductor*. A constriction of the volume conductor results in impaired or terminated propagation of activation [15].

The passage of the electrical activation from cell-to-cell across the myocardium is often described as propagating depolarization wavefront[10].

---

[6] In some parts of the heart, e.g. the atrioventricular node, calcium currents are mainly responsible for the depolarization process [6, p.43].

[7] Due to the fact that the exact instant of the return of V_m to the resting potential is difficult to identify, the APD is commonly determined from the onset of the depolarization phase to the time when V_m reaches 90 % of its resting value.

[8] It should be noted that the refractory time is subdivided into an *absolute* and a *relative refractory time*. During the latter one, the cell may be activated but the threshold voltage is elevated.

[9] The terminal crest (Crista terminalis) is a significant fiber bundle in the right atrium [14].

[10] In contrast to the depolarization, the repolarization of cardiac tissue is not a propagation phenomenon but takes place spontaneously in each cell. Nevertheless, the term ”repolarization wave” is used.

Anisotropy of Cardiac Propagation

Propagation of activation in myocardium is generally anisotropic, i.e. the conduction velocity[11] along the fiber axis is higher than transverse to the axis. The anisotropy ratio, i.e. the ratio between longitudinal and transversal conduction velocity, is between 3:1 in the ventricles and 10:1 in the terminal crest [16]. This anisotropy has two major reasons [17].

1) Cell geometry: As mentioned in Section 2.1.1, cells have elongated shape and the resistance of the cytoplasm is lower than the resistance of the gap junctions [18].

2) Gap junction distribution: The gap junctions are not uniformly distributed around a cell. In left ventricular cells of adult dogs, about 50 %, in the terminal crest about 80 % of the gap junctions are on the frontal side of the cell [4].

Like ion channel conductivity (see Section 2.1.1), gap junction conductivity can be modulated [19]. The reduction of gap junction conductivity stronger affects transversal conduction velocity and increases the anisotropy ratio [20].

Due to the anisotropy in the electrical properties of the myocardium, a propagating activation wavefront which originates from a point-like stimulus has an elliptic shape.

2.1.3 Continuity of Propagation

From a macroscopic point of view, the propagation of electrical activation in homogeneous heart tissue is continuous, albeit anisotropic. In the following, the propagation is examined in different size scales, namely subcellular, microscopic, and macroscopic. Subcellular propagation refers to dimensions smaller than the size of a single cardiomyocyte (about $100\,\mu m$), dimensions below the spatial extent of the upstroke of the action potential ($0.25-1$ mm) are called microscopic, otherwise macroscopic [21].

Macroscopic Propagation

In the macroscopic view, the course of impulse propagation is determined by the gross anatomy of the myocardium. Infarcted tissue or large vessels are obstacles which force the propagating activation wave to change its pathway.

In order to mathematically describe impulse propagation in myocardium, the tissue was represented as electrical syncytium[12]. Its resistance and capacitance were expressed

---

[11] Conduction velocity is attributed to the active propagation process in contrast to passive so-called *electrotonic* electric conduction. To stay consistent with electrophysiological literature, this notation has been adopted.

[12] The heart muscle is seen as a functional syncytium, a network of cells. The contraction follows the ”all-or-nothing” principle, i.e. if one cell is activated all the others are activated.

per unit length as lumped parameters. The obtained *cable equations*[13] introduced a relation between tissue geometry, ionic currents, and transmembrane voltage in a continuous cable-like fiber structure. It was demonstrated that according to experimental results the conduction velocity is proportional to the square root of the fiber diameter and to the square root of the maximum uprise in transmembrane voltage [6, p.32],[22],[23].

The cable theory (partially) succeeded in explaining macroscopic electric properties of propagation in well-defined tissue structures like the cylindrical papillary muscle [16] and was extended to model two-dimensional tissues with anisotropic properties [24].

Extensive experimental studies, however, have revealed that the continuous description is an oversimplification of reality. Spach *et al.* observed, contrary to the cable theory, faster action potential upstroke velocity in slower transversal propagation in comparison to longitudinal propagation [25]. The explanation for this phenomenon was that the tissue consists of low resistance cytoplasm and high resistance cell-to-cell connections which could not be interpreted by the lumped parameters in the cable equations. Kléber *et al.* demonstrated the limits of the cable theory in case of increased cell-to-cell uncoupling [26]. Therefore, even in macroscopically continuous tissue the discontinuous nature of the myocardial microstructure has effects on the macroscopic impulse propagation, which cannot be explained by the continuous cable theory. Especially the research of cardiac arrhythmogenesis requires taking the microscopic propagation into account.

Microscopic Propagation

The propagation of activation in cardiac tissue is influenced by heterogeneities in microstructure and dispersion of gap junctions. Such microstructural heterogeneities may cause a change in activation source-sink relation, i.e. the number of downstream cells to depolarize is decreased or increased. The first case occurs at tissue boundaries where current flow is disabled, which influences the shape of the action potential [27]. The opposite case is given at a tissue expansion, as for instance at a fiber branching, where the enhanced number of downstream cells causes a reduction in conduction velocity or even a conduction block [28]. In this case, the impulse propagation terminates because the initiating cell may not furnish enough current to depolarize the downstream cells.

Microscopic propagation is furthermore impaired by fibrosis[14]. The connective tissue embedded between cardiomyocytes forms microstructural obstacles for the propagation of electrical activation. These obstacles usually have elongated shape and dimensions in cell size range.

---

[13] The underlying equations are commonly known as *telegraph equations.* In electrophysiological literature the telegraph equations describing the continuous impulse propagation along a cable-like muscle fiber are denoted as ”cable equations”.

[14] *Cardiac fibrosis* denotes the increased fraction of connective tissue between cardiomyocytes. Fibrosis is caused by aging or diseases by reorganization of cardiomyocytes [29].

Depending on their density and distribution, these obstacles may form constrictions or complex pathways for the impulse propagation. Whereas the former may cause unbalanced source-sink relation, the latter may result in wavefront collisions and tedious course of propagation. In a macroscopic view, substantial delays in activation and a reduction in conduction velocity can be observed.

Reduced conduction velocity and (unidirectional) conduction block are major factors for reentry[15] and, as a consequence, arrhythmias [16].
Cardiac diseases often lead to a modification of tissue function and structure, called remodeling, which in turn favors arrhythmogenesis.

Subcellular Propagation

At a subcellular size scale, the propagation of activation is inherently discontinuous, because the cardiac tissue is a network of discrete muscle cells with different electrical properties of cytoplasm and gap junctions. Apart from that, conduction properties are not continuous within a heart muscle cell but depend on the dispersion of gap junctions and the activation sequence. Computer simulation studies [30] as well as experimental studies using optical mapping in single cardiomyocytes [31, 32] and cell cultures [33, 34] have demonstrated the heterogeneity of impulse propagation in a subcellular range.

2.1.4 Extracellular Electrical Signals

As described in Section 2.1.2 the propagation of activation in myocardium involves local current flow through the volume conductor in the extracellular space. Hence, the tissue can be considered as current source. The extracellular electric potential at a point of observation is related to the subjacent source currents as follows: For a set of source points $\boldsymbol{x_s}$ within the surface area Γ_T of the tissue, the extracellular potential Φ_e at the point of observation $\boldsymbol{x_f}$ is given as

$$\Phi_e(\boldsymbol{x_f}, t) = \frac{1}{4\pi\sigma_e} \int\limits_{\Gamma_T} \frac{I_m(\boldsymbol{x}_s, t)}{\boldsymbol{r}_{sf}} d\Gamma_T, \tag{2.1}$$

where σ_e is the conductivity of the volume conductor[16], and $\boldsymbol{r}_{sf}$ is the geometric distance between source and field points. Equation 2.1 states that the waveform of the extracellular potential is affected by the waveforms of the current sources and their distance to the point of observation. In other words, the volume conductor acts as a spatial lowpass and temporal averaging filter for electric current. Extracellular electrical signals, denoted *electrograms*, therefore reflect the electrical activation of cells in the adjacencies of the measurement position.

---

[15] In normal cardiac activation, the refractoriness of the cardiac tissue prevents a given site from being repeatedly activated by single impulse. In pathological settings, the activation wave can reenter and reactivate this site in repetitive cycles. This mechanism is termed *reentry* [16].

[16] It is assumed that the volume conductor has infinite extent and its conductivity σ_e is continuous and anisotropic.

2.2 Measurement of Cardiac Activation

Depending on the purpose of the study, the species and type of preparation, the extent of the area under investigation, the spatial and temporal resolution, and the experimental or clinical environment, a variety of different measurement techniques are being used to measure cardiac electrical activation and its propagation across the heart tissue. After a description of the different measurement techniques, methods for cardiac activation mapping, i.e. specifying the spatial and temporal sequence of electrical activation, in in-vitro experiments with cardiac tissue preparations or isolated entire hearts are presented. A brief insight into clinical mapping systems is given at the end of the Section.

2.2.1 Measurement Techniques of Cardiac Activation

Transmembrane Measurement of Cardiac Activation

The action potential of a cardiomyocyte can be detected by directly measuring the potential difference across the cell membrane with an extracellular electrode and an intracellular electrode inserted into the tissue. As intracellular electrode for cardiomyocytes microelectrodes consisting of a glass micropipet filled with an electrolyte [35] are used. The reference electrode is placed on the outside of the investigated cell closely to the inserted microelectrode.

Transmembrane measurements allow the direct determination of the AP, but usually damage the tissue under investigation. The fine electrode tips are hardly durable and parallel measurements at multiple positions are a laborious task.

The advantage of this method is that the course of the AP as well as absolute values of V_m can be determined.

Optical Measurement of Cardiac Activation

The preparation is stained with a voltage-sensitive dye[17] which binds to the cell membrane and changes its optical properties (e.g. fluorescence) due to the changes of the membrane potential. These transient changes can be measured by means of optical color sensors [37]. Drawbacks of optical techniques are the low signal-to-noise ratio of the overall measurement system and the photo-toxicity of the applied dye substances which may affect the impulse propagation [38, 36]. Because optical mapping methods are contact free, the mechanical movement of the tissue due to the contraction leads to artifacts in the measured signals. In order to study repolarization, substances blocking the contraction are used, which in turn have effects on the activation pattern [39, 40]. Moreover, the optical recording does not represent the action potential of a single cell but rather the sum of

---

[17] In optical measurement of cardiac activation, the ANEP (AminoNaphtylEthenylPyridinium) substances *di-4-ANEPPS* and *di-8-ANEPPS*, respectively, are predominantly used [36].

action potentials in the adjacency of the measurement site. This phenomenon is caused by photon scattering effects [41]. To obtain the absolute value of the membrane resting potential, a reference measurement by a transmembrane microelectrode is required [42].

Extracellular Measurement of Cardiac Activation

Extracellular electrograms (see Section 2.1.4) may be determined by means of so-called *unipolar* or *bipolar* electrode setups in the volume conductor surrounding the cardiac tissue. Unipolar methods measure the potential difference of an electrode with respect to a distant reference electrode. In case of bipolar methods, the voltage between two closely spaced electrodes is considered [43].

Each type of measurement has advantages over the other: Unipolar methods are less sensitive to the direction of impulse propagation than bipolar methods. The bipolar setup fails to detect activation when a wavefront reaches both electrodes simultaneously. Bipolar measurements, in turn, are less sensitive to other local and distant activation events which superimpose within the volume conductor. A quadrupolar setup consisting of two orthogonal bipolar measurements is described in detail in Chapter 3.

It should be noted that no direct mechanical contact between the electrode and the tissue is required. In contrast to transmembrane voltages, extracellular signals are weaker in amplitude and more variable in wave shape.

Measurement of Monophasic Action Potentials

A monophasic action potential (MAP) is an extracellular potential waveform whose shape is similar to the shape of a transmembrane voltage. MAP's are measured between two extracellular electrodes one of which is placed at a permanently depolarized site on the tissue. In the past, such a permanently depolarized site was obtained by injury. In contemporary MAP measurement systems, a contact electrode is either pressed against the tissue surface [44], or a syringe needle filled with KCl is slightly inserted into the tissue [45]. The two electrodes usually have a diameter of $1-2\,\mathrm{mm}$ and are separated by about $5\,\mathrm{mm}$, which is on one hand distant enough to ensure that the non-contact electrode is outside the permanently depolarized area, and on the other hand close enough to minimize far field influence on the recorded signal [44].

MAP measurements are used in clinical application because they allow the estimation of the action potential duration without damaging the tissue. Simultaneous measurements at several positions are possible. Although the shape of the MAP is fairly similar to the shape of the AP, upstroke velocities during the depolarization phase and absolute potential values are not comparable. The locality of the measured waveform is limited to several millimeters. Moreover, MAP's often show an additional deflection in the upstroke. Unstable electrode contact due to the movement of the beating heart causes artifacts which may be misinterpreted [44].

Experimental and computer simulation studies have compared shapes of AP and MAP. In case of a good signal quality, the MAP can estimate action potential duration with high fidelity [44, 46]. Nevertheless, the mechanisms which lead to MAP's are still not completely clear [45, 47, 48].

2.2.2 Cardiac Activation Mapping

In order to specify the cardiac activation sequence, multisite recordings are required. This can be obtained by multiple simultaneous recordings or by time serial mapping. The latter supposes stability of the activation pattern during the recording procedure.

Optical Mapping Systems

Optical mapping methods are applied to cardiac preparations to investigate propagation phenomena from subcellular to organ level [49].
Optical mapping allows the specification of global activation and is thus well-suited for the investigation of arrhythmias. Moreover, the measurement systems are hardly affected by the presence of external electric fields, allowing cardiac activation mapping even during defibrillation[18].

Extracellular Mapping Systems

In order to study the pattern of activation at the surface of cardiac tissue preparations, sensors consisting of arrays of multiple wire electrodes (up to several hundreds) have been constructed [50]. For inter-electrode distances of less than 100 μm thin-film technique on rigid or flexible substrates was used [51, 52].
Despite the small inter-electrode distances, the multitude of electrodes and the space required for their wiring make the entire sensor bulky. It is not feasible to adjust the plane sensor plaque to the complex topology of the tissue in a way that all electrodes maintain equal distance to the surface of the tissue. Moreover, the sensor may impair the spread of activation across the tissue by obstructing the volume conductor at the surface of the tissue. Besides, the measurement, acquisition, and visualization systems for these types of sensors are complex [53].
A different approach is time serial mapping using microminiature, flexible sensors which allow accessing any point of interest even in tissue with complex anatomical structure [54].

---

[18] *Defibrillation* means the application of an electric current to the heart tissue in order to terminate arrhythmia.

Clinical Mapping Systems

Clinical mapping systems are predominantly used in the treatment of atrial arrhythmias by catheter ablation[19] [55]. State-of-the-art clinical mapping systems consist of a catheter system for intracardiac recording in combination with an anatomical navigation system [56]. Intracardiac electrograms are commonly recorded by means of circular mapping catheters with a variable diameter of $15 \ldots 20\,\mathrm{mm}$ comprising 10-20 electrodes [57].

2.3 Computer Simulation of Cardiac Activation

Computer simulation has become an indispensable tool to study electrophysiological phenomena in the healthy and diseased heart. In contrast to experimental studies, all relevant parameters can be controlled and observed with high accuracy, and the resulting signals are free of noise. Nevertheless, computer models of cardiac activation are simplifications of the real propagation phenomena. Moreover, they need to be validated through experiments.

Two components contribute to the simulation of cardiac electric activation. First, a model of cellular membrane dynamics which describes the flow of ions across the cell membrane, and second, a tissue model which combines cells and environment to a virtual tissue.

Computer models of single cardiomyocytes are commonly based on the mathematical description of the gating of ionic channels and the resulting ionic currents across an electric equivalent circuit of the cell membrane. Numerous models of membrane kinetics, differing in species, specimen, and detail level, have been developed [58, p.65]. Usually the membrane kinetics are formulated as a system of ordinary differential equations (ODE's).

Multiple cells are combined to represent the anatomical structure at the tissue level. The propagation of activation is modeled by incorporating intercellular electrical coupling. These cell-to-cell interactions are described by a set of partial differential equations (PDE's).

Coupling the ODE's and the PDE's leads to the bidomain model [9, p.298ff.].

The bidomain equations are numerically solved after spatial discretization (finite elements methods) and temporal discretization (Crank-Nicholson method) [59, 60]. Solving the bidomain equations is computationally demanding, however, under certain assumptions the bidomain model may be reduced to the monodomain model [61].

An important issue of computer simulations of the heart is the required computational power which depends on the number of elements, the number of time steps, i.e. the product of the temporal resolution and the duration of the simulation, the used cell membrane model, and the model type (monodomain or bidomain).

---

[19] Catheter ablation is an invasive technique in the treatment of various tachyarrhythmias. Electrical pathways which may lead to arrhythmias are ablated, either by alternating current at radiofrequencies (radiofrequency ablation) or by freezing (cryoablation).

Chapter 3

Cardiac Electric Near Field Signals

In this Chapter, the origin and properties of cardiac electric near field (CNF) signals are described and methods to calculate characteristical parameters from CNF signals are introduced.

3.1 Definition of the Cardiac Electric Near Field

The potential gradients in the volume conductor at the cardiac surface due to the activation sequence describe a time-dependent electric field. The components of the electric field strength vectors which arise in a two-dimensional plane, parallel and very close to the tissue surface build up the CNF [62]. At a point of observation $\boldsymbol{x}_F$, the CNF field strength $\boldsymbol{E}$ is

$$\boldsymbol{E}(\boldsymbol{x}_F, t) = -\nabla\Phi(\boldsymbol{x}_F, t), \tag{3.1}$$

where $\Phi(\boldsymbol{x}_F, t)$ is the extracellular potential at $\boldsymbol{x}_F$. The temporal development of the electric field strength $\boldsymbol{E}(\boldsymbol{x}_F, t)$ provides information about local properties of the propagation of activation in the subjacent tissue.

Univariate or multivariate extracellular potential waveforms acquired within the CNF are henceforth termed *CNF signals*.

3.2 Computation of the CNF Strength

A spatially discrete approximation $\tilde{\boldsymbol{E}}$ of the CNF strength $\boldsymbol{E}$ can be established from two extracellular potential differences[1]. The components E_x and E_y, i.e. the potential gradient

---

[1] In the following, $\boldsymbol{E}$ is used to denote the spatially discrete approximation of the CNF strength.

in two dimensions in parallel to the surface of the tissue can be estimated by potential differences between two recording sites divided by the distance [63]. Figure 3.1 shows the principle of a sensor with four electrodes arranged in a square. The acquired extracellular potentials $\Phi_1 \ldots \Phi_4$ allow the computation of $\boldsymbol{E}$ in the center of the four electrodes.

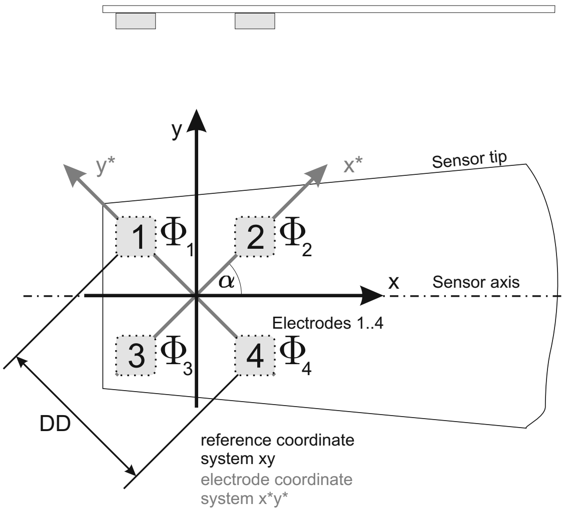

Figure 3.1: Principle of a CNF sensor. Four electrodes $1 \ldots 4$ at the tip of the sensor are arranged in a square with diagonal distance DD. The four extracellular recordings $\Phi_1 \ldots \Phi_4$ allow the reconstruction of the CNF strength. The electrode coordinate system $x^* \, y^*$ is rotated by the deflection angle α with respect to the reference coordinate system $x \, y$. In this arrangement, the reference coordinate system is arranged with the sensor axis and $\alpha = 45°$.

For the estimation of the components of the CNF strength $\boldsymbol{E}^* = \left[E_x^* \; E_y^*\right]$, the potentials at two diagonal electrode pairs separated by the distance DD are used. E_x^* and E_y^* calculate as follows:

$$E_x^*(t) = \frac{-(\Phi_2(t) - \Phi_3(t))}{\mathrm{DD}} \tag{3.2}$$

$$E_y^*(t) = \frac{-(\Phi_1(t) - \Phi_4(t))}{\mathrm{DD}} \tag{3.3}$$

The electrode coordinate system $x^* \, y^*$ is rotated by the deflection angle α in mathematically positive sense with respect to the reference coordinate system $x \, y$. To obtain the components E_x and E_y in the reference coordinate system, α has to be added to the angles of E_x and E_y.

For a certain instant of time τ, E_x and E_y are:

$$E_x(\tau) = \sqrt{E_x^*(\tau)^2 + E_y^*(\tau)^2}\ \cos\left(\arctan\frac{E_y^*(\tau)}{E_x^*(\tau)} + \alpha\right) \tag{3.4}$$

$$E_x(\tau) = \sqrt{E_x^*(\tau)^2 + E_y^*(\tau)^2}\ \sin\left(\arctan\frac{E_y^*(\tau)}{E_x^*(\tau)} + \alpha\right) \tag{3.5}$$

In order to resolve $\boldsymbol{E}$ with the necessary accuracy for the evaluation of impulse propagation in microstructural range, an ultra-dense arrangement of electrodes is required. The maximum electrode distance DD depends on the spatial extent of the depolarization wavefront. In a computer simulation study the effects of spatial undersampling in the approximation of the $\boldsymbol{E}$ were investigated and the theoretical basis for the development of CNF sensors was accomplished [62]. The authors found that the accurate measurement of $\boldsymbol{E}$ would require DD $< 100\,\mu$m.

3.3 Properties of Local Propagation Computed from CNF Signals

In this Section, parameters for the characterization of the local propagation of activation, computed from univariate CNF signals Φ as well as from multivariate CNF signals $\boldsymbol{\Phi}$ are described.

3.3.1 Activation Time

The activation time denotes the instant of time at which a heart muscle cell is activated. By means of isochrones of local activation time (LAT), the activation pattern of a tissue region can be reconstructed. The time of the maximum upstroke of the transmembrane voltage V_m is seen as reference value for the local activation time (LAT) [64].

The standard method of LAT determination from extracellular potentials Φ is to identify the time of the maximum negative peak of its temporal derivative $\dot{\Phi}$, which highly correlates with the time of maximum upstroke in V_m, as was shown in computer simulation [65] and experimental studies [64]. Another computer simulation study demonstrated that the times of maximum upstroke in V_m and maximum downstroke in Φ coincide for starting, ending, free running, and colliding wavefronts of activation [27]. Experiments with human atrial myocardium confirmed these findings [66]. In poorly coupled cardiomyocytes as well as in case of heterogeneities in membrane properties or cell coupling, significant discrepancies may occur [65].

The minimum derivative method frequently fails when Φ is fractionated, i.e. $\dot{\Phi}$ shows multiple negative deflections [67]. Furthermore, this method is prone to noise which is enhanced by the temporal differentiation operation. Hence, many authors have presented alternative methods for LAT determination.

Geselowitz *et al.* have shown that the zero crossing of surface Laplacian, an approximation of the transmembrane current I_m, is an accurate marker for LAT [68] while suppressing distant activity. The determination of LAT using the spatial gradient of Φ, i.e. the CNF strength $\boldsymbol{E}$, has been investigated by Plank *et al.* [69] in a computer simulation study. They found that their method was more robust against noise and shows lower errors in the vicinity of structural discontinuities, compared to the minimum derivative method.

Ellis *et al.* introduced a deconvolution method based on the expression of the volume conductor equation as a linear filtering operation (see Section 2.1.4) [70], i.e. a convolution of membrane current obtained from a computer simulation and a transfer function incorporating geometric parameters and conduction velocity. They concluded that their method was more accurate than the minimum derivative method and was suitable for LAT determination from fractionated electrograms.

Punske *et al.* [67] have shown in an experimental study that for nonfractionated as well as for fractionated electrograms spatial methods performed better, i.e. determined activation times were closer to those obtained by visual assessment of isopotential maps. LAT isochrones were obtained from isopotential maps by hand, which made the method at least partly subjective.

Chouvarda and Maglaveras introduced a spatial deconvolution method as well as a wavelet-based method to estimate membrane currents and activation times in a discontinuous 2D-computer model [71].

3.3.2 Conduction Velocity

The conduction velocity (CV), i.e. the speed which the electrical activation propagates with, differs considerably in different regions of the heart. The fastest CV's are found in the Purkinje fiber network ($\theta = 2\,m/s$), the slowest in the ventricles ($\theta = 0.5\,m/s$) [16].

Slow conduction is an important factor of arrhythmogenesis, because the CV is a determinant factor of the size of reentrant circuits [16]. Reduced CV may have different anatomical, physiological, and pathophysiological reasons. Alterations in membrane properties, especially the reduced sodium conductance may decrease the CV down to a lowest limit of about $\theta = 0.17\,\mathrm{m/s}$, below which the propagation of activation is blocked [72]. Very slow conduction, however, is caused either by reduced cell-to-cell coupling [72] or by complex microstructure of the cardiac tissue [73].

The determination of conduction velocity between two or more recording sites requires estimating two parameters, 1.) the distance and 2.) the time delay in activation between the recording sites. When activation mapping is conducted by electrode arrays, the distance between the recording sites is given. The distance between two spatially independent electrodes requires the localization of the recording positions. Especially in tissue with complex macrostructure or microstructure, however, the activation may not propagate along the shortest pathway between the recording sites. For multiple measurement sites with known distance between each other on known pathways, as e.g. in cable-like tissue structures, the CV can be obtained by linear regression of path length and LAT. The slope of the linear regression line corresponds to CV. The goodness of fit can be evaluated by the Pearson product-moment correlation coefficient r between the regression line and the measured values.

Figure 3.2 gives an example of the determination of CV along a pectinate muscle in rabbit atrium by means of linear regression of path length and LAT from 11 recording positions. The global CV in the muscle is compared to local conduction velocities θ at the recording positions.

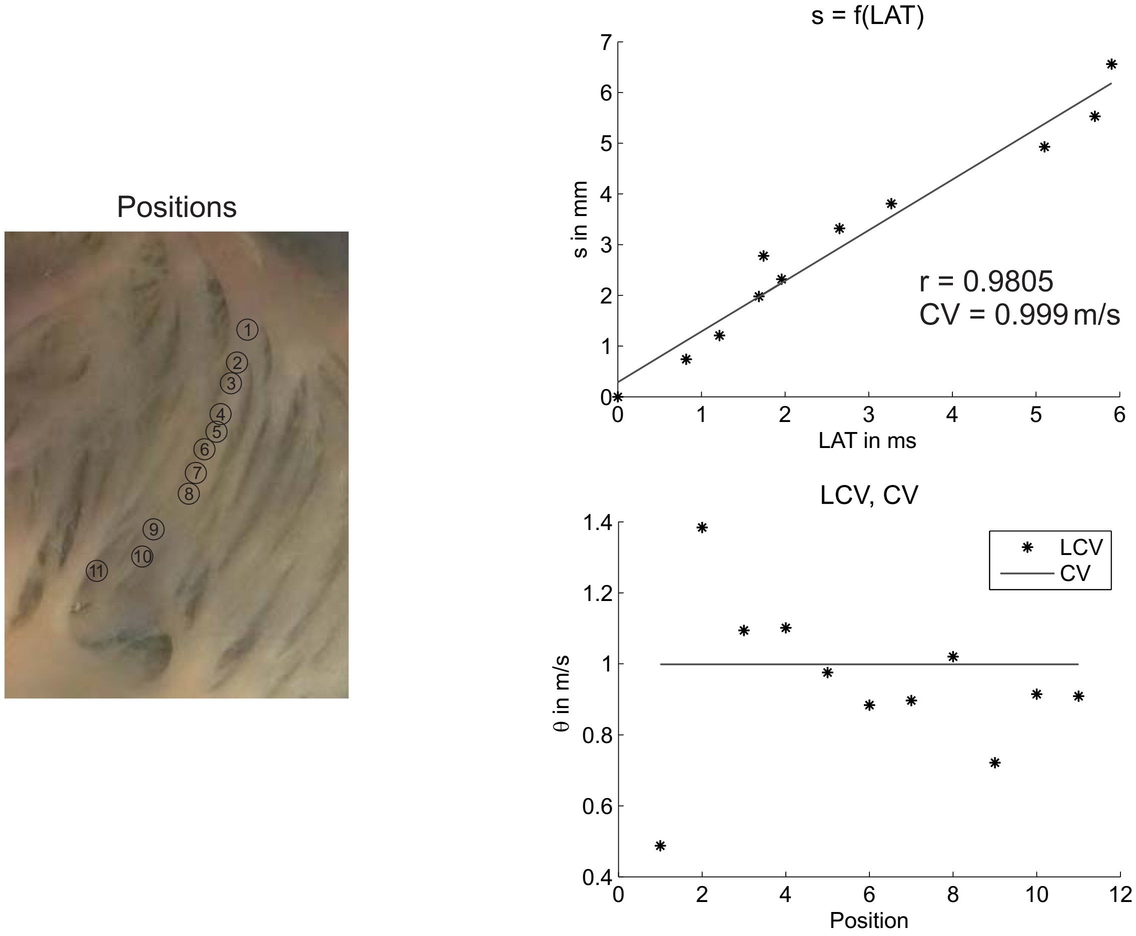

Figure 3.2: Conduction velocity along a pectinate muscle in rabbit atrium. The image shows the measurement positions 1-11 along the muscle. *Upper diagram:* Path length s as a function of local activation times LAT along the muscle. The slope of the regression line represents a conduction velocity CV = 0.999 m/s, the correlation coefficient r=0.9805. *Lower diagram:* Local conduction velocities θ at positions 1-11 compared with CV.

From four CNF signals $\Phi_1 \ldots \Phi_4$ measured in a square arrangement the gradient of LAT and thus the vector of local conduction velocity (LCV) $\boldsymbol{\theta}$ pointing in the main direction of propagation of activation can be estimated. The principle of this arrangement with distance DD between diagonal observation points is shown in Figure 3.1. To determine magnitude θ and direction φ of $\boldsymbol{\theta}$, the following methods are used.

Minimum Derivative Method (dmin)

The four LAT's $\mathrm{LAT}_1 \ldots \mathrm{LAT}_4$ from $\Phi_1 \ldots \Phi_4$ are determined by the time of the maximum negative peak of their temporal derivatives $\dot{\Phi}_1 \ldots \dot{\Phi}_4$. The gradient of LAT is computed at the center of the four observation points using a finite difference approach:

$$\nabla LAT(x,y) = \begin{bmatrix} \mathrm{LAT}_x \\ \mathrm{LAT}_y \end{bmatrix} \approx \frac{1}{\mathrm{DD}} \begin{bmatrix} \mathrm{LAT}_4 - \mathrm{LAT}_1 \\ \mathrm{LAT}_3 - \mathrm{LAT}_2 \end{bmatrix} \tag{3.6}$$

The vector of LCV $\boldsymbol{\theta}$ is expressed as follows:

$$\boldsymbol{\theta} = \begin{bmatrix} \theta_x \\ \theta_y \end{bmatrix} = \frac{1}{\mathrm{LAT}_x^2 + \mathrm{LAT}_y^2} \begin{bmatrix} \mathrm{LAT}_x \\ \mathrm{LAT}_y \end{bmatrix} . \tag{3.7}$$

Magnitude θ and angle φ are obtained:

$$\theta = \sqrt{\theta_x^2 + \theta_y^2}, \quad \varphi = \arctan \frac{\theta_y}{\theta_x} + \alpha \, , \tag{3.8}$$

where α is the deflection angle (see Section 3.2).

Cross Correlation-Based Method (CCF)

A common method to obtain the time delay between two waveforms is the use of their cross correlation function (CCF). The time of the maximum of the CCF gives the time delay between the two waveforms. This method has also been applied to extracellular electrograms in order to determine time delays and hence, according to Equations 3.6 and 3.7, conduction velocities. Often, the maximum of the CCF is not well-defined but rather broad, which may lead to ambiguous results. In such cases, the use of the Hilbert transform may simplify the time delay estimation. The imaginary part of the Hilbert transform of the CCF shows a negative-to-positive zero crossing at the time of the maximum of the CCF [74]. Shors *et al.* [75] have improved the resolution of the estimated time delay by linear interpolation of the section around the zero crossing.

The CCF method has has been established for the computation of $\boldsymbol{\theta}$ from CNF signals [76]. The accuracy of the resulting values is enhanced by sinc-interpolation of the CCF (cf. Section 7.2.1). Fast correlation and sinc-interpolation by zero padding of the CCF in the frequency domain were combined.

Maximum Field Strength Method (Emag)

Apart from φ, the angle of $\boldsymbol{\theta}$, the main direction of propagation can be estimated from the angle of CNF strength $\boldsymbol{E}$. At the time of the maximum of $|\boldsymbol{E}|$, $\boldsymbol{E}$ is oriented perpendicularly to the isochrones of LAT and points in the opposite direction of the local propagation of activation [62]. The magnitude of LCV, however, cannot be determined from a single waveform of $\boldsymbol{E}$.

3.3.3 Vector Loop of $\boldsymbol{E}$ during Depolarization

At a particular point within the CNF, the plot of the two orthogonal components of the CNF strength, $E_x(t)$ and $E_y(t)$ against each other is considered. During depolarization of the underlying tissue, this plot exhibits a loop-type shape, and is therefore called vector loop of $\boldsymbol{E}$.

Such vector loops of $\boldsymbol{E}$ have been acquired in experimental studies [63], [77], [78], and variations in their morphology have been reported.

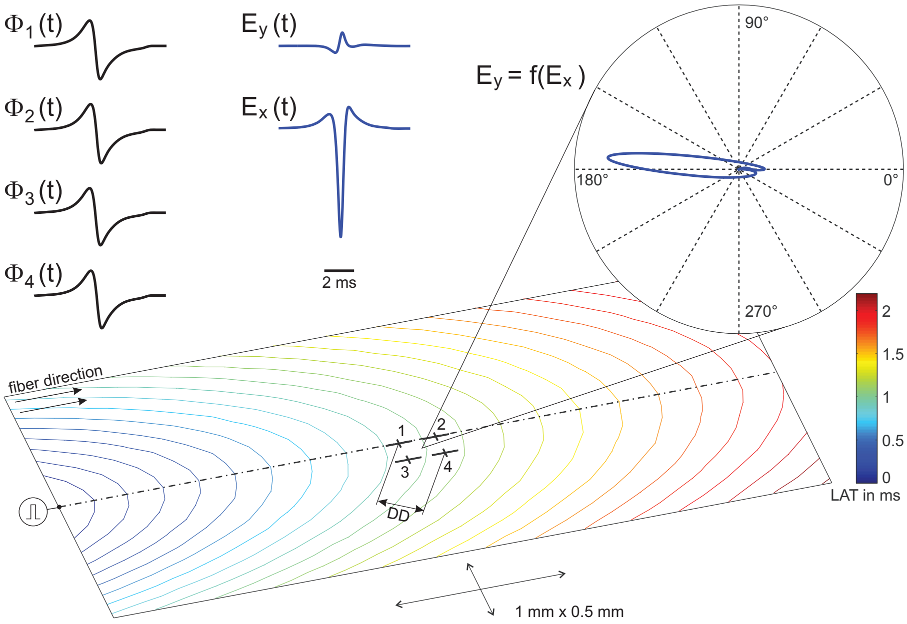

Figure 3.3: The vector loop of CNF strength $\boldsymbol{E}$ in case of continuous elliptic propagation of electrical activation. The activation was induced by a point-like stimulus in the center of the left tissue edge. Extracellular potentials $\Phi_1(t) \ldots \Phi_4(t)$ were observed close to the center of the tissue in a square arrangement with diagonal distance DD. Orthogonal electric field components E_x and E_y as functions of time were computed from $\Phi_1(t) \ldots \Phi_4(t)$. The vector loop of $\boldsymbol{E}$ is the plot of $E_y = f(E_x)$. Its tip points opposite to the main direction of propagation. The isochrone interval is 100 μs.

Figure 3.3 illustrates the vector loop of $\boldsymbol{E}$ resulting from the continuous anisotropic spread of an activation wave. The diagrams show the extracellular potentials $\Phi_1(t) \ldots \Phi_4(t)$ at four points of observation $1 \ldots 4$ as well as the orthogonal components $E_x(t)$ and $E_y(t)$ of the CNF strength $\boldsymbol{E}$ and the associated vector loop of $\boldsymbol{E}$ computed in the center of four points of observation. The tip of the vector loop indicates $\hat{\boldsymbol{E}}$, the vector with the peak magnitude of $\boldsymbol{E}(t)$. It points opposite to the main direction of the activation wave. The time at which $\hat{\boldsymbol{E}}$ occurs, is an accurate marker of LAT [62].

Due to its geometric structure and its sensitiveness to beat-to-beat changes of propagation parameters, the vector loop of $\boldsymbol{E}$ is an excellent tool for on-line evaluation of cardiac impulse propagation.

Several computer simulation studies have been carried out to investigate the origin of the vector loop morphology. The vector loop morphology in continuous tissue depends on the curvature of the depolarization wavefront. In case of planar wavefront, the vector loop of $\boldsymbol{E}$ becomes a straight line. During elliptic propagation, the vector loop of $\boldsymbol{E}$ is open at sites lateral to the axis of the elliptic wavefront. In a curved tissue structure representing a branching, the vector loop morphologies differ from those observed during uniform propagation [79]. Microscopic obstacles for the impulse propagation, such as inlays of connective tissue, lead to a deformation of the vector loop of $\boldsymbol{E}$ [80]. The collision of an activation wavefront with such an obstacle and resulting fractionated extracellular electrograms may give rise to complex vector loop morphologies [81].

In experiments a great variety of shapes of vector loops of $\boldsymbol{E}$ has been noticed [82]. However, the influence of imperfect experimental conditions on the morphology of vector loops of $\boldsymbol{E}$ is widely unclear.

3.3.4 Wavefront Curvature

The degree of wavefront curvature is defined as

$$\rho = -\frac{1}{r}, \tag{3.9}$$

where r is the radius of the curvature of the wavefront [16].

To obtain r or ρ, respectively, the activation pattern, i.e. the isochrones of LAT are required. Compared to the conduction velocity of a planar wavefront, the CV at the tip of a convex wavefront is lower whereas the CV of a concave wavefront is higher. The reason for this is a mismatch in the source-sink relation (cf. Section 2.1.3) [16].

As described in the previous Section 3.3.3, the curvature of the activation wavefront influences the morphology of the vector loop of $\boldsymbol{E}$. Open vector loops of $\boldsymbol{E}$ are attributed to strong wavefront curvature. However, the morphology of the vector loop of $\boldsymbol{E}$ is affected by other conditions like structural discontinuities in the tissue and measurement artifacts (cf. Sections 3.3.3 and 8.4).

3.3.5 Action Potential Duration

The depolarization and the repolarization of a cardiomyocyte are reflected in the extracellular potential waveform in an analogous manner. However, compared to the depolarization phase, the repolarization phase has a long duration and thus a large spatial extent. As a consequence, the respective event in Φ - if detectable at all - is characterized by very low amplitude and SNR. Due to the long duration of the depolarization, the respective event within Φ is more prone to power line interference.

The shape of the AP and its duration (APD) vary across the myocardium and differ among species. Spatial dispersion of APD across the myocardium may lead to different directions of the gradients of depolarization time and repolarization time. Thus, positive or negative deflection within $\dot{\Phi}$ is possible. Only a limited number of studies have evaluated extracellular estimators of APD. Millar *et al.* [83] have found a very high correlation between the activation-recovery interval[2] and the refractory time in unipolar electrograms from ventricular epicardium in dogs under a variety of physiological conditions. In a computer simulation study, the reliability of the activation-recovery interval in estimating the APD was demonstrated [65]. Recently, a series of repolarization time markers were compared in a 3D-computer simulation study [84]. Vigmond *et al.* have investigated the estimation of APD from atrial electrograms in a combined experimental and computer simulation study [85]. They have shown that lower signal amplitudes and different shape of the AP lead to a much worse estimation of APD in the atrium than in the ventricle.

Figure 3.4 shows AP and extracellular electrogram recorded in the right atrium of a guinea pig. The smooth descent of the AP in the repolarization phase leads to a moderate elevation in Φ.

3.3.6 Morphological Measures

From univariate CNF signals $\Phi(t)$ the following morphological properties can easily be determined.

- Amplitude of Φ: $\Phi_{pp} = \max\Phi - \min\Phi$
- Symmetry of Φ [86]: $a = \frac{\max\Phi - |\min\Phi|}{\max\Phi - \min\Phi}$
- Amplitude of $\dot{\Phi}$, the derivative of Φ: $\dot{\Phi}_{pp} = |\max\dot{\Phi} - \min\dot{\Phi}|$
- Depolarization time t_{dep}: $t_{dep} = t|_{\min\Phi} - t|_{\max\Phi}$

---

[2] The *activation-recovery interval* denotes the time between the maximum negative peak in the temporal derivative of the electrogram (LAT) and the maximum positive peak during the repolarization phase.

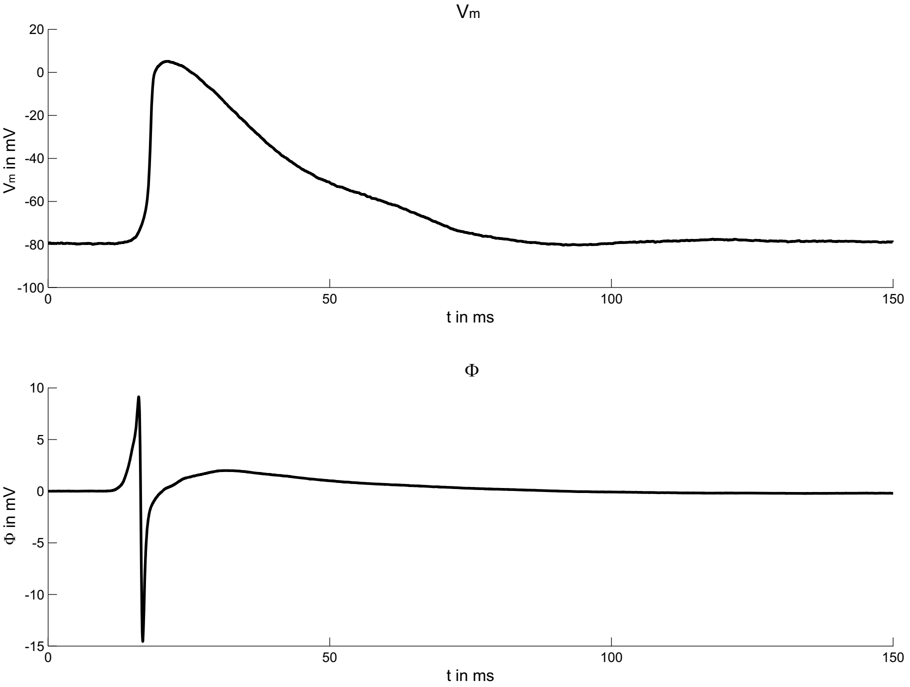

Figure 3.4: Action potential and extracellular electrogram recorded in guinea pig right atrium. *Upper diagram:* Action potential V_m. *Lower diagram:* Extracellular potential Φ. Recording positions and thus activation times are not identical. Unpublished experimental recordings provided by R. Arnold and E. Hofer (Medical University of Graz, Institute of Biophysics, 2011).

3.4 Morphology of Extracellular Electrograms

3.4.1 Nonfractionated Extracellular Waveforms

Even during uniform propagation, the waveform shapes of electrograms may vary. In the case of a free running activation along a cable-like muscle strand, the corresponding electrogram Φ shows a biphasic shape with similar magnitude of positive and negative phase. Close to an initiation site of impulse propagation, the positive amplitude of Φ is reduced, whereas close to a sealed end or a wavefront collision site, the negative amplitude is diminished [27].

Figure 3.5 gives an example of characteristic shapes of nonfractionated electrograms Φ. A cable-like myocardial fiber of 20 mm length was represented in a 1D-computer simulation. Activation was induced by stimulation at one end of the cable (Position **A**). At the surface of the cable, Φ was recovered at the beginning, in the middle, and at the end of the cable. The respective waveforms of Φ represent starting, free running, and terminating propagation of activation. In $\dot{\Phi}$, the differences in wave shape are not as clear as in Φ. However, it can be observed that the third phase of the triphasic waveform $\dot{\Phi}$ vanishes at

the cable end. Likewise, the first phase of $\dot{\Phi}$ vanishes at the beginning of the cable, which is not visible in this example because the waveform is corrupted by the stimulus artifact. An explanation for the shape of Φ and its variations may be given by simplifying the depolarizing activation wavefront as propagating dipole with non-zero spatial extent. When the dipole moves towards the recording site, Φ rises. After it has reached the recording site, Φ falls and becomes zero, when the dipole is centered at the recording site. As it moves away, Φ increases again. The lack of an approaching or leaving phase of the dipole, respectively, leads to the characteristic waveforms of Φ in case of a starting or terminating activation wavefront [87].
In case of a collision of activation wavefronts, Φ exhibits a similar shape as in case of a terminating wavefront at a sealed end.

3.4.2 Fractionated Extracellular Waveforms

Extracellular electrograms frequently do not show a single biphasic or monophasic deflection but a more complex morphology. Such electrograms Φ with two or more distinct deflections are referred to as fractionated[3]. Each deflection in Φ is manifested as negative peak in $\dot{\Phi}$. There is, however, no common agreement about the minimum magnitude of a peak to be taken into account. Values between 10 % and 20 % of the amplitude of the maximum negative peak value in $\dot{\Phi}$ are used. Fractionated electrograms are usually characterized by lower amplitude and longer duration [92].

Figure 3.6 shows a normal or nonfractionated as well as a fractionated waveform of Φ, their temporal derivatives $\dot{\Phi}$, and vector loops of $\boldsymbol{E}$. Both waveforms Φ were recorded during the same experiment at the surface of the right atrium of a rabbit.

Genesis of Fractionated Electrograms

The genesis of fractionated electrograms in the context of clinical recordings has been comprehensively reviewed by de Bakker and Wittkampf [87]. The authors discussed the following circumstances which may lead to fractionated electrograms: Artifacts due to the movement of the electrodes and power line interference, artifacts due to filtering, delay in activation of regions that are located close to each other, anisotropy of tissue properties, overlaying tissue structures, alterations in conduction velocity, and asynchronous conduction.

As described in Section 3.2, computation of the CNF strength requires small inter-electrode distances and small distances between electrodes and surface of the tissue. Therefore, electrograms recorded with CNF technique may be considered to represent

---

[3] Electrograms with two distinct deflections were also denoted *double potentials* [88], electrograms with more than one deflection *fragmented* [89], *multicomponent* [90], or *multiphasic* [91]. Throughout this work, the term *fractionated* is used.

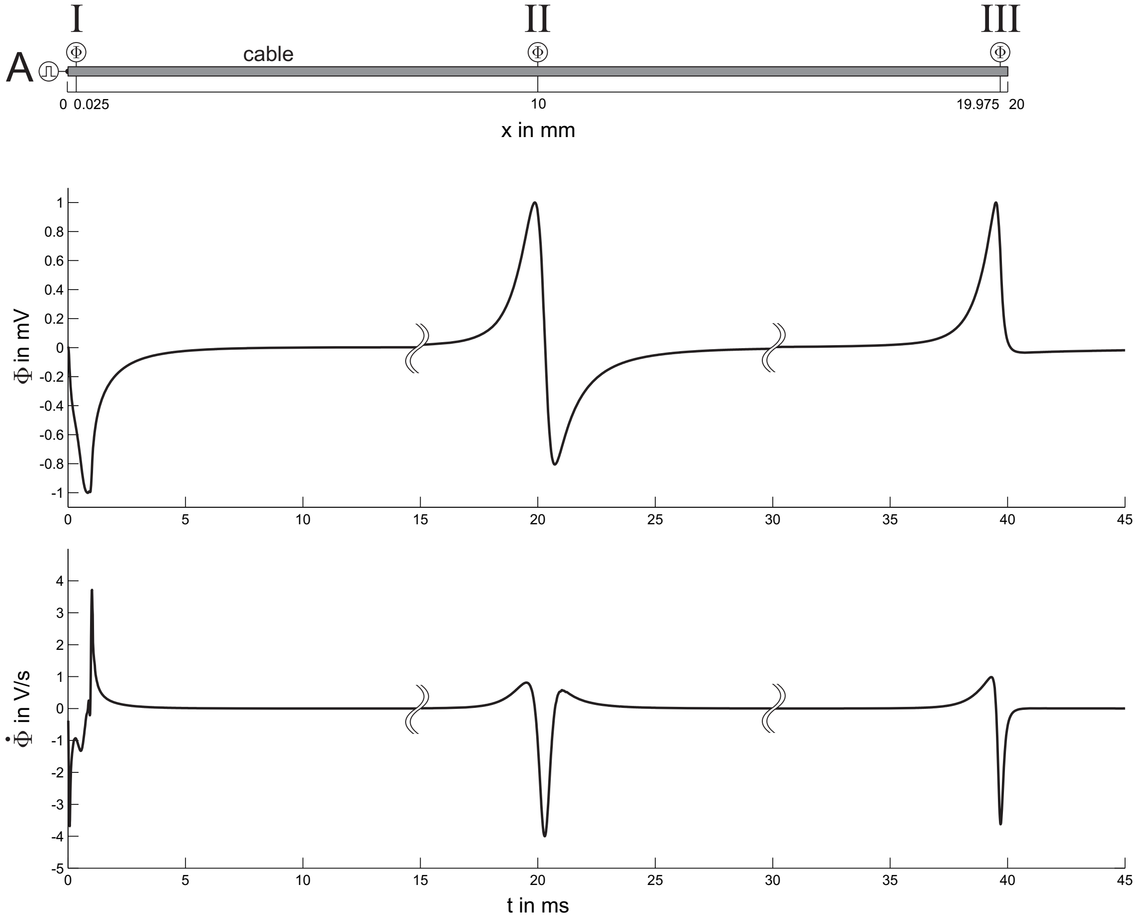

Figure 3.5: Characteristic waveform shapes of nonfractionated extracellular electrograms along a cable-like myocardial fiber. Activation is induced by stimulation at site **A**. Extracellular potentials Φ are recorded at the surface of the cable at positions **I** ($x = 0.025\,\mathrm{mm}$), **II** ($x = 10\,\mathrm{mm}$), and **III** ($x = 19.975\,\mathrm{mm}$). *Upper diagram:* Overlay plot of $\Phi(t)$ at positions **I**, **II**, and **III**. *Lower diagram:* Overlay plot of respective temporal derivatives $\dot{\Phi}(t)$. The stimulus artifact is clearly visible in $\dot{\Phi}(t)$ at measurement position **I**.

local propagation patterns. The major reason for the occurrence of fractionated local electrograms is the delayed activation of neighboring but electrically uncoupled regions. Those delayed activations interfere with the local signal via electrotonic interaction in the volume conductor surrounding the tissue. The reasons for delayed activation of adjacent tissue are on one hand structural complexities like muscle fiber junctions or electrically uncoupled parallel or crossing muscle fibers [21], and on the other hand embedded obstacles for propagation of activation. Such obstacles may be small scars or vessels, or inlays of connective tissue [29].

In a computer model study, it was demonstrated that the spatial variation of morphol-

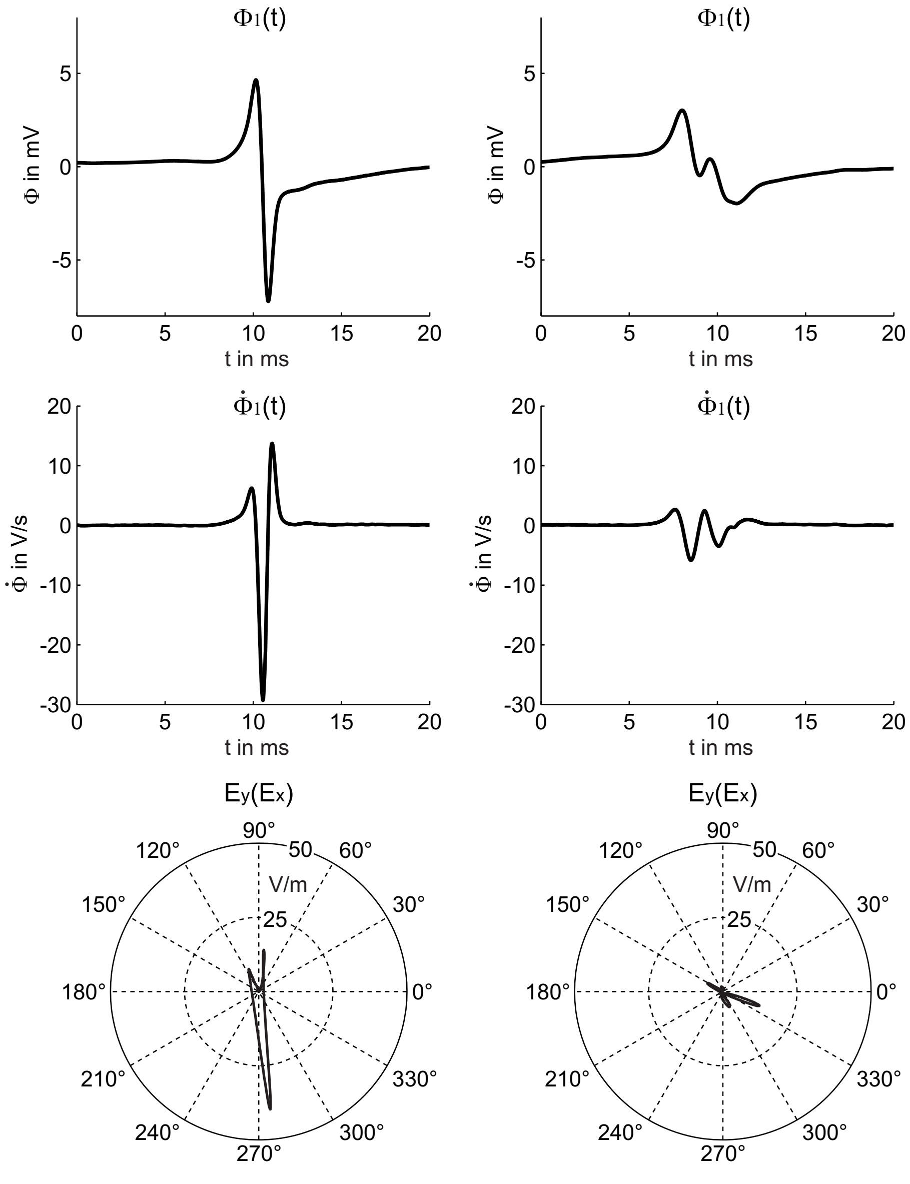

Figure 3.6: Nonfractionated vs. fractionated electrogram. *Left:* Nonfractionated electrogram Φ atop its temporal derivative $\dot{\Phi}$ and vector loop of CNF strength $E_y(E_x)$. *Right:* Fractionated Φ and derived signals.

ogy of electrograms increases with increasing heterogeneity of intercellular coupling [93]. Recently, the influence of microfibrosis on electrogram fractionation and macroscopic conduction parameters has been investigated in another computer simulation study [86].

Gardner *et al.* observed that the direction of propagation of activation has an influence on the fractionation of electrograms [94]. It was demonstrated in a computer simulation study that for fractionated electrograms to occur not only the presence of conduction obstacles, but also their orientation with respect to the direction of propagation matters [81]. Figure 3.7 demonstrates that on the same substrate fractionated electrograms may be observed or not, depending on the direction of propagation with respect to the orientation of the obstacle. A rectangular tissue sheet with an embedded elongated nonconducting obstacle was represented by a computer model. The stimulus site was chosen to induce either longitudinal elliptic propagation (LEP) or oblique elliptic propagation (OEP). The isochrones of LAT reflect the pattern of activation. In case of LEP, the obstacle has an influence on the activation pattern, but no significant delays in activation of adjacent regions occur. The temporal derivative $\dot{\Phi}(t)$ of the electrogram recorded at position × has a single negative peak. In case of OEP, the activation wavefront propagates continuously until encountering the lower left corner of the obstacle. Due to the changed electrotonic load, the activation propagates faster in front, and slower lateral to and behind the obstacle. $\dot{\Phi}(t)$ exhibits two negative peaks representing activation of the tissue below (first peak) and above (second peak) the obstacle.

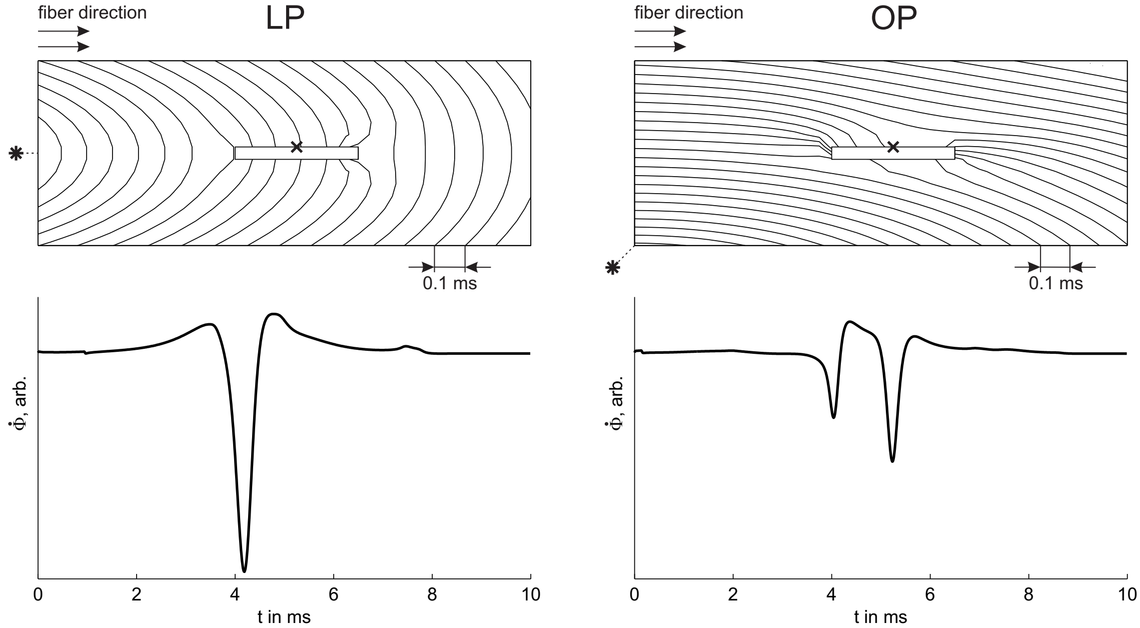

Figure 3.7: Directional dependence of electrogram fractionation. Computer simulation of a sheet of ventricular tissue (2000 μm × 750 μm) with embedded nonconducting obstacle (500 μm × 50 μm) in the center of the tissue sheet. *Left:* Schematic drawing of tissue sheet with longitudinal elliptic propagation (LP). Isochrones of LAT were created from V_m. Below, $\dot{\Phi}(t)$ computed 50 μm above the surface of the tissue is plotted. *Right:* Oblique elliptic propagation (OP) results in fractionated $\dot{\Phi}(t)$. The recording and stimulus positions are indicated with × and $*$, respectively.

Analysis of Fractionated Electrograms

The identification and characterization of complex fractionated atrial electrograms (CFAE's) has become an important task in clinical cardiology. Areas where fractionated electrograms are recorded during catheter mapping are seen as critical substrates for arrhythmogenesis. Those sites are being used as targets for catheter ablation [95].
Apart from classification upon visual inspection, automated algorithms for real time application have been developed. Scherr *et al.* have used morphological features of 2.5 s recordings of bipolar electrograms during atrial fibrillation (AF) to classify CFAE's [96]. Křemen *et al.* have used wavelet analysis to classify degrees of fractionated electrograms recorded during AF [97]. CFAE's have been associated with tachyarrhythmias, however, they are also observed during sinus rhythm, in an increased proportion with increasing age [98].

Different time and size scales as well as the fact that the mentioned automated algorithms are dedicated to CFAE's recorded during AF, they are not directly applicable to CNF signals. Two major problems arise when calculating parameters from fractionated local electrograms. First, the signal amplitude is usually lower and thus the signal-to-noise ratio (SNR) is reduced, and second, the determination of LAT may become ambiguous (cf. Section 3.3.1).

Chapter 4

Experimental Setups and Methods

In this Chapter, the setups which are used to carry out electrophysiological experiments using CNF technique, computer simulations of electrical activation, and analyses of the obtained CNF signals are introduced.

4.1 Electrophysiological Experiments

The setup for conducting electrophysiological experiments at the Institute of Biophysics at Medical University of Graz has been developed over many years. In this Section, a brief description is given, details have been specified elsewhere [99, 54]. The setup mainly consists of dedicated components which have been developed and manufactured in-house. In this Chapter, such components are marked with an asterisk (*).

4.1.1 Experimental Setup

Figure 4.1 shows a schematic of the experimental setup. The measurements take place on an absorbing table within a metal cage* which serves as Faraday cage to shield external electric fields. The preparation is fixed within a tissue bath* including a bath heating* and a transillumination device* with LED technology [100]. Oxygenated Tyrode's solution[1] is kept circulating through the bath via a tubing system by a roller pump. The temperature of the solution is regulated using PID control. Around the tissue bath five 3D-micromanipulators* holding pen-shape fixtures for the CNF sensors are attached. These fixtures contain the impedance converters*. Shielded cables connect to the preamplifiers* and the main amplifier*. Further recording or stimulus electrodes are applied to the preparation by means of 3D-micromanipulators.

---

[1] Tyrode's solution consist of (in mM/l): NaCl 132.1, KCl 5.4, $CaCl_2$ 2.5, $MgCl_2$ 1.15, $NaHCO_3$ 24, $NaHPO_4$ 0.42, D-glucose 5.6. The solution is gassed with a mixture of 95 %O_2 and 5 %CO_2.

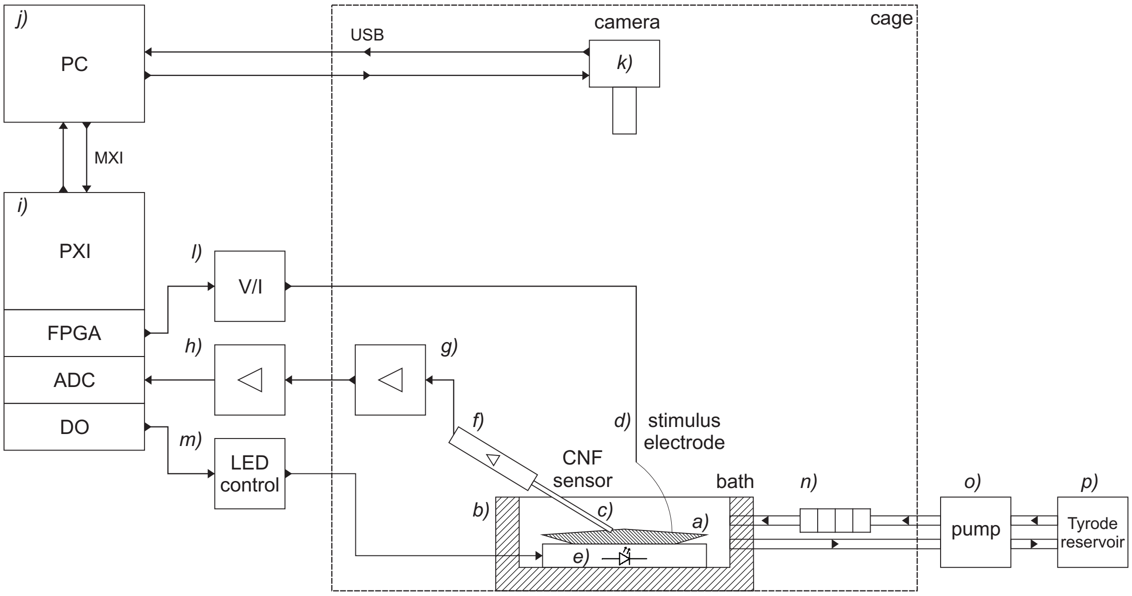

Figure 4.1: Experimental Setup. *a)* Specimen, *b)* tissue bath, *c)* CNF sensor, *d)* stimulus electrode, *e)* specimen carrier containing LED's, *f)* impedance converter, *g)* preamplifier, *h)* main amplifier, *i)* PXI rack containing FPGA, ADC, and DO (digital output) boards, *j)* PC, *k)* digital camera, *l)* current source, *m)* LED control, *n)* bath heating, *o)* roller pump, and *p)* Tyrode reservoir and preheating.

The measurement hardware comprises electrodes, amplifiers, and data acquisition (DAQ) boards for acquisition, conditioning, and digitalization of CNF signals as well as digital cameras for the acquisition of images. Furthermore, a computer system for the processing and visualization of the digitized signals and images is part of the measurement hardware.

Sensors

Extracellular potentials at the cardiac surface are detected by unipolar voltage measurements with respect to an electrode at reference potential. The CNF sensor consisting of a four channel electrode array allows the simultaneous measurement of four extracellular voltage signals. The Ag/AgCl-electrodes have a pad diameter of $18\,\mu$m and are arranged in a square with inter-electrode spacing of $50\,\mu$m. Images and a schematic drawing of the CNF sensor are shown in Figure 4.2. This ultra-dense quadratic arrangement of the electrodes allows the accurate approximation of orthogonal potential gradients and thus the CNF strength (see Section 3.2).
The tips of the silver electrodes are electro-chemically chlorinated to decrease their coupling impedance and to stabilize the electrode potential [101, pp.5]. Fabrication and

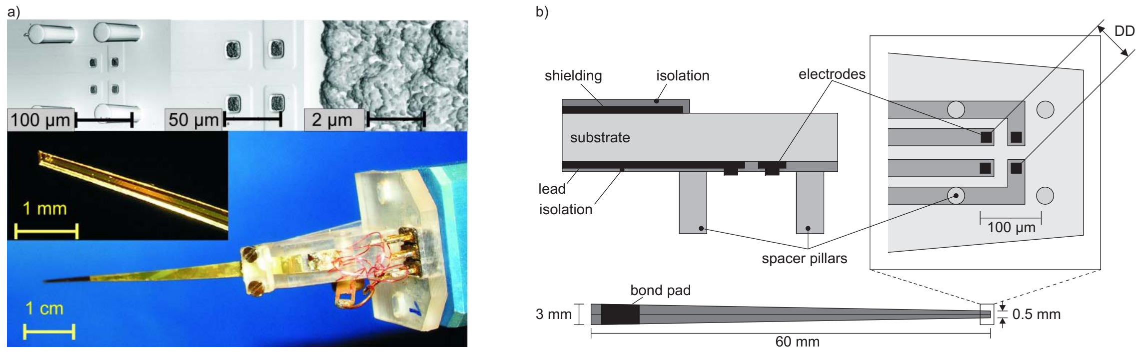

Figure 4.2: CNF sensor. *a)* Images in different magnifications. *b)* Schematic drawing. With permission from [54].

detailed specifications of the CNF sensor are given in the article of Hofer *et al.* [54]. This tongue-like type of sensor allows to access any point of interest even in complex anatomical structures. Due to the mechanical properties of its polyimide carrier, the sensor floats with the contraction of the tissue under examination. The tip of the sensor is equipped with spacer pillars from epoxy-based photoresist. They avoid the lateral displacement of the sensor due to the contraction and maintain a constant distance $z = 50\,\mu$m between electrodes and surface of the tissue.

In order to correctly assign the reconstructed CNF strength vector to the measurement position, the rotation angle β of the sensor with respect to the orientation of the specimen has to be taken into account. Images of the recording site taken with the digital camera (see Section 4.1.3) allow the estimation of β with sufficient accuracy. For the computation of CNF parameters, β has to be regarded in the same manner as the deflection angle α, which is explained in Section 3.2.

Reference electrode In experiments with tissue preparations, a ring-shaped reference electrode surrounding the investigated preparation is placed inside the tissue bath. In Langendorff experiments (see Section 4.1.2), the reference electrode is placed close to the cannula which is used to perfuse the heart.

The Amplifier Circuit

The 20-channel signal amplifier with an overall gain A = 100 consists of separate impedance converters (unity gain), preamplifiers (A = 10), main amplification stages (A = 10), and anti-aliasing filters for 20 input channels plus five reference channels. It adapts the small potential differences between each of the four electrodes and the reference electrode to the input range of the DAQ board. Due to the fact that the electrodes are highly sensitive to bias currents, very high demands on the shielding of the signal cables and on the input stage of the preamplifier[2] are made.

---

[2] Ultra-low bias current operational amplifiers with a maximum bias current of less than 100 fA are used (*Texas Instruments OPA129*, USA).

The amplified signals are then filtered with a 4^{th} order Bessel-type lowpass filter with a cutoff frequency $f_C = 20\,\mathrm{kHz}$. This filter also works as an anti-aliasing filter for the discretization of the amplified signals. Additionally, a highpass filter with a cutoff frequency $f_C = 0.6\,\mathrm{Hz}$ can be switched on to compensate the polarizing DC components of the sensor signals.

Data Acquisition Board

The electrically conditioned sensor signals are digitized with dedicated DAQ boards (*National Instruments NI PXI–6123* and *NI PXI–6120*, USA). The DAQ boards contain separate analog-to-digital converters (ADC) for each of their input channels. Thus, simultaneous sampling of up to 20 analog signals at a sampling rate $f_S = 100\,\mathrm{kHz}$ is performed.

Quantization noise of the ADC The ADC with a resolution $N = 16\,\mathrm{bit}$ has a full scale range (FSR) of ±10 V. Taking into account the overall amplifier gain A = 100 of the three amplifier stages, the FSR corresponds to a signal range $\Phi_{pp} = 200\,m\mathrm{V}$. The voltage resolution q is:

$$q = \frac{\Phi_{pp}}{2^N} = 3.052\,\mu\mathrm{V}$$

Computer System

The controlled acquisition of the CNF signals, on-line signal processing, visualization, and signal recording, is performed by a custom-designed measurement system termed *HARMS* (high-performance arrhythmia research measurement system)* [99]. The hardware of HARMS consists of a PXI[3] rack (*National Instruments NI PXI-1024Q*, USA) containing data acquisition and generation boards, and a desktop PC with quad core processor (*Dell Optiplex*, USA). PC and PXI are connected via MXI interface with a data throughput of 110 MB/s. An arbitrary impulse generator used for electrical pacing of the preparation has been implemented on an FPGA[4] (*National Instruments NI PXI-7813R*, USA) [102].

The software of HARMS was programmed in *LabVIEW* (National Instruments, USA). It controls data acquisition, stimulus generation, and audio acquisition as well as camera control and image acquisition via USB[5] and firewire (IEEE 1394). The acquired CNF signals are processed and displayed in real time. On-line processing comprises filtering and computation of $\boldsymbol{E}$ and LCV. Signal data can be stored to hard disk either as a continuous stream or per beat during a window of defined length. The modular software design allows the integration of new developed signal processing algorithms.

---

[3] PXI (PCI (Peripheral Component Interconnect) eXtensions for Instrumentation) is a modular instrumentation platform which is based on the PCI. It adds integrated timing and synchronization functionality and a rugged industrial form-factor.

[4] FPGA: Field-Programmable Gate Array

[5] USB: Universal Serial Bus

4.1.2 Specimen

The experimental setup is geared to preparations from small mammalian hearts. Preparations of mouse, rat, guinea pig, and rabbit have been used for experimental studies. Animal preparation has conformed the national ethic guidelines.

The three most common specimen in experiments which are described in this work are the *right atrial isthmus*, the *papillary muscle*, and the *Langendorff preparation.* Figure 4.3 shows images taken during experiments with these specimen.

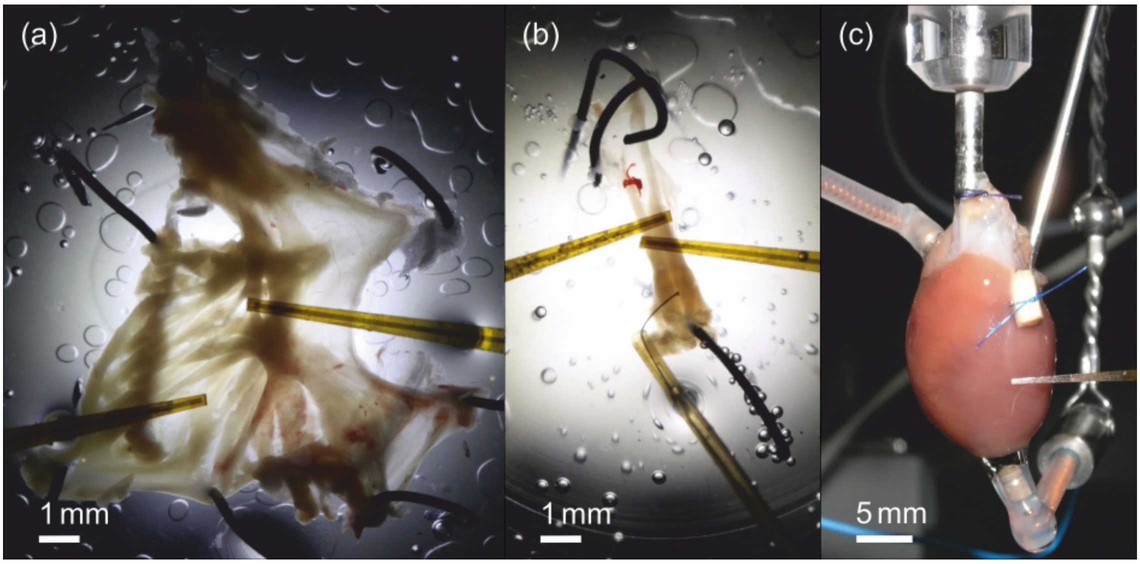

Figure 4.3: Specimen in electrophysiological experiments with CNF measurement. *(a)* Autorhythmic right atrial isthmus of a guinea pig. Two CNF sensors are placed at the surface of the preparation, in the network of pectinate muscles (left sensor) and at the terminal crest (right sensor). *(b)* Electrically paced guinea pig papillary muscle. The muscle is stimulated at its base. CNF signals are recorded with two sensors. *(c)* Langendorff preparation of a rat heart. The coronary occlusion caused by a piece of a toothpick impairs the supply with Tyrode's solution in the adjacent ventricular tissue. A CNF sensor is placed inside the ischemic zone.

Right Atrial Isthmus

The right atrial isthmus comprises the terminal crest, the network of pectinate muscles, and the tricuspid valve vestibule [103]. This region is seen as a critical substrate for the genesis of intermittent block of conduction and atrial flutter[6] [104] and is targeted during catheter ablation of atrial flutter [105]. The dissected specimen is fixed inside a temperature controlled tissue bath and superfused with oxygenated Tyrode's solution (see Figure 4.3 (a)). This preparation contains the sinoatrial node and therefore usually is autorhythmic.

---

[6] *Atrial flutter* is characterized by rapid, irregular atrial contractions. As a result, the pumping of blood into the ventricle is impaired.

Papillary Muscle

The papillary muscles[7] of the right ventricle have a relatively large cable-like geometry and are therefore preferred substrates for studying the propagation of activation. Papillary muscles have been considered as anatomical substrates which show fairly continuous impulse propagation. An experimental study, however, has revealed partially complex micropropagation [82].
The preparation is fixed in the tissue bath as shown in Figure 4.3 (b). Because the isolated papillary muscle usually is not autorhythmic, electrical pacing is required. A programmable current-impulse generator [106] and a pacing electrode from tungsten wire are used for stimulation. Pacing in constant intervals as well as sophisticated pacing protocols are being used [102].

Langendorff Preparation

An isolated beating heart is attached to the Langendorff apparatus (*IH-5, HUGO SACHS ELEKTRONIK*, Germany) and perfused with Tyrode's solution which is introduced into the aorta by a cannula [107] (see Figure 4.3 (c)). This type of experiment allows the investigation of cardiac impulse propagation at autorhythmic activation. A series of other physiological parameters such as left ventricular pressure, electrocardiogram, and coronary flow can be measured. In Langendorff preparations, arrhythmia studies and ischemia-reperfusion studies[8] are common experimental protocols.

4.1.3 Documentation of Macrostructure

During the experiment, the positions of sensors and stimulus electrodes at the surface of the tissue are documented by means of digital images. Image acquisition and storage is controlled via HARMS. After the experiment, high resolution transillumination images can be taken with a custom-designed scanning device*. Three digital cameras are in use.

1) Microscope camera (*Sony DFW–X700*, Japan): This C-mounted color digital video camera outputs images with a resolution of 1024 × 768 pixels. The camera is controlled via firewire.

2) Compact camera (*Olympus C–5060WZ*, Japan): The compact camera is used during Langendorff experiments. Images are acquired in super macro mode at a resolution of 5.1 MPixel (2592 × 1944) in a minimum distance of 3 cm. This corresponds to a maximum resolution of 10 μm/Pixel. The camera is controlled via USB 1.0.

---

[7] *Papillary muscles* exist in the right and in the left heart. They prevent the atrioventricular valves from prolapsing into the atrium.

[8] Myocardial *ischemia* is caused by insufficient blood flow to the muscle tissue, predominantly due to a narrowing of the coronary arteries or thrombosis. The restoration of the blood flow is termed *reperfusion*.

3) Single-lens reflex camera (*Canon EOS 5D Mark II*, Japan): The camera has a 36 × 24 mm CMOS[9] chip which allows a resolution of 21.1 MPixel (5616 × 3744 Pixel). During the experiment the camera is attached to the top of the experimental cage at a distance of approximately 60 cm from the specimen and takes images from a fixed perspective using a macro objective (*Canon 3,5/180mm L USM*, Japan). The images show sections of 60 × 40 mm at a resolution of 10.68 μm/Pixel. After the experiment the camera is used with a macro lens (*Canon MP–E65 Zoom*, Japan) to take transillumination images with a resolution of 1.28 μm/Pixel. The camera is controlled via USB 2.0 [108].

Image acquisition with either of the described cameras during the experiments has turned out to have no detectable influence on the measured signals.

4.1.4 Documentation of Microstructure

After the experiment, the tissue is fixed with a mixture of paraformaldehyde-glutaraldehyde, embedded in paraffin, and sliced with a microtome. The sections are stained using Masson's Trichrome, which results in a coloring of myocytes in red, connective tissue in blue, and intercellular clefts in white. Micrographs are digitized using a slide scanner (*Aperio ScanScope*, USA) with a resolution of 0.25 μm/pixel. The digital images are stored in single-file pyramidal tiled TIFF[10] (SVS format).

4.2 Computer Models and Simulation

In order to study propagation by means of the CNF, a series of computer models of different dimensions and complexity have been established. Activation was induced by simulating electric current stimuli of 1 ms duration. Extracellular electrograms were computed as described by Plank and Hofer [62] with a temporal resolution of 10 μs, which corresponds to the sampling interval used during the acquisition of CNF signals in experiments.

All simulations were performed using the *Cardiac Arrhythmia Research Package* (CARP) [109]. The utilized computer system is equipped with eight Quad-Core AMD Opteron 8386 SE 2.8 GHz processors with 126 GB of RAM running a 64-bit Linux system.

4.2.1 Continuous Tissue Models

Cardiac myocytes were arranged in a regular grid to build up a mesh of finite elements in a simple geometric form. Depending on the aim of the study, 1D, 2D, or 3D-tissue models have been created.

---

[9] CMOS: Complementary Metal-Oxyd-Semiconductor

[10] TIFF: Tagged Image File Format

A single strand of cardiomyocytes was represented by a 1D-monodomain model. Hence, the propagation of activation along a thin cable-like muscle fiber could be studied.

A thin sheet of cardiac tissue was represented by a 2D-monodomain model. Different longitudinal and transversal conductivities allowed incorporating anisotropy in propagation. Moreover, structural discontinuities like embedded nonconducting obstacles for propagation were realized.

A cylindrical muscle fiber was represented by a 3D-monodomain model. This model was used to evaluate the contribution of deeper current sources on the electrograms and the 2D-representation in the CNF strength.

4.2.2 Histologically Detailed Tissue Model

A digitized image taken from a single histological slice of a rabbit's right atrial isthmus, created as described in Section 4.1.4, was segmented using color clustering and thresholding technique to distinguish myocardium (red staining) from connective tissue (blue staining) and intercellular clefts (white background) [110]. The microscopic fiber orientations were obtained using an image intensity gradient method [111]. The generation of the finite element mesh from the segmented histograph was described in detail elsewhere [112]. At a spatial resolution of $8\,\mu$m, in total 2 695 299 nodes and 1 792 896 elements set up the microscopic model.

The histologically detailed 2D-model reveals the complexity of activation patterns caused by the microstructure, but does not reflect the shunting effects of subsequent layers of tissue in 3D. In order to alleviate such a drawback, a second layer of cardiac tissue was added. The structure of this shunt layer based on the same histograph, but neglected some microscopic details. Its conductivity was adjusted by comparing extracellular electrograms computed at the surface of the virtual tissue with those recorded in the particular heart region during electrophysiological experiments, in terms of the distribution of the fractionation index (cf. Section 7.5).

4.3 Signal Processing

The development of signal processing algorithms applied to CNF signals acquired with HARMS as well as obtained from computer simulations was done with MATLAB R2009a [113] including signal processing, optimization, statistical, and BioSig [114] toolboxes.

Developed algorithms for beat and artifact detection [102], calculation of LCV (described in Section 3.3.2), and quantification of fractionation (Section 7.5.2) have been implemented in LabVIEW and integrated in HARMS for on-line processing of CNF signals.

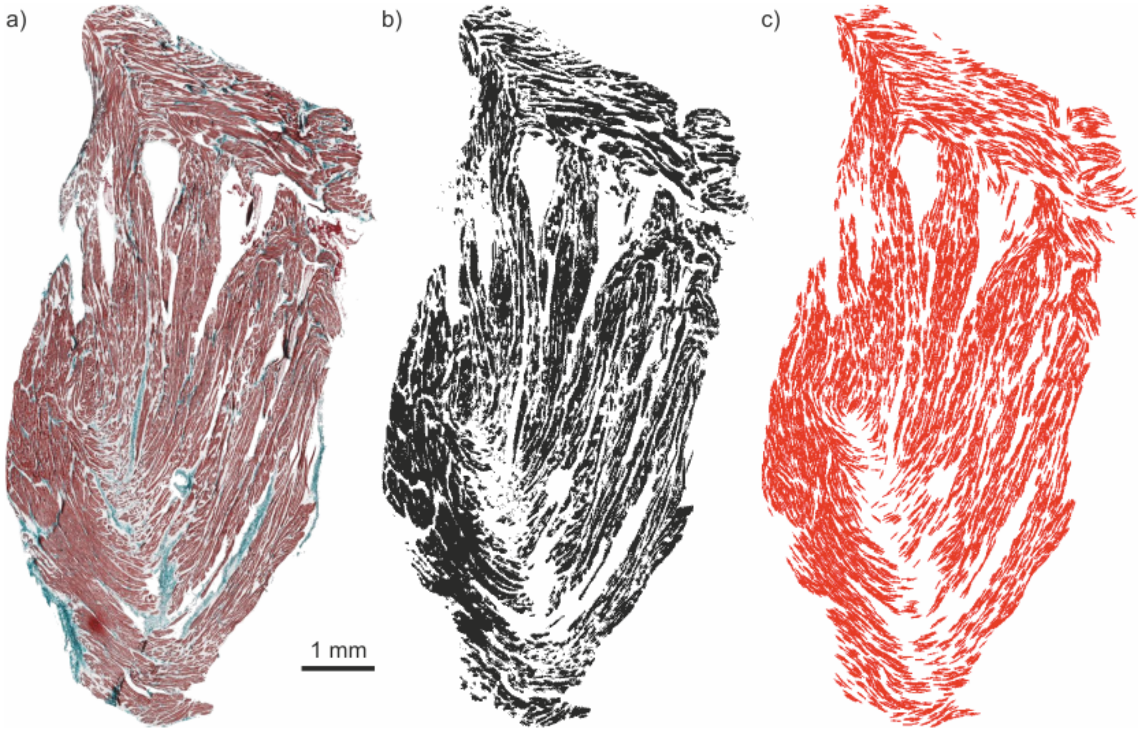

Figure 4.4: Generation of a histologically detailed tissue model of a rabbit's right atrial isthmus. *a)* Histograph of tissue slice. Myocytes are stained in red, connective tissue in cyan. *b)* Segmented image distinguishing myocytes (black) from connective tissue and intercellular clefts. *c)* Determined fiber directions indicated as direction vectors. Tissue histology was provided by D. Sánchez-Quintana (Department of Human Anatomy, Faculty of Medicine, University of Extremadura, Badajoz, Spain, 2011) images were provided by H. Ahammer and F. Campos (Medical University of Graz, Institute of Biophysics, 2011).

Chapter 5

Aims and Strategy

The theoretical basis of the CNF measurement technique has been established, and computer simulation studies have demonstrated its benefits and to a certain degree its limitations [62, 79, 80, 69]. A novel sensor to acquire CNF signals has been developed [54], and a comprehensive measurement systems has been presented which allows the on-line processing and visualization of magnitude and direction of the local conduction velocity (LCV) and the vector loop of CNF strength $\boldsymbol{E}$ [99].

Based on the experience gained during numerous electrophysiological in-vitro experiments with different preparations and animal species, two major problems became evident. First, no information could be given, how reliable the determined values of LCV and vector loop of $\boldsymbol{E}$ were, and second, no appropriate methods to identify and analyze the important class of fractionated local electrograms were available.

Hence, the specific aims of this work are

1) to investigate the influence of experimental conditions on the LCV and the vector loop of $\boldsymbol{E}$,
2) to introduce signal processing methods for the identification and analysis of fractionated local electrograms, and
3) to extract parameters from CNF signals which allow characterizing the microstructure of the underlying heart tissue.

The presented methods are aimed at electrograms obtained from experiments. For the development of these methods, however, waveforms resulting from established computer models of cardiac tissue have been used. These waveforms are noise-free and, in contrast to recorded signals, all relevant factors of their genesis are known and can be adjusted with high accuracy. To estimate the robustness of developed methods, noise of the same characteristics as observed under experimental conditions was added.

Part II

Analysis of Cardiac Near Field Signals

Chapter 6

Introduction

The studies presented in this Part comprise the analysis of CNF signals from electrophysiological in-vitro experiments and computer simulations, the design and conductance of computer simulations and experiments, the development and evaluation of signal processing algorithms, and the application of developed methods to CNF signals from experiments and computer simulations.

6.1 Signal and Noise Analysis of CNF Signals

In order to develop dedicated processing algorithms for CNF signals, detailed knowledge about time and frequency domain properties of signal and noise within the experimental environment is required.

Characteristical parameters of CNF signals have been described in Section 3.3. Their probability distribution and the correlation between the parameters was examined in a set of electrograms recorded during several experiments. The set was then separated into fractionated and nonfractionated electrograms, and the distributions of the parameters between the two classes were analyzed and compared. The obtained results were consequently used as constraints for CNF signal processing algorithms.

CNF signals recorded during electrophysiological experiments are perturbed by noise and power line interference. The major noise sources in the measurement chain are the electrode-electrolyte interface, the signal cables, the amplifier stages (impedance converter, preamplifier, main amplifier), and the ADC. To create artificial noise of the same characteristics as observed under experimental conditions, noise in the measurement chain needs to be analyzed. Detailed frequency analysis of the CNF sensor and the amplifier have been described previously [54, 115]. In this study, it was examined if the overall noise in the measurement chain may be represented by additive Gaussian band limited white noise and if noise should be created independently for the individual channels.

Design and parametrization of acquisition systems and processing routines are essentially based on the frequency response of the targeted signals. Therefore, a frequency analysis of CNF signals from computer simulations and experiments was performed.

6.2 Determination of Local Conduction Velocity

In Section 3.3.2, methods to compute the vector of local conduction velocity (LCV) from multivariate CNF signals $\mathbf{\Phi}$ were described. The vector of LCV $\boldsymbol{\theta}$, pointing in the direction of propagation, consists of the magnitude θ and the angle φ. In addition to the values θ and φ, their uncertainty was analyzed.
The uncertainty of $\boldsymbol{\theta}$ has two reasons. First, the limited temporal resolution of the time discrete electrograms $\mathbf{\Phi}$ and second, the overall noise in the measurement chain.
The temporal resolution of Φ is determined by the sampling rate f_S of the ADC. Increasing the temporal resolution by a factor M by raising f_S to M f_S results in an M-fold amount of data to be acquired, processed, and stored. Another approach to increase the temporal resolution is digital resampling, i.e. interpolation of the acquired waveforms. Thus, only the interesting segments of the waveform can be extracted and interpolated for subsequent on-line analysis and display.
In order to examine the influence of noise in the measurement chain of $\mathbf{\Phi}$ on the uncertainty of LCV, a computer simulation study has been carried out. The aims of this study were 1.) to determine the minimum amplitude-to-noise ratio (ANR) in the extracellular potential waveforms Φ at which the uncertainty of the determined values θ and φ remains within a given tolerance band, 2.) to determine the optimum cutoff frequency of a lowpass filter applied to $\mathbf{\Phi}$, and 3.) to compare different algorithms for the computation of LCV in terms of robustness against noise.
LAT's determined from fractionated electrograms $\mathbf{\Phi}$ may be ambiguous and thus, the computation of LCV may lead to erroneous results. Therefore, this study concentrates on nonfractionated electrograms which were obtained from computer simulations of continuous tissue models.

LAT's determined from transmembrane voltages V_m are being considered as gold standard (cf. Section 3.3.1). First, because such LAT's represent the activation of single cells, and second, because the steep slope of V_m during the depolarization phase allows reliably determining the LAT by the instant of the maximum $\dot{V}_m$, the temporal derivative of V_m. Therefore, also the LCV determined from a multivariate $\boldsymbol{V}_m$ can be considered as reference value. To study the deviation of LCV computed from extracellular signals with respect to the reference value, multivariate transmembrane voltages and extracellular potentials have to be recorded at the same position. In experiments, this is not feasible because glass pipet microelectrodes and extracellular electrodes cannot be placed at the same position and the impalement by the microelectrode would falsify the extracellular signals. Computer simulation, however, can provide both signals, $\boldsymbol{V_m}$ and $\boldsymbol{\Phi}$, from the same site.

The aim of this study was to compare LCV $\boldsymbol{\theta}$ determined from $\boldsymbol{\Phi}$ across the surface of a continuous anisotropic tissue sheet with the values obtained from $\boldsymbol{V_m}$. Furthermore, the influence of the direction of propagation with respect to the fiber direction on the deviation between $\boldsymbol{\theta}$ computed from $\boldsymbol{V_m}$ and from $\boldsymbol{\Phi}$ was examined.
The study was repeated using a computer simulation of a continuous anisotropic tissue sheet with an embedded obstacle. Thus, the deviation between $\boldsymbol{\theta}$ computed from $\boldsymbol{V_m}$ and from $\boldsymbol{\Phi}$ was investigated in the adjacency of a microstructural obstacle.

6.3 Analytic Signal Model of Extracellular Electrogram

An analytic signal model of a nonfractionated unipolar electrogram during depolarization was developed. The signal model is based on sigmoid functions. By variation of four parameters, a wide range of shapes including electrograms emerging from starting, free running, terminating, and colliding wavefronts of activation can be created.
This novel signal model was consequently used for template-based algorithms for the analysis of CNF signals.

6.4 Analysis of Vector Loops of CNF Strength

Vector loops of CNF strength $\boldsymbol{E}$ are being used during experiments to evaluate the local pattern of activation in the underlying tissue. It has been shown in computer simulation studies that the morphology of the vector loop of $\boldsymbol{E}$ indicates the main direction of propagation, is related to the curvature of the wavefront, and may reveal discontinuities in the adjacency of the recording site [62, 79, 80, 69, 81]. It has not been investigated, as to how the imperfect experimental conditions influence the shape of the vector loop of $\boldsymbol{E}$.

In previous studies it was assumed that multisite recordings of extracellular electrograms are taken exactly at the same distance from the surface for all electrodes. During the experiment this cannot be guaranteed because the surface of the tissue is not perfectly planar or may not allow the positioning of the CNF sensor in parallel to the surface. Moreover, the sensor is subjected to aging, particularly due to the exposure to Tyrode's solution. The spacer pillars which maintain a certain distance between the electrodes and the surface of the tissue may break and thus introduce a tilt to the sensor with respect to the tissue surface. As a consequence, unequal distances between the individual electrodes and the surface of the tissue arise. The effects on the determined direction of propagation were investigated by means of electrograms obtained from computer simulation.

Great effort has been made to minimize the influence of noise and power line interference on the acquired CNF signals by proper design of the experimental setup (cf. Section 4.1.1). Nevertheless, a 50 Hz power line interference may hardly be eliminated from the signal recordings. It has not been evaluated how this interference affects $\boldsymbol{E}$ and derived parameters of local impulse propagation.

It was shown that the vector loop of $\boldsymbol{E}$ indicates the angle of local propagation φ in that its tip points opposite to the main direction of the propagating wavefront [62]. In case of fractionated electrograms recorded at sites of parallel, branching, crossing, or merging muscle fibers, abundant in the right atrial isthmus, the time course of the tip of $\boldsymbol{E}$ often describes double or multiple loops. The aim of this computer simulation study was to examine as to how the angles determined from the vector loop of $\boldsymbol{E}$ allow estimating the structure of the underlying tissue, i.e. the crossing angle of fibers beneath the recording position.

6.5 Evaluation of Fractionated Electrograms

Since electrogram fractionation is usually caused by the presence of multiple current sources which differ in strength, distance to the recording site, and activation time, fractionated electrograms may be considered as superimposed nonfractionated components (cf. Section 3.4.2).
In order to quantitatively describe fractionated electrograms, a new measure termed *fractionation index* (FI) was introduced. The integer value FI indicates the number of superimposed nonfractionated components within a fractionated electrogram. In addition to the FI, fractionated electrograms are characterized by the difference between the local activation times of the components (ΔLAT) and the relation of their amplitudes.

6.6 Decomposition of Fractionated Electrograms

The decomposition of fractionated electrograms enables the analysis of its nonfractionated components in terms of amplitude, symmetry, and – for multisite recordings – local conduction velocity and direction of propagation. The number of nonfractionated components and their waveform characteristics can be used as additional features for the classification of the microstructural composition of the tissue in the adjacency of the recording site.
The strategy of the decomposition of a fractionated electrogram Φ is to repeatedly fit in and subtract a template, created by means of the analytic signal model introduced in Section 6.3.

6.7 Discrimination of Local and Distant Activation

Extracellular electrograms not only represent the activation of a single cardiomyocyte but emerge from the spatio-temporal integration of current sources in the recording area (cf. Section 2.1.4). Especially when fractionated electrograms are recorded, it is desirable to estimate the distance z between recording site and current sources, i.e. the myocardial fibers, or at least to distinguish which deflection represents local and which one remote activation, in order to assign correct local activation times. When the source strengths are equal, as given for the theoretical example of muscle fibers with equal geometric (e.g. diameter) and electrophysiological properties (e.g. conduction velocity, curvature of propagating activation wave), the amplitude of Φ, Φ_{pp}, gives a measure of the distance, because Φ_{pp} falls with increasing distance to the current source (see Equation 2.1). The amplitude of the temporal derivative $\dot{\Phi}_{pp}$, has been used to distinguish local and distant activation, as shown in experimental studies [116, 117]. In general, muscle fibers show individual properties and the task of estimating the distances between current sources and deflections within a fractionated electrogram Φ may become more complicated. As extreme case activations from a strong distal source (e.g. a thick fiber bundle) and a weak local source superimposed within Φ can be considered.

An approach to this issue is finding a ratio between two parameters extracted from Φ, which both change with increasing distance but at a different rate. Spach and Dolber showed that for a cylindric fiber the amplitude of the second derivative of Φ with respect to time $\ddot{\Phi}_{pp}$ falls more rapidly with the distance than the amplitude of the first derivative $\dot{\Phi}_{pp}$ [66]. They suggested therefore to use the ratio $\ddot{\Phi}_{pp} : \dot{\Phi}_{pp}$ as an estimator of z. Hofer *et al.* observed that $|\dot{\boldsymbol{E}}|_{pp}$, the amplitude of the temporal derivative of the magnitude of CNF strength $|\boldsymbol{E}|$, decreases at a higher rate with increasing z than $|\boldsymbol{E}|_{pp}$ and thus suggested using the ratio $|\dot{\boldsymbol{E}}|_{pp} : |\boldsymbol{E}|_{pp}$ as a measure of locality of the observed electrogram deflection [118].

Chouvarda *et al.* have used a dipole model as well as a nonlinear model to represent the time course of the transmembrane current and the volume conductor equation and an optimization procedure to solve the inverse problem of determining the distance z between current source and recording site [119]. They yielded promising results, as the estimation error for z was below $50\,\mu$m. However, the method required the accurate determination of the local conduction velocity and noise dramatically deteriorated the results. The method was based on a very simple anatomical model of a myocardial bundle as one-dimensional strand of current sources.

The aim of this study was to examine the two proposed morphological measures, $\ddot{\Phi}_{pp} : \dot{\Phi}_{pp}$ and $|\dot{\boldsymbol{E}}|_{pp} : |\boldsymbol{E}|_{pp}$ determined at varying distances z from the surface of fibers with different diameters and tissue sheets incorporating anisotropy, elliptic propagation of activation, and structural heterogeneities.

The experimental study was intended to examine the feasibility of determining the proposed measures. Specifically, the influence of noise and measurement artifacts on the parameters and the size of the calculated ratios and their accordance with values obtained from computer simulations was investigated.

6.8 Classification of Tissue Microstructure through CNF Signals

The presented CNF measurement technique allows the resolution of discontinuous activation in the submillisecond range resulting from structural discontinuities in the submillimeter range as for instance caused by fibrosis. One major challenge for this technique is the characterization of the microstructure of the underlying tissue through recorded electrograms. With regard to the achieved spatio-temporal resolution, particularly the distinction between normal and fibrotic tissue, as well as the classification into different types and degrees of fibrosis is desirable.

Currently, there is no common quantitative definition of certain classes of fibrosis. Qualitatively, a distinction between patchy fibrosis and diffuse fibrosis has been made. Patchy fibrosis is characterized by longitudinal compact inlays of fibrotic strands, diffuse fibrosis by short strands [22]. Kawara *et al.* have shown that not only the amount of fibrosis, i.e. the percentage of fibrosis in terms of area, but as well the texture of fibrosis is essential for the activation pattern [120]. They compared impulse propagation in tissue with patchy fibrosis and diffuse fibrosis at the same percentage, and observed that the former leads to increased conduction delays.

The characterization of the microstructure of the tissue through electrograms requires the classification of microstructure from histological images from the recording area. The procedure of embedding and slicing the preparation, as described in Section 4.1.4, causes shrinkage, morphologic distortions, and clefts. For these reasons, the annotation between histograph and macroscopic digital image and thus the recording position with the necessary accuracy has turned out to be unfeasible.

Therefore, as a first approach to classification of the microstructure through CNF signals, the histologically detailed computer model of rabbit atrium described in Section 4.2 was used.

The computer simulation study has been carried out in order to classify myocardium in terms of its microstructure into three classes: 1.) well coupled tissue, 2.) tissue with longitudinal inlays, and 3.) tissue with complex distribution of inlays of connective tissue.

It was demonstrated in Section 3.4.2 that electrogram fractionation may depend on the direction of impulse propagation. The basic idea of the study was to vary the stimulus site in order to induce different directions of propagation while recording electrograms in a certain region of interest. Dependent on the type of tissue, the parameters extracted from the recorded electrograms are expected to show different behavior. The study examines the ability in classifying the type of tissue from features extracted from electrograms recorded during varying direction of propagation of activation.

Chapter 7

Methods

In this Chapter, the methods to obtain the results presented in Chapter 8 are described.

7.1 Signal and Noise Analysis of CNF Signals

7.1.1 Statistical Analysis of CNF Signal Parameters

In order to statistically evaluate CNF signal properties, a set containing 566 multivariate electrograms $\mathbf{\Phi} = [\Phi_1\ \Phi_2\ \Phi_3\ \Phi_4]^T$ recorded at 566 different positions during 9 electrophysiological experiments with preparations of the rabbit's right atrial isthmus was created. This *set A* was separated into two sets containing nonfractionated or fractionated waveforms, respectively, using the *SM* algorithm described in Section 7.5.2. From both sets 200 waveforms were randomly chosen, resulting in *set I* containing 200 nonfractionated waveforms of $\mathbf{\Phi}$ and *set II* containing 200 fractionated waveforms of $\mathbf{\Phi}$. The waveforms were bidirectionally lowpass filtered (4^{th} order Butterworth-type, cutoff frequency $f_C = 1.5\,\text{kHz}$).

The signal quality of a recorded unfiltered electrogram Φ was quantified by means of the amplitude-to-noise ratio (ANR) [76], which calculates as follows:

$$\text{ANR} = 20 \log_{10} \frac{\Phi_{pp}}{\sigma_N}, \tag{7.1}$$

where Φ_{pp} is the peak-to-peak amplitude of Φ, and σ_N is the standard deviation of the noise which was determined in a quiescent section of the recording.

Φ_{pp} and its temporal derivative $\dot{\Phi}_{pp}$ as well as fractionation index FI (see Section 7.5.2) and ANR were determined from Φ_1. The maximum of the CNF strength $|\boldsymbol{E}|_p$ was determined from $\mathbf{\Phi}$.

The probability distributions of Φ_{pp}, $\dot{\Phi}_{pp}$, ANR, and $|\boldsymbol{E}|_p$ from *set I* and *set II* were compared using a Mann-Whitney-U test[1].

From the distributions of ANR, lower quartile $\text{ANR}_{.25}$, median $\text{ANR}_{.50}$, and upper quartile $\text{ANR}_{.75}$ for *set A*, *set I*, and *set II* were computed.

Furthermore, the correlation matrix of the variables FI, Φ_{pp}, $\dot{\Phi}_{pp}$, ANR, and $|\boldsymbol{E}|_p$ was calculated.

7.1.2 Analysis of Noise in the Measurement Chain

In the absence of a tissue preparation, electric potential signals of 1 s duration were recorded in the tissue bath filled with Tyrode's solution and digitized using the measurement system described in Section 4.1.1. Thus, the noise signal induced by the entire measurement chain containing electrode-electrolyte interface, CNF sensor, impedance converter, preamplifier, main amplifier, cables, and DAQ board was acquired. The noise signal induced by the amplifier chain was acquired by a recording of 1 s duration without the CNF sensor and with all input channels of the preamplifier connected to signal ground. The quantization noise of the ADC was simulated by generating a noise signal with an amplitude range of $\pm q/2$ with uniform distribution[2], where q is the voltage resolution of the ADC (cf. Section 4.1.1).

The power spectral densities (PSD's) of quantization noise, amplifier noise, and measurement noise were estimated using Welch's method with 50 segments and 50% overlap [123]. The acquired noise signal was lowpass filtered (4^{th} order Butterworth type, $f_C = 100\,\text{Hz}$). Its peak-to-peak amplitude $\text{A}_{\tilde{\Phi}}$ was considered as the amplitude of the 50 Hz power line interference signal.

7.1.3 Frequency Analysis of CNF Signals

It has been shown that the volume conductor surrounding the tissue is a low pass filter for extracellular potential waveforms [124] and that its cutoff frequency decreases with increasing distance between current sources and measurement position. To determine the highest relevant frequency components that may occur in CNF measurements, an extracellular electrogram Φ_{sim} was computed directly, i.e. $1\,\mu$m above the surface of a computer simulated sheet of cardiac tissue. As a comparison Φ_{sim} was computed $50\,\mu$m above the surface, which corresponds to the distance between surface and electrodes of CNF sensors used in the electrophysiological experiments. The PSD was estimated using Welch's method with 50 segments and 50% overlap.

---

[1] The Mann-Whitney-U test was chosen for variance analysis because a Lilliefors composite goodness of fit test has shown that none of the compared variables are normally distributed [121].

[2] The assumptions enabling the presented statistical considerations are described in [122, p.194].

7.2 Determination of Local Conduction Velocity

7.2.1 Uncertainty Due to Temporal Discretization

In the absence of noise, the uncertainty of magnitude θ and direction φ of the LCV is dependent on the value of θ, the inter-electrode distance DD, and the sampling rate f_S. To quantify the uncertainty of θ, a simplified arrangement consisting of two electrodes was considered.

The latency of the propagating impulse between the electrodes causes a temporal shift t_D between the simultaneously acquired waveforms Φ_1 and Φ_2. The magnitude θ of the LCV is:

$$\theta = \frac{\mathrm{DD}}{t_D}$$

The absolute deviation Δt_D is dependent on the temporal resolution of the digitized waveforms Φ_1 and Φ_2, i.e. the sampling interval T_S and the sampling rate $f_S = 1/T_S$, respectively:

$$\Delta t_D = \pm T_S = \pm \frac{1}{f_S}$$

As a consequence, the absolute deviation in θ, calculated by the propagation of uncertainty is:

$$\Delta\theta = \mp \frac{\theta^2}{f_S \cdot \mathrm{DD}} \tag{7.2}$$

The uncertainty of the direction of propagation φ is examined using an arrangement of two orthogonal electrode pairs with equal inter-electrode distance DD. The electrode pairs allow determining the longitudinal and transversal conduction velocities θ_l and θ_t. Velocity θ and angle φ in the main direction of propagation calculate as follows:

$$\theta = \sqrt{\theta_l^2 + \theta_t^2}$$

$$\varphi = \arctan \frac{\theta_t}{\theta_l}$$

The absolute deviation in $\Delta\varphi$ is:

$$\Delta\varphi = \arctan \frac{\Delta\theta}{\theta} = \arctan \mp \frac{\theta}{f_S \cdot \mathrm{DD}} \tag{7.3}$$

Equations 7.2 and 7.3 show that for given inter-electrode distance DD the uncertainty in the determination of LCV can be decreased by increasing the sampling rate f_S or rather by digital resampling of the acquired electrograms.

Digital Resampling

The chosen method for increasing the temporal resolution of electrograms Φ is sinc-interpolation by zero padding in the frequency domain. The extracted signal is windowed using a rectangular window with length N and Fast Fourier transformed (FFT). The frequency domain signal is extended by $\mathrm{N} \cdot (\mathrm{M}-1)$ zeros and transformed to time domain using inverse FFT. Thus, almost arbitrary interpolation factors M can be achieved, provided that the sampling theorem was satisfied when acquiring the waveforms [125].

In order to evaluate the digital resampling and the theoretical considerations concerning the uncertainty of LAT delays, two extracellular electrograms Φ_{h1} and Φ_{h2} with a temporal resolution of $1\,\mu$s were created by 1D-computer simulation. The local activation times of Φ_{h1} and Φ_{h2} differed by $\Delta\mathrm{LAT}_h = 70\,\mu\mathrm{s}$, which – assuming an inter-electrode distance $\mathrm{DD} = 70\,\mu\mathrm{m}$ – corresponds to an LCV $\theta = 1\,\mathrm{m/s}$.
The temporal resolution of Φ_{h1} and Φ_{h2} was reduced by a factor of 50, which corresponds to the downsampling to $f_S = 20\,\mathrm{kHz}$. The decimation phase was varied from $i = 0 \ldots 49$ and electrograms Φ_{l1_i} and Φ_{l2_i} were obtained. Then the decimated electrograms were sinc-interpolated by a factor of 50 and the respective LAT_{1_i} and LAT_{2_i} were calculated. The range of $\mathrm{LAT}_{2_i} - \mathrm{LAT}_{1_i}$ was determined and compared to the uncertainty due to the temporal resolution of Φ_{h1} and Φ_{h2} ($1\,\mu$s).

7.2.2 Uncertainty Due to Noise

Two different anatomical substrates were analyzed. a) A cable-like strand of cells with atrial membrane kinetics (Lindblad *et al.* model [126] of rabbit atrium) and b) a continuous anisotropic tissue sheet ($4000\,\mu\mathrm{m} \times 1250\,\mu\mathrm{m}$) with ventricular membrane kinetics (Beeler-Reuter-Drouhard-Roberge model of general mammalian ventricle [127]). The fiber orientation was defined in the long axis of the tissue sheet by introducing a transversal-to-longitudinal anisotropy ratio of 0.174. This setup is illustrated in Figure 7.1. Point-like stimuli were applied to the tissue at the indicated positions to induce longitudinal elliptic propagation (b1), transversal elliptic propagation (b2), and oblique elliptic propagation (b3), respectively.

Four extracellular potentials $\mathbf{\Phi}$ were computed in a square with $50\,\mu$m lateral length, centered in the tissue sheet, in a plane $50\,\mu$m above the surface. The tolerance band for φ was chosen $\pm 20°$ which even in worst case should enable a distinction between longitudinal, oblique, or transversal propagation with respect to the fiber orientation. The tolerance band for θ was chosen $\pm 0.1\,\mathrm{m/s}$ which gives a maximum uncertainty of $20\,\%$ in case $\theta = 0.5\,\mathrm{m/s}$. Reference values for θ and φ were taken from noise-free waveforms $\mathbf{\Phi}$. ANR was varied from 70 down to 15 in steps of 1. For each value of ANR, Gaussian white noise with corresponding level was generated and added to $\mathbf{\Phi}$. Then, $\mathbf{\Phi}$ was bidirectionally

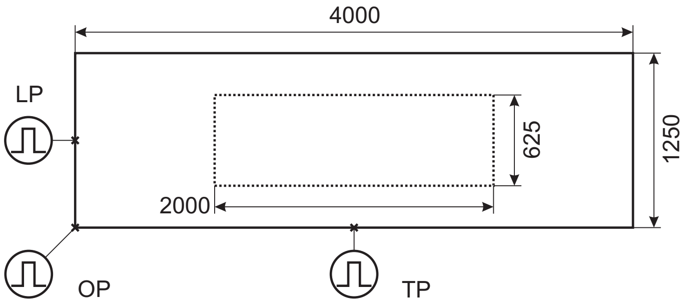

Figure 7.1: Computer simulation setup of a 2D-sheet of cardiac tissue. Stimulus positions to induce longitudinal elliptic (LP), transversal elliptic (TP), and oblique elliptic (OP) wavefronts of propagation of activation are indicated. The section demarcated by dashed line was considered for signal analysis. Dimensions are given in μm.

filtered using a lowpass filter (4^{th} order Butterworth type), whose cutoff frequency f_C was varied from 5 kHz down to 200 Hz. The filtered waveforms were sinc-interpolated with factor 20 to increase the temporal resolution to 0.5 μs.

LCV's (θ and φ) were computed using the minimum derivative method (*dmin method*) and the cross correlation method (*CCF method*). Additionally, φ was determined from the CNF strength $\boldsymbol{E}$ (*Emag method*). A detailed explanation of these methods is given in Section 3.3.2.

For each pair of ANR and f_C, θ and φ were computed 100 times with regenerated noise. The uncertainty of θ and φ was expressed as the three-fold standard deviation of the respective 100 values.

Hence, for each f_C, the minimum ANR was determined, at which the uncertainty of θ and φ, respectively, remains within the given tolerance band.

The following computer simulation study was carried out to obtain the uncertainty of θ and φ for the range of values of ANR and θ which can be expected during electrophysiological experiments with the described setup (see Section 4.1.1). A noise-free extracellular potential $\Phi_1(t)$ was obtained from a computer simulation with the setup a). The four waveforms $\boldsymbol{\Phi} = \Phi_1(t) \ldots \Phi_4(t)$ according to the sensor described in [54] were obtained by copying $\Phi_1(t)$ and shifting it in time. Thus, propagation velocities θ in a range of 0.1 m/s to 2 m/s in steps of 0.05 m/s were mimicked. Again, the ANR was varied from 70 down to 15 in steps of 1. Gaussian white noise with respective level was added to $\boldsymbol{\Phi}$. For each tuple (θ, ANR), noise was regenerated 100 times and the three-fold standard deviations $3\sigma_\theta$ and $3\sigma_\varphi$ of θ and φ, determined using the *CCF method* and the *Emag method*, respectively, were calculated.

7.2.3 Comparison to LCV Determined from Transmembrane Voltages

The computer model of a 2D-sheet of cardiac tissue (depicted in Figure 7.1) was used. A point-like stimulus was applied to the tissue at positions LP, TP, and OP to induce a) longitudinal elliptic propagation (LP), b) transversal elliptic propagation (TP), and c) oblique elliptic propagation (OP), respectively.

In order to exclude possible artifacts within $\mathbf{\Phi}$ due to the borders of the simulated tissue, a rectangle of $2000\,\mu\mathrm{m} \times 625\,\mu\mathrm{m}$ was extracted from the center of the tissue sheet for signal analysis. LCV (magnitude θ and direction φ) was calculated in a grid of $50\,\mu\mathrm{m}$ lateral length from $\boldsymbol{V}_m$ (θ_{Vm}, φ_{Vm}) and $\mathbf{\Phi}$ (θ_Φ, φ_Φ). The deviation of θ, $e_\theta = \theta_\Phi - \theta_{Vm}$ and the deviation of φ, $e_\varphi = \varphi_\Phi - \varphi_{Vm}$ were calculated for each grid point.

The study was repeated with a nonconducting obstacle ($500\,\mu\mathrm{m} \times 50\,\mu\mathrm{m}$) embedded in the center of the tissue sheet. OP was induced and θ_{Vm}, φ_{Vm}, e_θ, and e_φ were computed.

7.3 Analytic Signal Model of Extracellular Electrogram

7.3.1 Signal Model

The template $\Phi_m(t)$, centered at $t = 0$ consists of four sigmoid functions: The positive phase of the biphasic waveform $\Phi_m(t)$ is created by multiplication of the rising function $s_{PR}(t)$ and the falling function $s_{PF}(t)$. Likewise, the negative phase consists of $s_{NR}(t)$ and $s_{NF}(t)$. The function $\Phi_m(t)$ is described by four parameters $[a\ b\ c\ d]^T$, where b, c, and d determine the waveform of the sigmoids and a scales the overall function.

$$\begin{aligned}
\Phi_m(t) &= a\,(s_{PR}(t)\,s_{PF}(t) - s_{NR}(t)\,s_{NF}(t)) \\
s_{PR}(t) &= \frac{b}{1+\exp(-tb)} \\
s_{PF}(t) &= \frac{c\,\exp(-tc)}{1+\exp(-tc)} \\
s_{NR}(t) &= \frac{c}{1+\exp(-tc)} \\
s_{NF}(t) &= \frac{d\,\exp(-td)}{1+\exp(-td)}
\end{aligned}$$

Figure 7.2 illustrates the generation of $\Phi_m(t)$ and shows the modeling of waveforms which represent initiating, free running, and colliding wavefronts of activation by variation of $[a\ b\ c\ d]^T$.

7.3.2 Curve Fitting

The task of finding a set of the four parameters $[a\ b\ c\ d]^T$ for which $\Phi_m(t)$ best fits a given waveform $\Phi(t)$ was solved by nonlinear curve fitting in least-squares sense using the Trust-

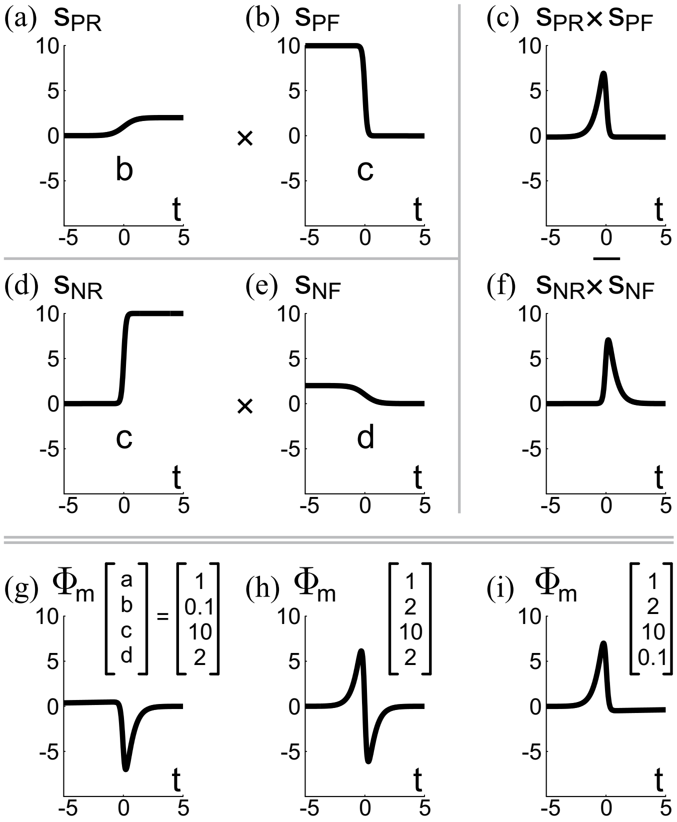

Figure 7.2: Modeling of depolarization waveform $\Phi_m(t)$, $t = -5 \dots 5$ in steps of 0.01. Amplitude and time scales are dimensionless. Subfigures *(a)-(f)* illustrate the composition of $\Phi_m(t)$ *(h)* by sigmoid functions $s_{PR}(t)$, $s_{PF}(t)$, $s_{NR}(t)$, and $s_{NF}(t)$. The coefficients for the sigmoids are indicated in subfigures *(a)*, *(b)*, *(d)*, and *(e)*. Subfigures *(g)-(i)* show starting, free running, and terminating or colliding waveforms and respective parameters $[a\ b\ c\ d]^T$. Figure adopted from [128].

Table 7.1: Choice of start, minimum, and maximum coefficients for the optimization process. Φ_{pp}: amplitude of $\Phi(t)$, Φ_{max}: magnitude of positive phase of $\Phi(t)$, $\left|\dot{\Phi}_{min}\right|$: amplitude of $\dot{\Phi}(t)$, $|\Phi_{min}|$: magnitude of negative phase of $\Phi(t)$.

Coefficient	Initialization	Minimum value	Maximum value
a	$a_1 := \frac{\Phi_{pp}}{2}$	$a_l := \frac{\Phi_{pp}}{400}$	$a_h := 4 \cdot \Phi_{pp}$
b	$b_1 := \frac{\Phi_{max}}{\Phi_{pp}}$	$b_l := \frac{1}{1000} \frac{\Phi_{max}}{\Phi_{pp}}$	$b_h := 20 \frac{\Phi_{max}}{\Phi_{pp}}$
c	$c_1 := 5 \frac{\left\|\dot{\Phi}_{min}\right\|}{\Phi_{pp}}$	$c_l := \frac{1}{5} \frac{\left\|\dot{\Phi}_{min}\right\|}{\Phi_{pp}}$	$c_h := 20 \frac{\left\|\dot{\Phi}_{min}\right\|}{\Phi_{pp}}$
d	$d_1 := \frac{\|\Phi_{min}\|}{\Phi_{pp}}$	$d_l := \frac{1}{1000} \frac{\|\Phi_{min}\|}{\Phi_{pp}}$	$d_h := 20 \frac{\|\Phi_{min}\|}{\Phi_{pp}}$

Region-Reflective method (MATLAB function `lsqcurvefit`) [113]. The depolarization time t_{dep} was determined. $\Phi(t)$ was windowed using a rectangular window of $t_W = 4\,t_{dep}$ length. Start coefficients $[a_1\ b_1\ c_1\ d_1]^T$, minimum coefficients $[a_l\ b_l\ c_l\ d_l]^T$, and maximum coefficients $[a_h\ b_h\ c_h\ d_h]^T$ were calculated from $\Phi(t)$ following empirically established rules (see Table 7.1). The maximum number of function evaluations was chosen 2000, the termination tolerance for the function value was set to $tol = \Phi_{pp} \cdot 10^{-4}$.

The ability of the proposed signal model to represent a wide range of nonfractionated electrograms was tested using a computer simulation of a one-dimensional cable-like fiber of 20 mm length.

Extracellular potentials $\Phi(t)$ were computed at different positions x along the fiber ($x = 0$ mm, 10 mm, and 20 mm) representing starting, free running, and terminating propagation and at different distances z from the surface of the fiber ($z = 5$, 250, and 500 μm) representing local and remote activation events. Moreover, membrane kinetic models for atrial (LMCG) as well as ventricular activation (MSH) were used [126, 11]. For each x and z as well as for both membrane kinetic models, the curve fitting procedure was applied to $\Phi(t)$ to obtain a modeled waveform $\Phi_m(t)$.

The goodness of fit was quantified by a) the sum of the squared errors sse_Φ, which calculates as follows:

$$sse_\Phi = \frac{\sum\limits_{t=0}^{N-1} (\Phi_m(t) - \Phi(t))^2}{\sum\limits_{t=0}^{N-1} (\Phi(t))^2}, \tag{7.4}$$

where N is the length of the sequences $\Phi(t)$ and $\Phi_m(t)$ and b) the Pearson product-moment correlation coefficient r_Φ between $\Phi(t)$ and $\Phi_m(t)$. Likewise, $sse_{\dot{\Phi}}$ and $r_{\dot{\Phi}}$ were determined for the temporal derivative.

7.4 Analysis of Vector Loops of CNF Strength

7.4.1 Influence of Unequal Distances between Electrodes and Tissue

The influence of unequal distances between the electrodes and the surface of the tissue under examination on the determined angle of impulse propagation φ was investigated using the computer model described in Section 7.2.3. Two scenarios were taken into consideration: a) altered distance Δz from the tissue surface of one of the four electrodes and b) Δz of two electrodes. In both scenarios, all options, i.e. Δz for any electrode or any electrode pair, were evaluated and the respective worst case in terms of deviation in φ was selected. Assuming a regular distance of $50\,\mu$m from the surface, Δz was varied from 5 to $50\,\mu$m in steps of $5\,\mu$m. Thus, a maximum tilt of the CNF sensor of 45° with respect to the tissue surface was mimicked. A further tilt would certainly be noticed by the experimenter and the repositioning of the sensor would be initiated. To simulate sensor tilt by broken spacer pillars, Δz$= -5\,\mu$m and Δz$= -10\,\mu$m were evaluated.
The angle of impulse propagation was determined on one hand from the CNF strength $\boldsymbol{E}$ (φ_E) and on the other hand from the vector of local conduction velocity $\boldsymbol{\theta}$ (φ). For both scenarios – Δz effective on one or two electrodes – the respective deviations from φ_0 in the absence of a Δz (eφ_E and eφ) were calculated for different values of Δz.

7.4.2 Influence of Power Line Interference

Multivariate electrograms $\boldsymbol{\Phi}$ of 10 ms duration were obtained with the computer model described in Section 7.2.3 and perturbed by adding an artificial sinusoidal interference signal. Two scenarios were taken into consideration: a) effective power line interference in one channel (Φ_1) and b) effective power line interference in two channels (Φ_1 and Φ_2). In the latter case, two channels whose waveforms are not subtracted from each other when computing $\boldsymbol{E}$ (see Equations 3.2 and 3.3) were perturbed to the same extent.
A sinusoid $\tilde{\Phi}$(t) with frequency $f = 50$ Hz and variable amplitude and phase was generated and added to Φ_1, or Φ_1 and Φ_2, respectively. The relation of the amplitude of $\tilde{\Phi}$(t) and Φ_1 (A$_{\tilde{\Phi}}$/A) was varied from 0 . . . 20 % in steps of 1 %, the phase angle ζ was varied from 1 . . . 360° in steps of 1°. For each value of ζ and A$_{\tilde{\Phi}}$/A, the absolute deviation in angle $e_\varphi = |\varphi_E - \varphi_0|$ was computed, where φ_0 is the angle in the undisturbed case. For each value of A$_{\tilde{\Phi}}$/A, the maximum value of e_{φ_E} for varying ζ was determined.
Moreover, it was examined if e_{φ_E} could be reduced by elimination of linear or quadratic trend in $\boldsymbol{\Phi}$ using curve fitting in the least-squares sense [114].

7.4.3 Estimation of Crossing Angle of Fibers

The computer simulation setup is illustrated in Figure 7.3. Two fibers crossing each other at half of their length in an angle $\alpha = 90°$ were represented by a 2D-monodomain

model of two continuous anisotropic tissue layers (10 mm × 10 mm) separated by 25 μm with perpendicular fiber direction. The areas around the cable-like fibers were set to be isolating. Membrane kinetics were modeled by the Lindblad *et al.* model [126]. At positions A and B, point-like stimuli of 1 ms duration were induced. Discretization steps were 25 μs in space and 10 μs in time. Extracellular potentials were recovered 50 μm above the surface in a grid of 25 μm. Transversal to longitudinal conductivity ratio was set to 0.174, longitudinal conduction velocity was 0.5 m/s.
By stimulation of fiber I at position A and – after a time delay ΔLAT – fiber II at position B, fractionated electrograms with two components were obtained at the point of observation (1). The crossing angle was varied from $0 \leq \alpha \leq 180°$ in steps of 5°. Thus, crossing, parallel, and antiparallel (i.e. parallel but with opposite directions) fibers could be mimicked.

For each component, the direction of local propagation (φ) was determined at the instants of peak magnitude of $\boldsymbol{E}$ (cf. Section 3.3.2). Peaks higher than 20 % of the maximum peak amplitude were taken into consideration. The deviations in φ for the two components ($e_{\varphi 1}$ and $e_{\varphi 2}$) were obtained as follows:

$$e_{\varphi} = |\varphi - \alpha|$$

The deviations $e_{\varphi 1}$ and $e_{\varphi 2}$ as functions of α were determined for two time delays $\Delta\text{LAT}_1 = 1$ ms and $\Delta\text{LAT}_2 = 1.5$ ms.
Furthermore, ΔLAT was varied from $\Delta\text{LAT} = 3 \ldots 1$ ms in steps of -0.1 ms. For each value of ΔLAT, $|\hat{e}_{\varphi 1}|$ and $|\hat{e}_{\varphi 2}|$, the maximum deviations of $e_{\varphi 1}(\alpha)$ and $e_{\varphi 2}(\alpha)$ were computed.

7.5 Evaluation of Fractionated Electrograms

To determine the fractionation index (FI) of an electrogram Φ, two algorithms have been developed: 1) A simple peak counting within the temporal derivative $\dot{\Phi}$, termed *pCt* and 2) a cross correlation-based algorithm, *SM*, which uses a template of Φ created by means of the analytic signal model described in Section 8.3.

7.5.1 Peak Counting Algorithm (pCt)

Fractionated electrograms Φ are characterized by multiple bipolar deflections and consequently multiple negative peaks in the temporal derivative $\dot{\Phi}$. The straightforward approach to determining the number of superimposed nonfractionated components (FI) is thus to count the negative peaks within $\dot{\Phi}$.
The algorithm requires two input variables, a threshold th and a separation time t_{sep} which specifies the minimum time between subsequent peaks. The appropriate choice of t_{sep} is necessary to avoid counting one peak within $\dot{\Phi}$ several times, when the waveform

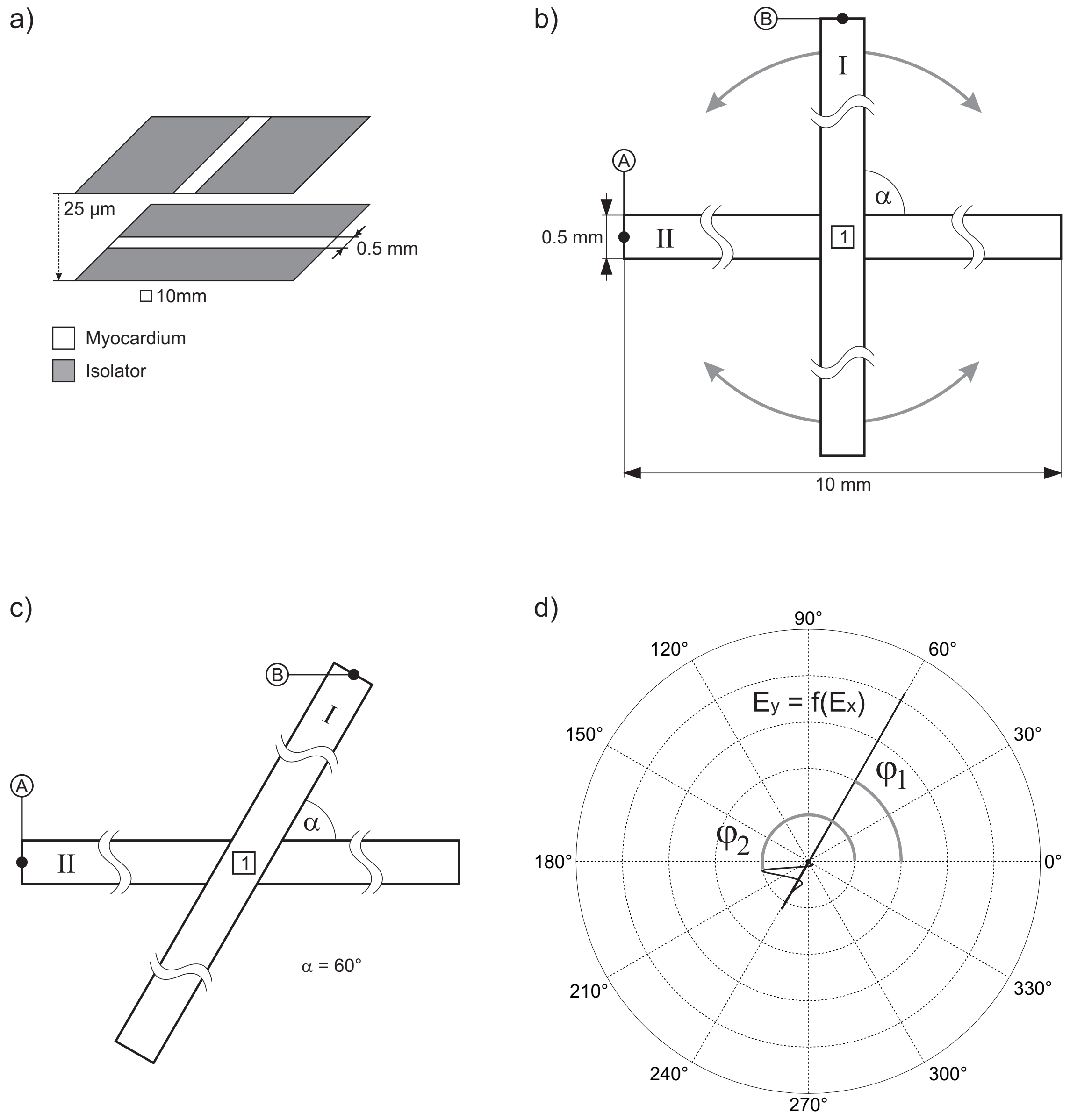

Figure 7.3: Setup for the simulation of two crossing fibers. *a)* Two layers of tissue form crossing fibers. *b)* Two fibers (I and II) crossing at angle α. Stimulus sites (A, B) are marked with circles, the point of observation (1) with a square. The crossing angle can be adjusted from $0 \leq \alpha \leq 180°$. Subfigure adopted from [129]. *c)* Example arrangement for $\alpha = 60°$. *d)* Corresponding vector loop of $\boldsymbol{E}$ exhibiting two tips pointing at φ_1 and φ_2.

is perturbed by noise or the peak is not well-defined. Peaks higher than $th \cdot (-\dot{\Phi})_p$ are counted, where $(-\dot{\Phi})_p$ is the magnitude of the maximum negative peak. The threshold has been set to $th = 0.1$. The output values of the algorithm are the fractionation index (FI) and the vector (length FI) of local activation times (**LAT**) of the components.

7.5.2 Signal Model Algorithm (SM)

This cross correlation-based algorithm uses a template of $\dot{\Phi}$ created by means of the analytic signal model of Φ introduced in Section 7.3. The block diagram shown in Figure 7.4 illustrates the procedure. The template Φ_m with the duration $t_W = 16t_{dep}$ is created by means of the signal model using the coefficients $[a \ b \ c \ d]^T = \left[\Phi_{pp}/4 \quad 2\Phi_{max}/\Phi_{pp} \quad |\dot{\Phi}_{min}|/2 \quad |\Phi_{min}|/\Phi_{pp}\right]$ and differentiated with respect to time ($\dot{\Phi}_m$). Φ is bidirectionally lowpass filtered (Butterworth IIR, 4^{th} order, $f_C = 1.5\,\mathrm{kHz}$) and temporally differentiated ($\dot{\Phi}$). A window of duration t_W is extracted around the maximum negative peak of $\dot{\Phi}$. The cross correlation function $c_{\dot{\Phi}\dot{\Phi}_m}(\tau)$ of $\dot{\Phi}$ and the temporal derivative $\dot{\Phi}_m$ of the modeled waveform Φ_m is calculated by fast correlation in the frequency domain [122, p.746]. The second derivative of $c_{\dot{\Phi}\dot{\Phi}_m}(\tau)$ with respect to τ is calculated and multiplied with a Kaiser window to attenuate artifacts at the borders of the waveform induced by the differentiation operations. From $\ddot{c}_{\dot{\Phi}\dot{\Phi}_m}(\tau)$, peaks with a magnitude above 20 % of the maximum peak are identified. The number of peaks as well as their instants of time and magnitudes relative to the maximum peak are determined. These values represent FI, the vector of local activation times (**LAT**), and the vector of magnitudes (**A**).

7.5.3 Evaluation of FI Detection Algorithms

In order to evaluate the limitations of the algorithms *pCt* and *SM* to determine the FI, the following computer simulation study has been carried out. Two nonfractionated electrograms Φ_1 and Φ_2 were added to generate a fractionated electrogram Φ_{12}. The latency between the LAT's of Φ_1 and Φ_2, ΔLAT, was varied by temporally shifting Φ_2 against Φ_1 in the range of 2 ms down to 0 ms in steps of 0.05 ms. Φ_1 was computed 50 μm above the surface, corresponding to the dimensions of CNF sensors [54]. Because differences in amplitude between the components of fractionated electrograms are usually due to the different distances between measurement site and current sources of the individual components, the distance z from the surface in which Φ_2 was recovered was varied from 50 μm to 300 μm in steps of 5 μm. Thus, the relation A_2 of the amplitudes of Φ_2 and Φ_1 varied from 1 down to 0.24 in a nonlinear manner, inversely proportional to the distance z. The robustness of the algorithms against noise was evaluated by regenerating and adding noise 100 times for each pair (ΔLAT , A_2) and calculating the mean of the FI from these 100 runs. The noise level was set to achieve an amplitude-to-noise ratio ANR = 38 dB, which corresponds to the lower quartile of the ANR-distribution from fractionated electrograms determined from electrophysiological experiments in the rabbit's right atrial isthmus (see Section 8.1.1 and Table 8.1).

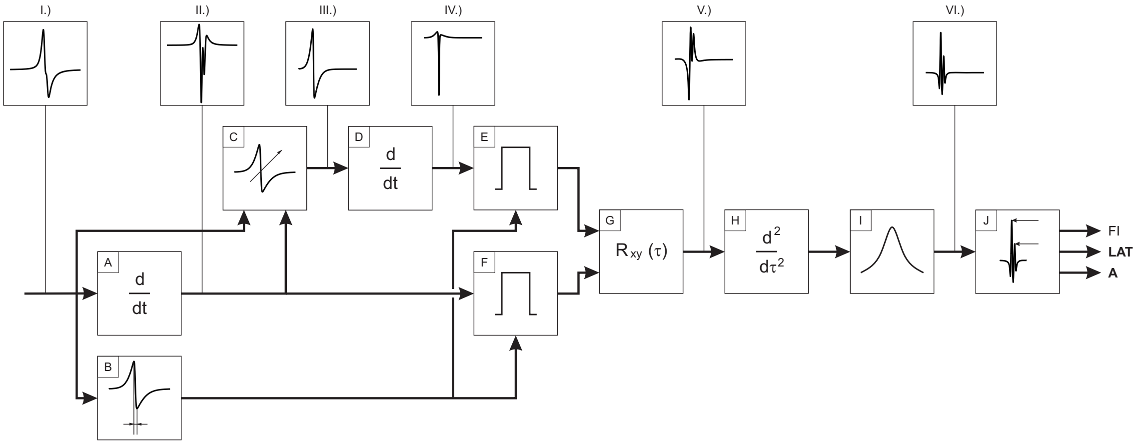

Figure 7.4: Block diagram of the algorithm *SM* for the detection of the fractionation index (FI): *A*: Differentiation, *B*: Determination of the depolarization duration t_{dep}, *C*: Signal generation using analytic signal model, *D*: Differentiation, *E,F*: Rectangular windowing, *G*: Calculation of cross correlation, *H*: Differentiation (second derivative), *I*: Windowing using Kaiser window, *J*: Peak detection algorithm. I.) Input waveform Φ, II.) Temporal derivative $\dot{\Phi}$, III.) Modeled waveform Φ_m, IV.) Temporal derivative of modeled waveform $\dot{\Phi}_m$, V.) Cross correlation function $c_{\dot{\Phi}\dot{\Phi}_m}(\tau)$, VI.) Second temporal derivative $\ddot{c}_{\dot{\Phi}\dot{\Phi}_m}(\tau)$.

7.6 Decomposition of Fractionated Electrograms

The decomposition of fractionated electrograms is performed by repeated application of the curve fitting procedure described in Section 7.3.
The curve fitting procedure is carried out in n iterations $i = 1 \ldots n$. Hence, it is applied $n\,\mathrm{FI}$ times centered at the local activation time LAT_k, $k = (j-1 \mod \mathrm{FI})+1$, $j = 1..n\,\mathrm{FI}$. Window size and termination tolerance for the optimization procedure are adapted as follows: $t_W = t_{dep}2^{2(i-1)}$, $tol = \Phi_{pp}10^{-(i+3)}$. After each iteration j, $\Phi_{m,j}(t)$ is modeled using the determined coefficients. For $i = 1$ the coefficients for the FI components are determined by fitting the signal model into $\Phi_j = \Phi - \sum_{k=1}^{j-1} \Phi_j$. For $i > 1$ the curve fitting is done for $\Phi_j = \Phi - \sum_{k=1}^{FI}(\Phi_{m,l})_{l=FI\,(i-2)+k,\, l\neq j-FI}$. Because the subtraction of modeled components might alter the LAT's, the respective LAT is recomputed prior to the curve fitting. The resulting components are $\Phi_{m,(n-1)\,FI+1}..\Phi_{m,n\,FI}$.

The goodness of fit was quantified by a) the sum of the squared errors sse_Φ (see Equation 7.4) and b) the Pearson product-moment correlation coefficient r_Φ between $\Phi(t)$ and $\Phi_m(t)$. Likewise, $sse_{\dot{\Phi}}$ and $r_{\dot{\Phi}}$ were determined for the temporal derivative.
Figure 7.5 shows the decomposition procedure for $n = 3$. With i the fit improves, i.e. sse decreases and r increases. For the choice of n a trade-off between goodness of fit and computation time has to be made. In the following, $n = 5$ was chosen.

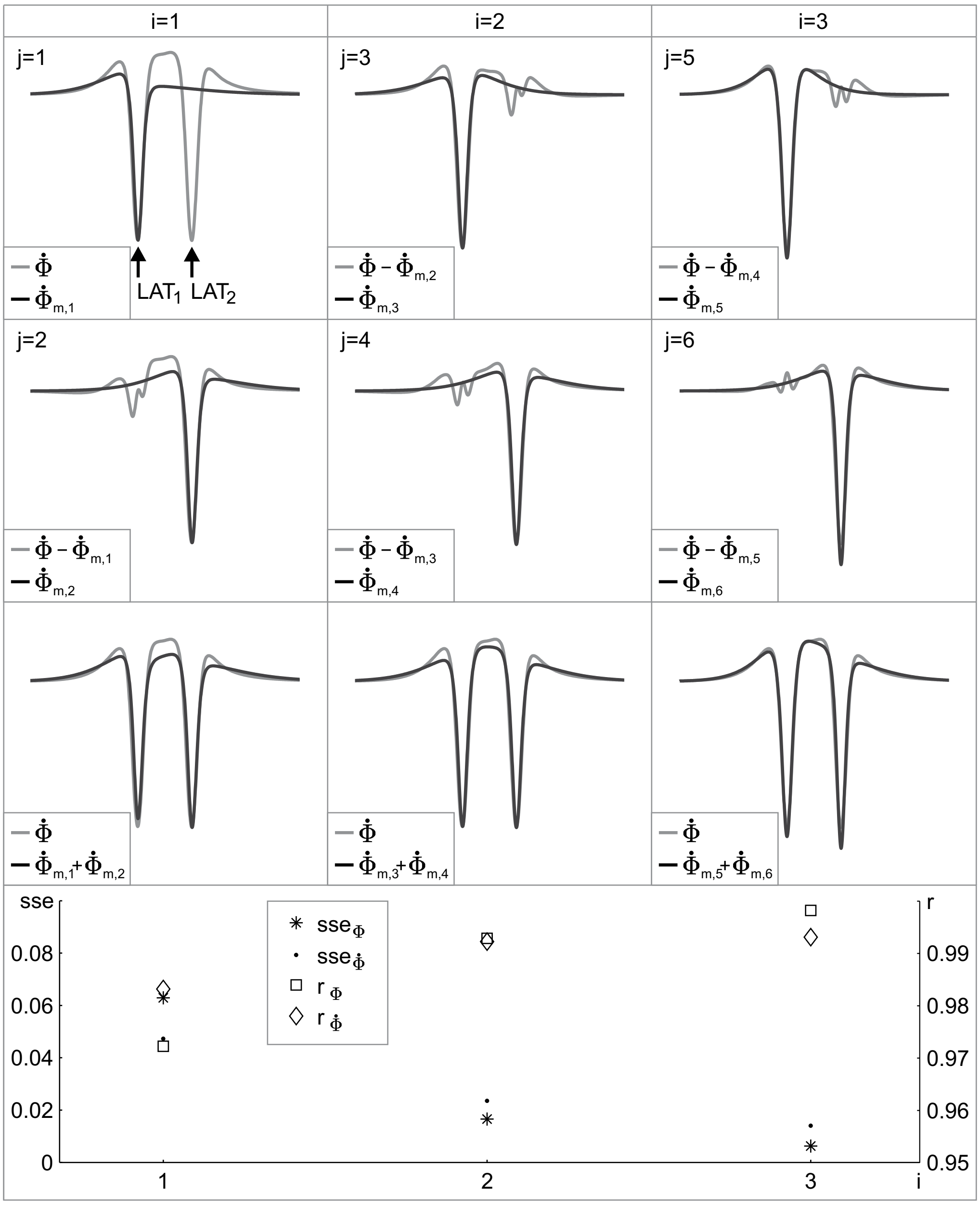

Figure 7.5: Decomposition of a fractionated waveform consisting of two components at the local activation times LAT_1 and LAT_2, respectively; number of iterations n=3: For better visibility, the graphs show the development of the temporal derivatives of simulated waveform $\dot{\Phi}$ and modeled waveform $\dot{\Phi}_m$. The decomposition starts by fitting in the signal model at LAT_1 (panel j=1). The modeled waveform $\Phi_{m,1}$ is subtracted from Φ and LAT_2 is adapted before curve fitting centered at LAT_2 is performed (j=2). The third row shows the result of the fitting procedure after each iteration i. The diagram below displays the changes in error (sse) and correlation coefficient r between the simulated waveform Φ and the modeled waveform Φ_m (sse_Φ and r_Φ), as well as between their derivatives $\dot{\Phi}$ and $\dot{\Phi}_m$ ($sse_{\dot{\Phi}}$ and $r_{\dot{\Phi}}$). Figure adopted from [128].

7.6.1 Evaluation of the Decomposition of Fractionated Electrograms

Two setups, depicted in Figure 7.6 were considered. The first setup consists of two 20 mm long strands of cardiomyocytes where the distance z between *strand 2* and recording site could be varied (Figure 7.6 (a)). The weighting of two propagating sources on the extracellular potential Φ at the recording position was separately analyzed by stimulating only either *strand 1* or *strand 2*. Φ was obtained by adding the contributions Φ_1 and Φ_2 of the two strands.

The second setup modeled a 2D-anisotropic sheet of tissue of 4 mm × 1.25 mm in which obstacles were embedded to mimic the effect of microfibrosis upon activation patterns at a microscopic size scale (Figure 7.6 (b)). Longitudinal to transversal conductivity ratio was set to 9.158; longitudinal conduction velocity was 0.7 m/s. Two rectangular nonconducting obstacles of $500\,\mu$m $\times$ $50\,\mu$m, oriented parallel to the fibers were embedded at a distance of $100\,\mu$m in the center of the tissue sheet, mimicking inlays of interstitial connective tissue. Point-like stimulation of 1 ms duration was applied to the lower left corner of the sheet to induce an elliptic wavefront which propagates towards the obstacles in an oblique direction. To mask the influence of borders, an area of 1 mm × 0.3 mm at the center of the sheet was extracted for signal analysis.

The setup consisting of two 1D-strands of cardiomyocytes was used to synthesize fractionated electrograms Φ_{12} in a well-controlled manner by superposition of two nonfractionated waveforms Φ_1 and Φ_2. Two limiting parameters for the decomposition of fractionated electrograms were taken into consideration: 1.) the difference ΔLAT between the local activation times of Φ_1 and Φ_2, and 2.) the difference in the distance between recording site and the sources of Φ_1 and Φ_2, respectively. The components Φ_1 and Φ_2 were recorded at site II, with only either *strand 1* or *strand 2* being stimulated. The minimum distance of $50\,\mu$m between recording site and strand corresponds to the distance between electrodes and tissue surface of the used CNF sensors [54]. Φ_2 was computed with *strand 2* being located at distances $z = 50 \ldots 300\,\mu$m in steps of $5\,\mu$m, which resulted in an amplitude ratio between Φ_2 and Φ_1, A_2/A_1, in the range of 1 to 0.24.

The depolarization time of Φ_1, t_{dep1} was 0.94 ms, whereas the depolarization time of Φ_2, t_{dep2} constantly increased from 0.94 to 1.8 ms with increasing z. The difference in LAT (ΔLAT) was varied by temporally shifting Φ_2 with respect to Φ_1 from 0.5 to 3 ms in steps of 0.1 ms. The resulting fractionated electrogram Φ_{12} was decomposed with the described procedure to recover the nonfractionated components Φ_{m1} and Φ_{m2} as well as their sum Φ_{m12}. To evaluate the goodness of fit, the amplitudes B_1 and B_2, the symmetry factors b_1 and b_2, and the depolarization times t_{depm1} and t_{depm2} of Φ_{m1} and Φ_{m2} were compared to the values A_1, A_2, a_1, a_2, t_{dep1}, and t_{dep2}, respectively, obtained from Φ_1 and Φ_2. For each distance z and each parameter (B_1, B_2, b_1, b_2, t_{depm1}, and t_{depm2}), the minimum values of ΔLAT were determined above which the chosen error tolerance of $\pm 20\%$ for amplitude

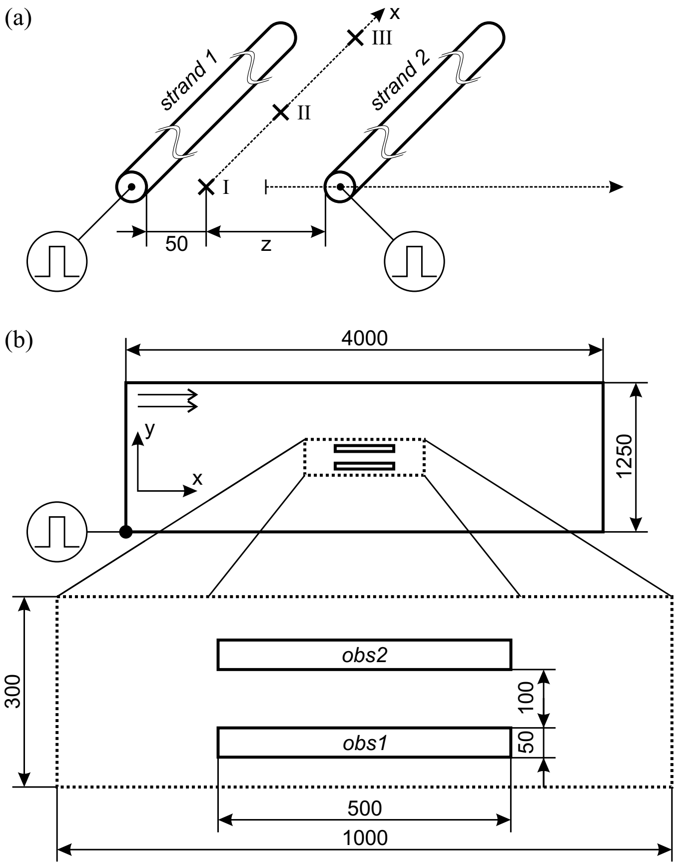

Figure 7.6: Computer simulation setups. *(a)* Two 20 mm long strands of cardiomyocytes stimulated at $x = 0\,\mathrm{mm}$. Recording positions (×) at the beginning (I, $x = 0\,\mathrm{mm}$), in the middle (II, $x = 10\,\mathrm{mm}$), and at the end of the strands (III, $x = 20\,\mathrm{mm}$) at a fixed distance of $50\,\mu\mathrm{m}$ from *strand 1* and a variable distance z from *strand 2*. *(b)* 2D-sheet of tissue with embedded obstacles *obs1* and *obs2*, stimulated at the lower left corner. Fiber orientation is aligned with the x-axis. The dashed area was considered for signal analysis. Dimensions are given in μm. Figure adopted from [128].

and depolarization time, and ±0.2 for the symmetry factor, were not exceeded.

To examine the robustness of the decomposition method against noise, for each z and ΔLAT Gaussian white noise with amplitudes according to experimental values (see Table 8.1) was regenerated 100 times and added to Φ_{12} before the decomposition procedure was performed. The mean values μ and standard deviations σ of B_1, B_2, b_1, b_2, t_{depm1}, and t_{depm2} were calculated and compared to the corresponding values A_1, A_2, a_1, a_2, t_{dep1}, and t_{dep2}. Again, the minimum values of ΔLAT were determined above which $\mu \pm \sigma$ did not exceed the chosen error tolerance. The respective values were denoted $\Delta\mathrm{LAT}_{min,B_1}$, $\Delta\mathrm{LAT}_{min,B_2}$, $\Delta\mathrm{LAT}_{min,b_1}$, $\Delta\mathrm{LAT}_{min,b_2}$, $\Delta\mathrm{LAT}_{min,t_{depm1}}$, and $\Delta\mathrm{LAT}_{min,t_{depm2}}$.

7.6.2 Application of the Decomposition Procedure to Fractionated Electrograms Caused by a Microstructural Obstacle

In order to obtain fractionated electrograms with a fractionation index $1 \leq \mathrm{FI} \leq 3$, the 2D-computer model of a tissue sheet with two embedded elongated microobstacles was used. This setup is depicted in Figure 7.6 (b). As demonstrated in Section 3.4.2, for the occurrence of fractionated electrograms not only the presence of conduction obstacles but also their orientation with respect to the direction of propagation is essential. That is, wavefronts propagating aligned with the axis of an elongated obstacle do not produce any relevant fractionation. Therefore, a stimulus site was chosen to induce propagation in an oblique direction relative to the alignment of the obstacle, to ensure sufficiently large delays in activation time between the split wavefronts. In a grid of 25 μm lateral length spanning an area of approximately 1 mm × 0.3 mm, 602 extracellular potentials $\Phi(t)$ were computed at a distance $z = 50\,\mu$m. The decomposition procedure was applied to the entire set of electrograms. FI, sse_{Φ}, $sse_{\dot{\Phi}}$, r_{Φ}, and $r_{\dot{\Phi}}$ were computed.

7.7 Discrimination of Local and Distant Activation

7.7.1 Computer Simulation Study

To investigate the influence of fiber thickness and direction of propagation with respect to the fiber orientation on two distance measures, the following two computer models were created.

3D-Fiber

Two myocardial muscle fibers with different diameters were modeled by a three-dimensional cubic monodomain model. The dimensions were 5 mm × 0.25 mm × 0.25 mm for the thin fiber (cable A) and 5 mm × 1 mm × 1 mm for the thick fiber (cable B). Membrane kinetics were represented by the Mahajan-Shiferaw model [11]. Propagation of activation was induced by an electrical stimulus at one fiber end.

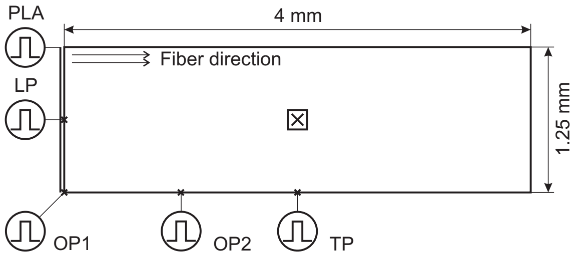

Figure 7.7: Computer simulation arrangement of a 2D-sheet of cardiac tissue. Stimulus positions to induce planar (PLA), longitudinal elliptic (LP), transversal elliptic (TP), and oblique elliptic (OP1 and OP2) wavefronts of activation. The point of observation for $\mathbf{\Phi}$, in the center of the sheet, is marked with ×.

Extracellular potentials $\mathbf{\Phi}$ were computed in the middle of the fibers at distances $z = 50 \ldots 500\,\mu$m from the surface in steps of $5\,\mu$m.

The amplitudes of Φ and its first and second temporal derivative (Φ_{pp}, $\dot{\Phi}_{pp}$, $\ddot{\Phi}_{pp}$) as well as the maxima of the magnitude of CNF strength ($|\boldsymbol{E}|_{pp}$) and its temporal derivative ($|\dot{\boldsymbol{E}}|_{pp}$) were computed.

2D-Sheet

The tissue model depicted in Figure 7.7 was used. Membrane kinetics were represented by the Mahajan-Shiferaw model [11]. Stimulus sites were chosen to induce planar (PLA) as well as elliptic wavefronts of activation propagating in longitudinal (LP), transversal (TP), and oblique (OP1 and OP2) directions.

Extracellular potentials $\mathbf{\Phi}$ were computed in the center of the tissue sheet at distances $z = 50 \ldots 500\,\mu$m from the surface in steps of $5\,\mu$m.

From $\mathbf{\Phi}$, Φ_{pp}, $\dot{\Phi}_{pp}$, $\ddot{\Phi}_{pp}$, $|\boldsymbol{E}|_{pp}$, and $|\dot{\boldsymbol{E}}|_{pp}$ were computed.

2D-Sheet with Branching

In the described tissue sheet, an electric isolator was embedded to mimic a branching structure. The asymmetric position of this obstacle within the tissue (see Figure 7.8) formed a thick branch with a diameter of $575\,\mu$m and a thin branch with a diameter of $250\,\mu$m. Stimulus positions were chosen to induce planar (PLA), longitudinal elliptic (LP), and oblique elliptic (OP) wavefronts of impulse propagation.

Extracellular potentials $\mathbf{\Phi}$ were computed in the center of the thin tissue branch (1), in the center of the obstacle between the branches (2), and in the center of the thick branch (3) at distances $z = 50$, 100, 200, 300, 400, and $500\,\mu$m from the surface.

The local conduction velocity (LCV) θ was calculated from $\boldsymbol{V}_m$ in Pos. 1 and 3 for stimulus sites PLA, LP, and OP. In order to vary the LCV, simulations were performed

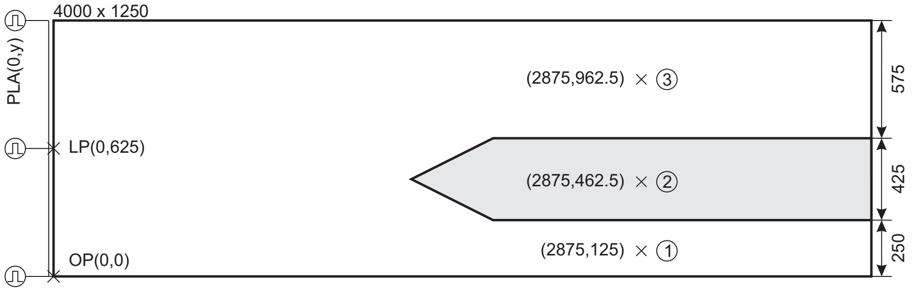

Figure 7.8: Computer simulation arrangement of a 2D-sheet of cardiac tissue with embedded obstacle. Stimulus positions to induce planar (PLA), longitudinal elliptic (LP), and oblique elliptic (OP) wavefronts of activation. At the points of observation 1, 2, and 3, $\mathbf{\Phi}$ is computed at 50, 100, 200, 300, 400, and 500 μm above the surface of the tissue. Dimensions are given in μm.

with the intracellular conductivity [3] g_I reduced by 50%. Unchanged g_I was denoted as $1\,g_I$, reduced g_I as $0.5\,g_I$.
Φ_{pp}, $\dot{\Phi}_{pp}$, $\ddot{\Phi}_{pp}$, $|\boldsymbol{E}|_{pp}$, and $|\dot{\boldsymbol{E}}|_{pp}$ were computed.
In case of oblique elliptic propagation (OP) of the activation wavefront, fractionated electrograms $\mathbf{\Phi}$ are observed in Pos. 2. This is, because the wavefront collides with the lower left side of the obstacle and then gets accelerated in front, and decelerated in moving around the obstacle. The fractionated $\mathbf{\Phi}$ were separated into the contributions from the thin and the thick tissue branch by windowing, and Φ_{pp}, $\dot{\Phi}_{pp}$, $\ddot{\Phi}_{pp}$, $|\boldsymbol{E}|_{pp}$, and $|\dot{\boldsymbol{E}}|_{pp}$ were computed for the individual contributions to $\mathbf{\Phi}$.

7.7.2 Experimental Study

Guinea pig papillary muscles were stimulated at a rate of 2/s with a current pulse of 1 ms duration and a magnitude of approximately 1.5 times the stimulation threshold. Figure 7.9 shows an image, taken during such an experiment.

The common sensor setup had to be modified in order to overcome two difficulties. First, the CNF sensor 1 was stiffened by applying a glue film onto its polyimide carrier. Hence the floating of the sensor due to streaming of the Tyrode's solution was reduced. Second, sensor 1 was positioned laterally to the papillary muscle in order to monitor its distance z from the surface of the muscle. Using a 3D-micromanipulator, z was varied from 50 μm, which corresponds to the height of the spacer pillars, to approximately 500 μm. The current position of the sensor was documented by a digital image taken with a single-lens reflex camera (see Section 4.1.3). The CNF sensor 2 was positioned close to sensor 1 at the

---

[3] The intracellular conductivity seen in the traditional bidomain and monodomain equations is an effective (or average) conductivity. It is obtained by considering the effect of gap junction resistance on propagation to be small enough that it may be ignored or at least averaged over the entire cell [61]. In this work, such conductivities are termed g_I.

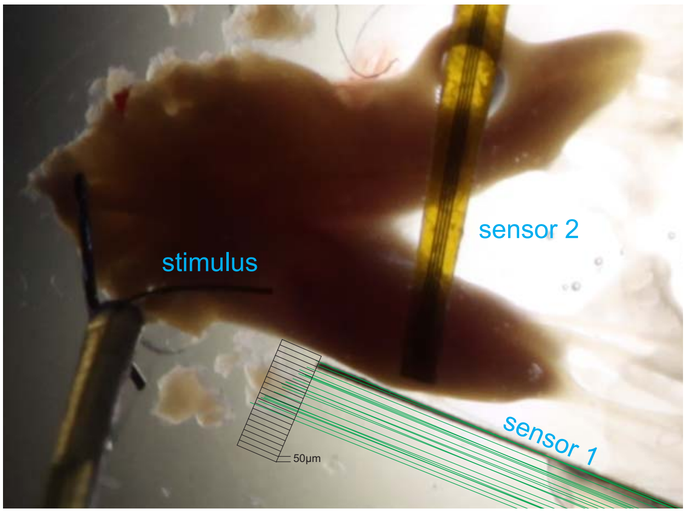

Figure 7.9: Measurement of $\mathbf{\Phi}$ at different distances z from the surface of a guinea pig papillary muscle. The green lines indicate different positions of sensor 1. z was recovered after the experiment from digital images. Sensor 2 was kept at the same position throughout the experiment.

surface of the muscle to monitor the stability of the activation during the entire recording process.

A single cycle of $\mathbf{\Phi}$ was recorded from sensor 1 at every position. After the experiment the actual distances z between sensor and surface of the tissue were recovered by means of the digital images. $|\boldsymbol{E}|_{pp}$, $|\dot{\boldsymbol{E}}|_{pp}$, $|\dot{\Phi}|_{pp}$, and $|\ddot{\Phi}|_{pp}$ were calculated.

7.8 Classification of Tissue Microstructure through CNF Signals

7.8.1 Computer Model

From the computer model of a rabbit atrium (see Section 4.2.2), 6 sections (1 mm × 1 mm) were extracted and classified by an expert into

1) WC: well coupled tissue (number of sections n=2),

2) PO: tissue with separating structures which are in parallel to the fiber direction (n=2), or

3) CO: tissue with complex pattern of separating structures (n=2).

Figure 7.10 shows a sample of each tissue class.

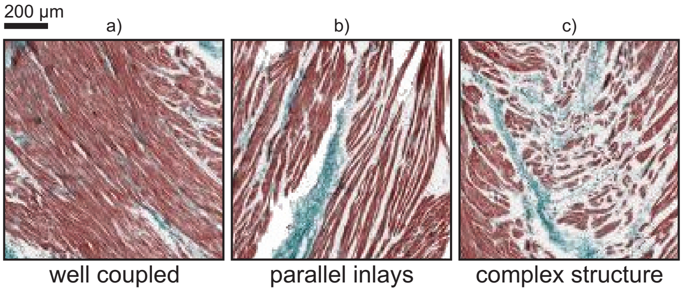

Figure 7.10: Samples of tissue sections (1 mm × 1 mm) representing three tissue classes. *a)* WC: Well coupled tissue. *b)* PO: Tissue containing parallel inlays of connective tissue. *c)* CO: Tissue with complex arrangement of microstructural obstacles for propagation of activation. Myocytes are stained in red, connective tissue in blue, and interstitial clefts in white.

7.8.2 Stimulation and Recording

The arrangement is illustrated in Figure 7.11. Twelve stimulus sites (STIM 1 . . . 12) were equally distributed on an imaginary ring around the tissue section under examination. The number of stimulus sites M was then varied ($M = 12$, 6, and 3).
Extracellular electrograms were computed 50 μm above the surface of the tissue. The grid length d was varied ($d = 100$, 200, 300, 400, and 600 μm) yielding 121, 36, 15, 9, and 4 simultaneously recorded electrograms, respectively.

7.8.3 Feature Extraction

For each stimulus site, the fractionation index (FI) was calculated for the entire set of electrograms using the algorithm *SM* described in Section 7.5.2. Moreover, the amplitude Φ_{pp} of each electrogram was computed. The means of FI (μ_{FI}) and Φ_{pp} (μ_{amp}) were determined for each stimulus site.

From FI and Φ_{pp}, the following three features were selected for the classification process.

1) m_{FI}: mean of μ_{FI} over all stimulus sites.

2) ΔFI: range of μ_{FI} ($\Delta FI = \max_{M} \mu_{FI} - \min_{M} \mu_{FI}$).

3) ξ_{amp}: normalized range of μ_{amp}. $\xi_{amp} = \Delta amp/m_{amp}$, where $\Delta amp = \max_{M} \mu_{amp} - \min_{M} \mu_{amp}$ and m_{amp} is the mean of μ_{amp} over all stimulus sites.

In case the number of stimulus sites $M = 6$, the features were computed for stimulus positions 1, 3, 5, 7, 9, and 11. Then, the imaginary ring containing the stimulus electrodes was rotated by 30° and the features were again computed. Thus, e.g. for $M = 3$, three feature sets were obtained. In the same manner, for $d = 200\,\mu$m the grid of recording

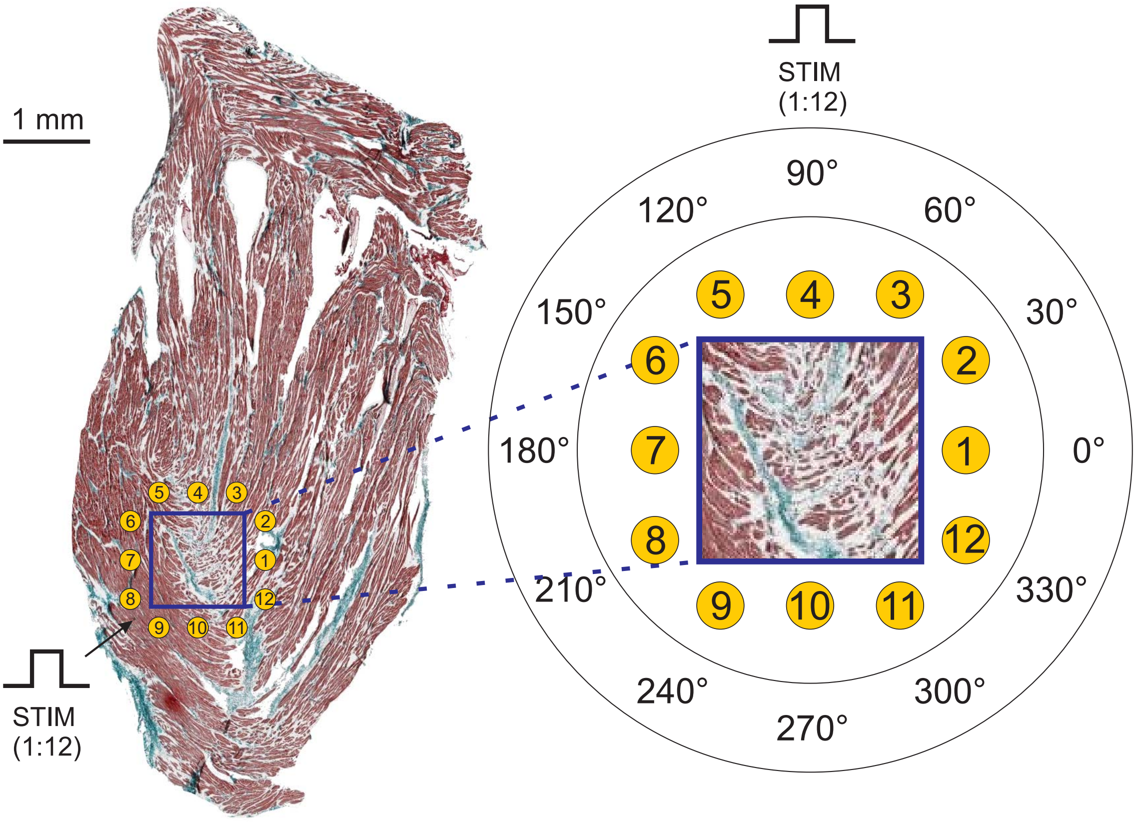

Figure 7.11: Principle of the circumferential stimulation. Twelve stimulus electrodes are arranged on an imaginary ring surrounding the tissue section under inspection. Image was provided by F. Campos (Medical University of Graz, Institute of Biophysics, 2011).

points was shifted in x and y direction by $[x\ y]^T = [100\ 0]\,\mu$m, $[x\ y]^T = [0\ 100]\,\mu$m, and $[x\ y]^T = [100\ 100]\,\mu$m. Thus, e.g. for $d = 200\,\mu$m, four feature sets were obtained. The obtained sample sizes for varying M and d are listed in Tables 8.10-8.12.

7.8.4 Classification

A linear discriminant analysis (LDA) classifier [130] was used to classify a tissue section into one of three classes based on the three features extracted from the electrograms. Cross validation was done using the leave-one-out method [131]. Evaluation criterion was the classification accuracy [132] for each class (acc_1 for WC, acc_2 for PO, and acc_3 for CO) as well as the overall accuracy acc_{tot}.

Chapter 8

Results

In this Chapter, the results of theoretical analyses, computer simulation studies, and electrophysiological experiments described in the previous Chapters 6 and 7 are presented. Page numbers of the corresponding Sections in Chapter 7 are given in footnotes.

8.1 Signal and Noise Analysis of CNF Signals

8.1.1 Statistical Analysis of CNF Signal Parameters [1]

Figure 8.1 displays box plots of parameters FI, Φ_{pp}, $\dot{\Phi}_{pp}$, ANR, and $|\boldsymbol{E}|_p$ determined from signals of *set A*. Figure 8.2 compares box plots from Φ_{pp}, $\dot{\Phi}_{pp}$, ANR, and $|\boldsymbol{E}|_p$ determined from nonfractionated signals (*set I*) and fractionated signals (*set II*).

The medians of all displayed parameters are significantly higher in *set I* than in *set II* (*Mann-Whitney-U test*, $p < 0.05$). In addition, the quartiles of the distribution of the ANR are listed in Table 8.1.

---

[1] Methods, see p.55.

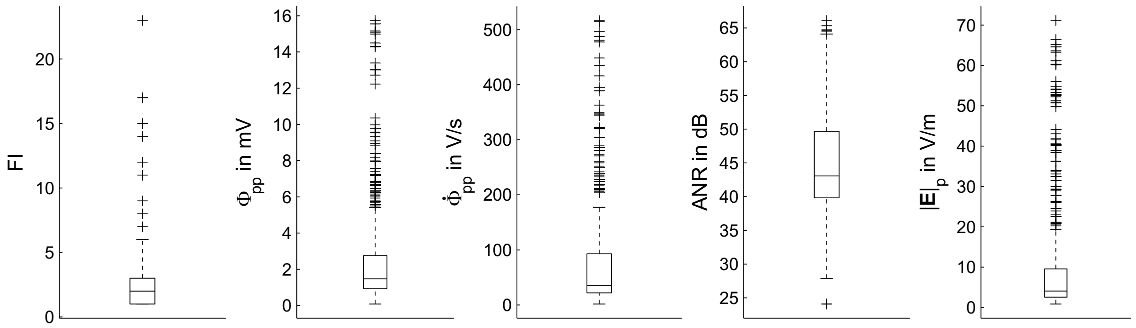

Figure 8.1: Box plots of parameters FI, Φ_{pp}, $\dot{\Phi}_{pp}$, ANR, and $|\boldsymbol{E}|_p$ determined from *set A* (n = 566).

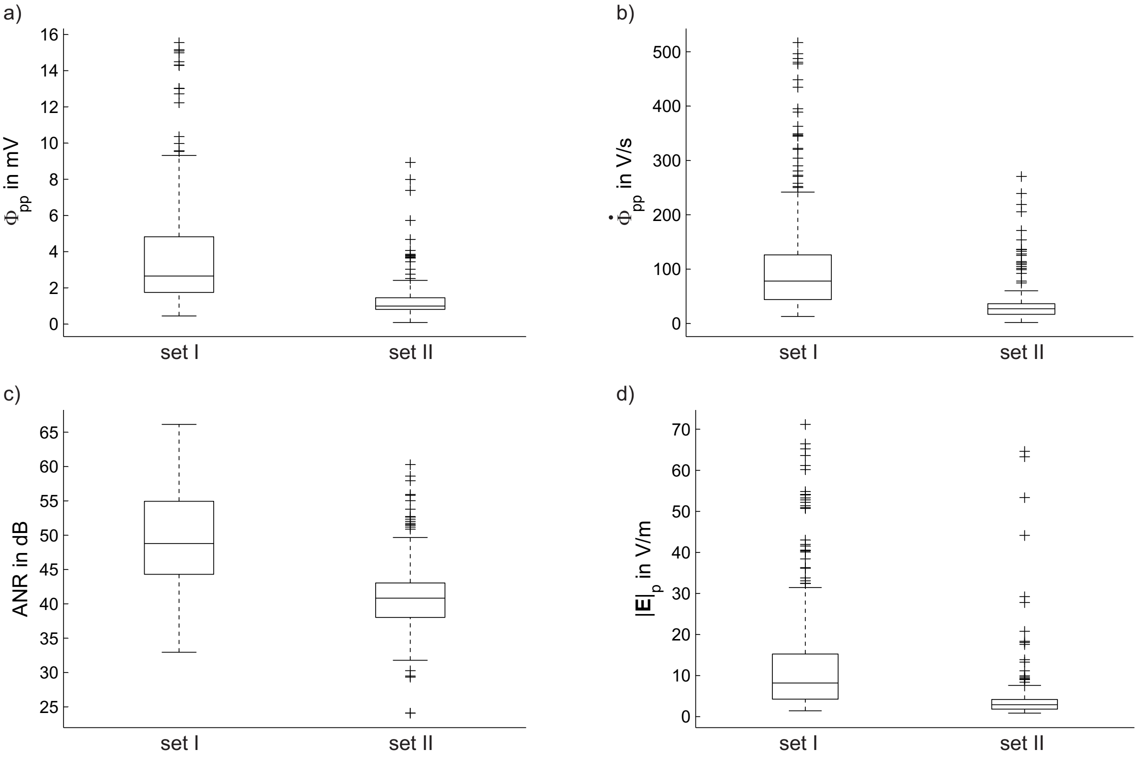

Figure 8.2: Box plots of parameters determined from *set I* (n = 200) and *set II* (n = 200). *a)* Φ_{pp}, *b)* $\dot{\Phi}_{pp}$, *c)* ANR, and *d)* $|\boldsymbol{E}|_p$.

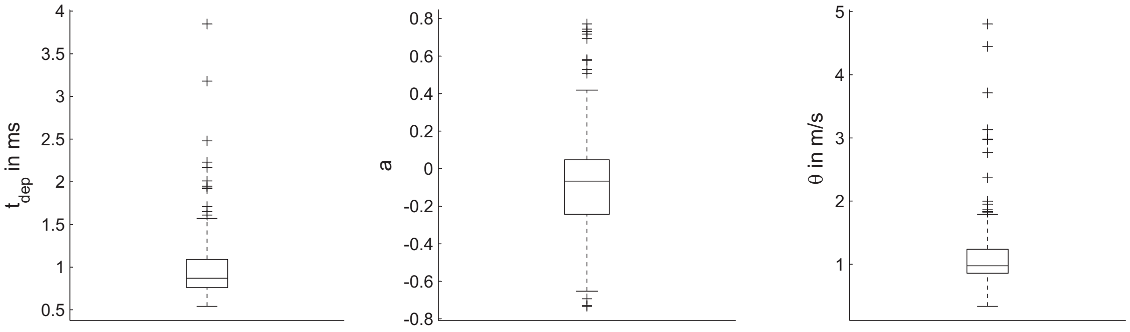

Figure 8.3: Box plots of parameters t_{dep}, a, and θ determined from *set I* (n = 200).

Set	A	I	II
n	566	200	200
$\text{ANR}_{.25}$ in dB	39.83	44.30	38.00
$\text{ANR}_{.50}$ in dB	43.07	48.97	40.97
$\text{ANR}_{.75}$ in dB	49.68	55.08	43.25

Table 8.1: Lower quartile ($\text{ANR}_{.25}$), median ($\text{ANR}_{.50}$), and upper quartile ($\text{ANR}_{.75}$) of the amplitude-to-noise ratio in dB of *set A*, *set I*, and *set II*.

	FI	Φ_{pp}	$\dot{\Phi}_{pp}$	ANR
Φ_{pp}	-0.340			
$\dot{\Phi}_{pp}$	-0.322	0.977		
ANR	-0.512	0.863	0.857	
$\lvert\boldsymbol{E}\rvert_p$	-0.272	0.903	0.898	0.788

Table 8.2: Cross correlation coefficients between parameters from *set A* (n = 566).

In Table 8.2 the Pearson product-moment cross correlation coefficients r of the determined parameters from *set A* are displayed. It can be seen that there is a very high correlation ($r_{\Phi_{pp}\dot{\Phi}_{pp}} = 0.977$) between Φ_{pp} and $\dot{\Phi}_{pp}$. Moreover, strong correlations are given between $\lvert\boldsymbol{E}\rvert_p$ and the parameters Φ_{pp} ($r_{\lvert\boldsymbol{E}\rvert_p\Phi_{pp}} = 0.898$) and $\dot{\Phi}_{pp}$ ($r_{\lvert\boldsymbol{E}\rvert_p\dot{\Phi}_{pp}} = 0.903$).

The duration of depolarization t_{dep}, symmetry a, and magnitude of local conduction velocity θ were evaluated only for *set I*, because these parameters might show ambiguous results in case of fractionated electrograms. Box plots from these values are presented in Figure 8.3.

8.1.2 Analysis of Noise in the Measurement Chain [2]

Power spectral densities (PSD's) of the quantization noise, the amplifier noise, and the noise of the entire measurement chain are depicted in Figure 8.4 d). The latter is significantly higher than the PSD of the amplifier noise.

The comparison of noise power of individual channels and difference signals between channels has shown no significant differences.

In histogram plots, the amplitude distribution of the noise signal of the measurement chain resembles a normal distribution. However, a normal probability plot and a logarithmic plot of the probability distribution [133] (not shown) have revealed slight deviations from a normal distribution in the tails of the function.

The maximum amplitude of the power line interference in four recording channels was $A_{\tilde{\Phi}} = 49.6\,\mu V$.

8.1.3 Frequency Analysis of CNF Signals [3]

Figure 8.4 a) shows $\Phi_{sim}(t)$ computed at distances $z = 1\,\mu m$ and $z = 50\,\mu m$ from the surface of the tissue. The temporal resolution was $10\,\mu s$ which corresponds to the sampling rate of 100 kHz used for the acquisition of CNF signals with HARMS. The PSD's of Φ_{sim}, computed at distances $z = 1\,\mu m$ and $z = 50\,\mu m$ from the surface of the tissue are given in

---

[2] Methods, see p.56.

[3] Methods, see p.56.

Figure 8.4 b). For the purpose of comparison, the PSD of an experimental waveform Φ_{exp} is plotted in Figure 8.4 d). It can be seen that the relevant frequency components from Φ_{sim} recorded at $z = 1\,\mu$m range from $f = 0 \cdots \approx 7\,$kHz. For Φ_{sim} recorded at $z = 50\,\mu$m as well as for Φ_{exp}, the bandwidth is even smaller with an upper limit $f \approx 6\,$kHz.

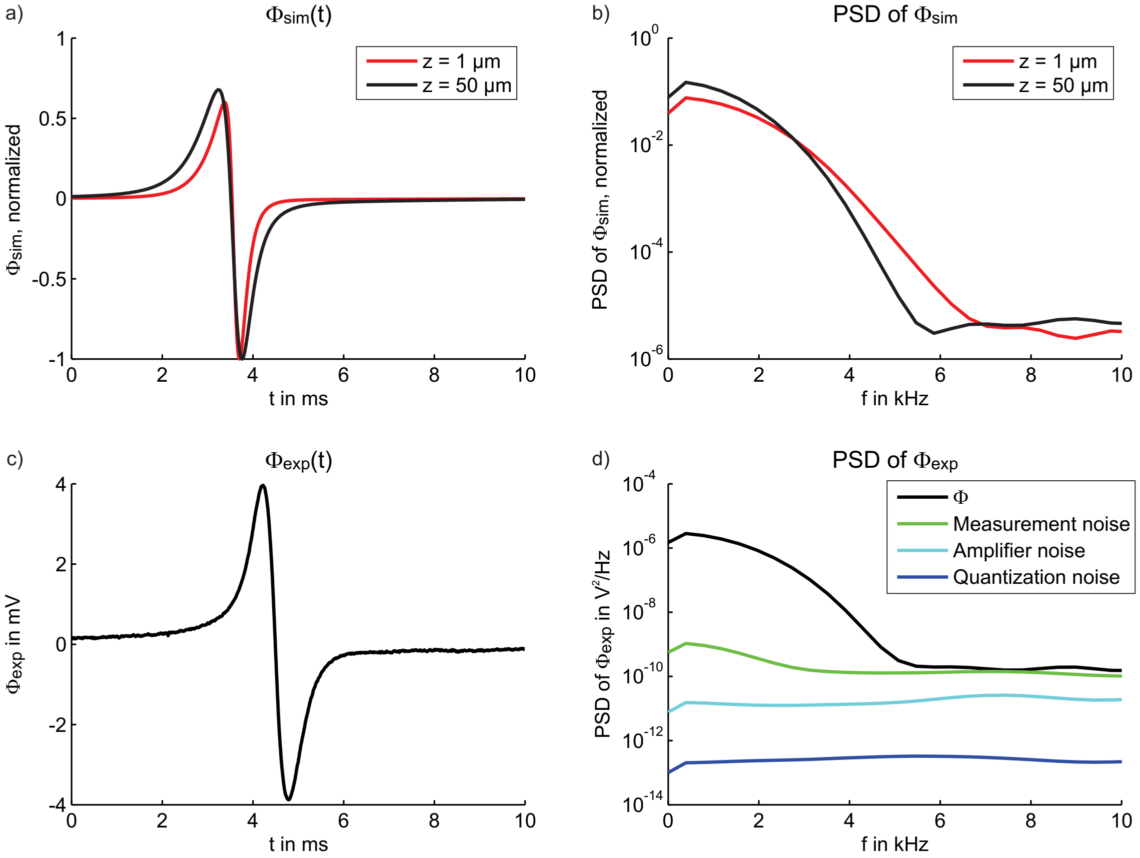

Figure 8.4: Frequency response of CNF and noise signals from computer simulation and experiment. *a)* Electrograms from computer simulation computed at distances $z = 1\,\mu$m and $z = 50\,\mu$m above the surface of the tissue, normalized. *b)* Corresponding power spectral densities (PSD's). *c)* Electrogram recorded during electrophysiological experiment. *d)* Corresponding PSD (black curve) as well as PSD's of the noise of the entire measurement chain (green), the noise of the amplifier circuit (cyan), and the quantization noise introduced by the 16 bit ADC (blue). For better visibility, frequency axes are displayed in the range of 0 to $f_S/10$, where $f_S = 100\,$kHz.

8.2 Determination of Local Conduction Velocity

8.2.1 Uncertainty Due to Temporal Discretization [4]

Figure 8.5 shows the uncertainty range in θ and φ as functions of θ for spatial and temporal resolution according to the experimental setup as well as for a temporal resolution increased by a factor of 20.

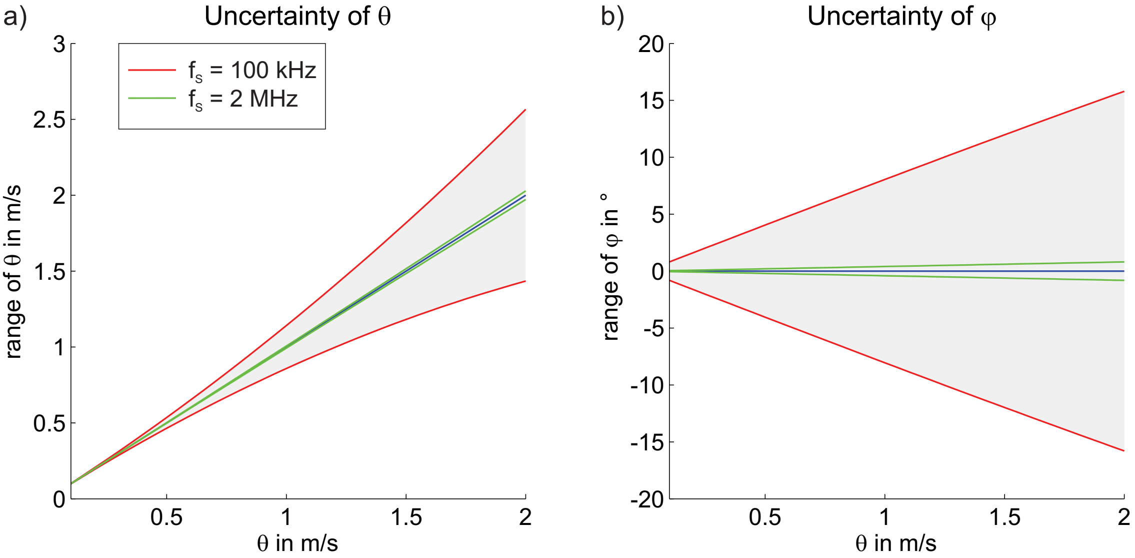

Figure 8.5: *a)* Uncertainty of θ as function of θ. *b)* Uncertainty of φ as function of θ. The uncertainty ranges are demarcated with red lines for sampling rate $f_S = 100\,\text{kHz}$ and green lines for $f_S = 2\,\text{MHz}$. The inter-electrode distance $\text{DD} = 71\,\mu\text{m}$.

Digital Resampling [5]

The range of $\text{LAT}_{2_i} - \text{LAT}_{1_i}$ did not exceed the uncertainty of $\pm 1\,\mu$s due to the temporal resolution of Φ_{h1} and Φ_{h2}. Hence, it was demonstrated that the achieved reductions in uncertainty of θ and φ by means of sinc-interpolation are in accordance with the results of the theoretical analysis shown in Figure 8.5.

8.2.2 Uncertainty Due to Noise [6]

Tables 8.3-8.6 list the minimum ANR (ANR_{min}) for which θ and φ ($\mu \pm 3\,\sigma$) remain within the given tolerance band for simulation setups a), b1), b2), and b3). Figures 8.6 and 8.7 show the dispersion of θ and φ as functions of ANR, respectively, for the simulation setup b3). θ was calculated with *CCF* and *dmin* methods, φ was calculated with *CCF*, *dmin*, and *Emag* methods.

---

[4] Methods, see p.57.

[5] Methods, see p.58.

[6] Methods, see p.58.

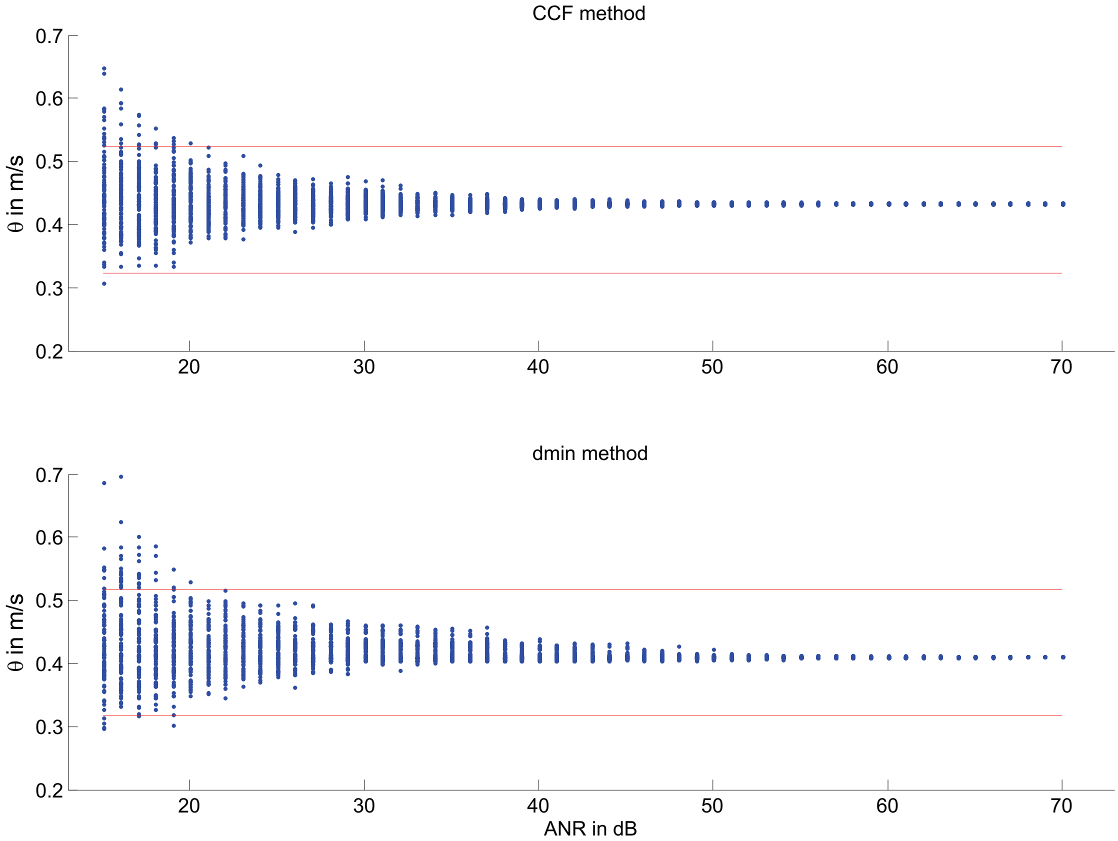

Figure 8.6: Dispersion of the magnitude θ of local conduction velocity resulting from 100 runs with regenerated noise for varying ANR. Oblique elliptic propagation, $\theta = 0.42\,\mathrm{m/s}$, $\varphi = 235°$, was simulated. θ was calculated using *CCF* and *dmin* methods. Red horizontal lines indicate the chosen tolerance limits for θ ($\pm 0.1\,\mathrm{m/s}$).

Table 8.3: ANR$_{min}$ for different methods of LCV determination and cutoff frequencies f_C of lowpass filter. a) Cable-like fiber $\theta = 0.5\,\mathrm{m/s}$, $\varphi = 180°$. Bold numbers indicate the minimum ANR$_{min}$ for the respective method.

	f_C in kHz	-	5	4	3	2.5	2	1.5	1	0.5	0.2
θ	CCF	61	34	31	28	26	25	25	**23**	**23**	36
	dmin	70+	56	53	47	42	37	34	27	**23**	26
φ	CCF	55	31	28	24	22	20	18	18	**16**	21
	dmin	70+	51	46	40	37	33	26	21	**17**	20
	Emag	32	22	21	20	19	**18**	19	23	21	34

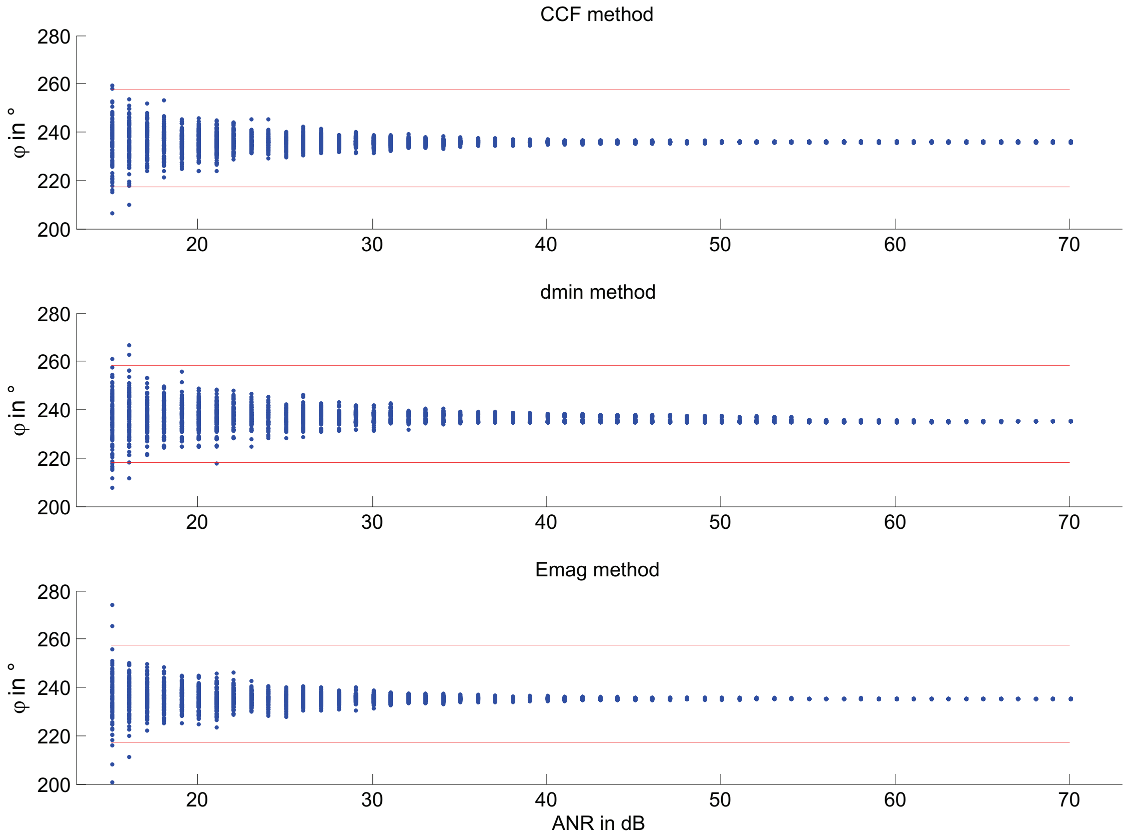

Figure 8.7: Dispersion of the direction φ of local conduction velocity resulting from 100 runs with regenerated noise for varying ANR. Oblique elliptic propagation, $\theta = 0.42\,\mathrm{m/s}$, $\varphi = 235°$, was simulated. φ was calculated by *CCF*, *dmin*, and *Emag* methods. Red horizontal lines indicate the chosen tolerance limits for φ ($\pm 20°$).

Table 8.4: ANR$_{min}$ for different methods of LCV determination and cutoff frequencies f_C of lowpass filter. b1) Rectangular tissue sheet, longitudinal propagation $\theta = 0.7\,\mathrm{m/s}$, $\varphi = 175°$. Bold numbers indicate the minimum ANR$_{min}$ for the respective method.

	f_C in kHz	-	5	4	3	2.5	2	1.5	1	0.5	0.2
θ	CCF	55	28	26	25	26	**24**	**24**	**24**	29	54
	dmin	70+	38	33	30	28	27	**26**	28	33	50
φ	CCF	45	21	20	17	17	17	**16**	17	20	44
	dmin	64	30	25	21	19	18	**17**	**17**	19	37
	Emag	27	17	17	**15**	16	16	18	20	28	46

Table 8.5: ANR_{min} for different methods of LCV determination and cutoff frequencies f_C of lowpass filter. b2) Transversal propagation $\theta = 0.28\,\mathrm{m/s}$, $\varphi = 267°$. Bold numbers indicate the minimum ANR_{min} for the respective method.

	f_C in kHz	-	5	4	3	2.5	2	1.5	1	0.5	0.2
θ	CCF	67	40	39	34	31	30	**29**	42	38	70+
	dmin	70+	51	46	40	38	33	31	**25**	27	42
φ	CCF	60	37	35	32	30	28	**25**	26	31	70+
	dmin	70+	48	44	38	35	31	28	**24**	27	50
	Emag	37	27	25	25	24	**23**	24	24	28	40

Table 8.6: ANR_{min} for different methods of LCV determination and cutoff frequencies f_C of lowpass filter. b3) Oblique propagation $\theta = 0.42\,\mathrm{m/s}$, $\varphi = 237.8°$. Bold numbers indicate the minimum ANR_{min} for the respective method.

	f_C in kHz	-	5	4	3	2.5	2	1.5	1	0.5	0.2
θ	CCF	53	28	25	23	24	**22**	**22**	24	31	52
	dmin	70+	40	34	30	28	25	**23**	**23**	30	61
φ	CCF	47	25	23	20	20	20	**18**	19	23	47
	dmin	67	35	31	27	25	22	**19**	**19**	21	42
	Emag	30	21	19	18	**17**	18	18	20	28	45

In case of longitudinal propagation (b1), the conduction velocity and thus the amplitude of Φ is higher than in case of transversal (b2) or oblique (b3) propagation. Assuming a certain noise level in the experimental environment which is independent of the type of propagation, the values for ANR in case of transversal or oblique propagation refer to the noise level at the respective ANR in case of longitudinal propagation.
The *Emag* method to compute φ is less sensitive to noise because it does not require the temporal differentiation of Φ.
The results shown in Tables 8.3-8.6 suggest to use a filter cutoff frequency $f_C = 1.5\,\mathrm{kHz}$ for *CCF* and *dmin* methods and $f_C = 2.5\,\mathrm{kHz}$ for the *Emag* method.

Figures 8.8 and 8.9 show the uncertainty of θ ($3\sigma_\theta$) and the uncertainty of φ ($3\sigma_\varphi$) as functions of θ and ANR. The values of $3\sigma_\theta$ and $3\sigma_\varphi$ are clipped at $0.1\,\mathrm{m/s}$ and $20°$, the chosen tolerance bands for θ and φ, respectively. A wider range of pairs of (φ, ANR) lies within the chosen tolerance band of φ than pairs of (θ, ANR) within the tolerance band of θ.

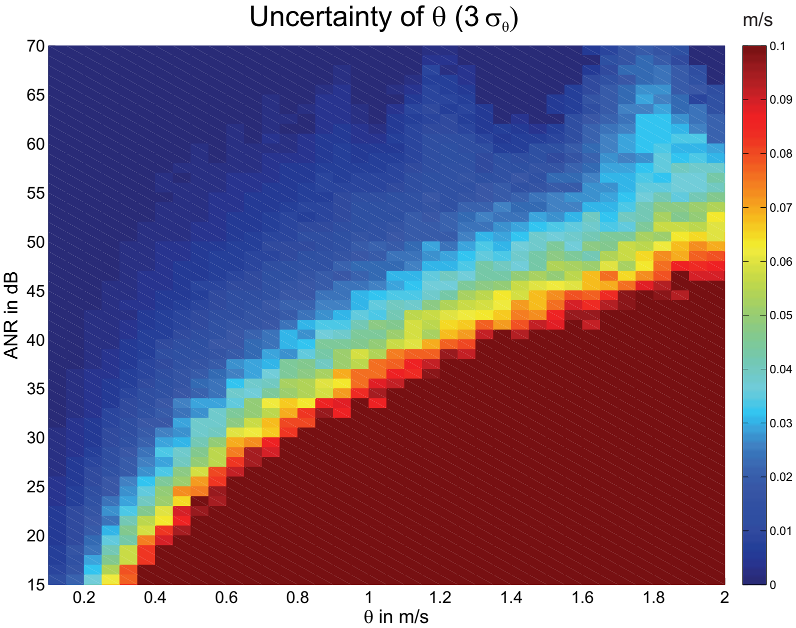

Figure 8.8: Uncertainty of the magnitude θ of local conduction velocity. $3\,\sigma_\theta$ as a function of θ and ANR. Values of $3\,\sigma_\theta$ were clipped at 0.1 m/s.

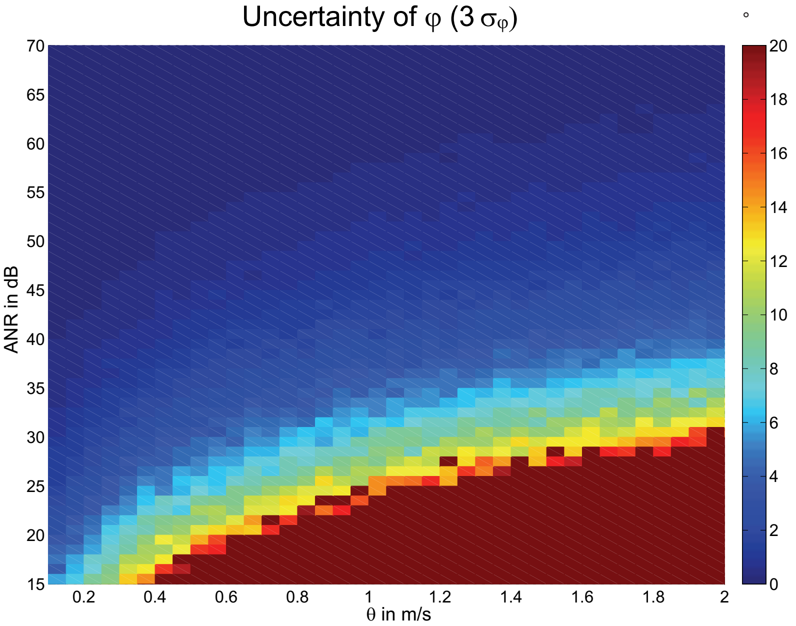

Figure 8.9: Uncertainty of the angle φ of local conduction velocity. $3\,\sigma_\varphi$ as a function of θ and ANR. Values of $3\,\sigma_\varphi$ were clipped at 20°.

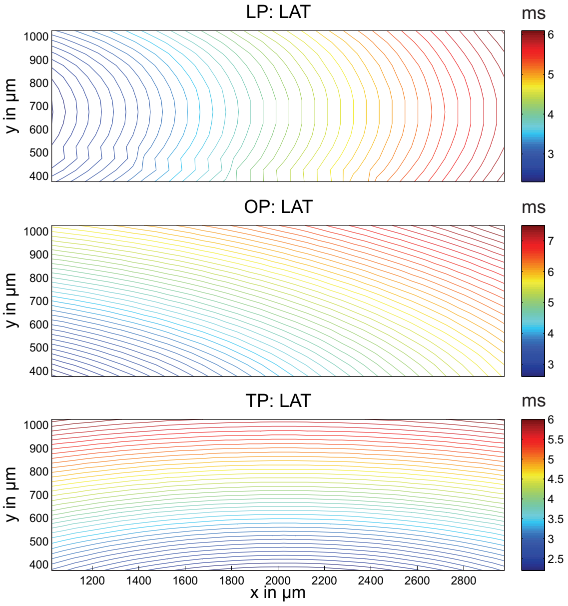

Figure 8.10: Isochrones of local activation time (LAT) for longitudinal (LP), oblique (OP), and transversal propagation (TP). The isochrone intervals are 100 μs.

8.2.3 Comparison to LCV Determined from Transmembrane Voltages [7]

Isochrones of LAT for longitudinal (LP), oblique (OP), and transversal impulse propagation (TP) are given in Figure 8.10.

Figure 8.11 shows LCV determined from $\boldsymbol{V_m}$ (θ_{Vm}, φ_{Vm}) and deviation in LCV determined from $\boldsymbol{\Phi}$ (e_θ, e_φ) for longitudinal (LP), oblique (OP), and transversal propagation (TP).
The highest deviations in θ and φ occur during LP, most notably in regions with a high curvature of the activation wavefront.

Figure 8.12 depicts LCV determined from $\boldsymbol{V_m}$ (θ_{Vm}, φ_{Vm}) and deviation in LCV determined from $\boldsymbol{\Phi}$ (e_θ, e_φ) for a tissue sheet with embedded obstacle during OP.
Close to the obstacle, the propagation is characterized by increased θ and changed φ, i.e. the activation wavefront changes its direction. e_θ and e_φ show high values up to a distance of about 500 μm from the obstacle.

8.3 Analytic Signal Model of Extracellular Electrogram [8]

Figure 8.13 depicts the simulated waveforms Φ using the LMCG model, the waveforms Φ_m modeled with the introduced signal model, and the residuals $e_\Phi = \Phi_m - \Phi$ at the

---

[7] Methods, see p.60.

[8] Methods, see p.60.

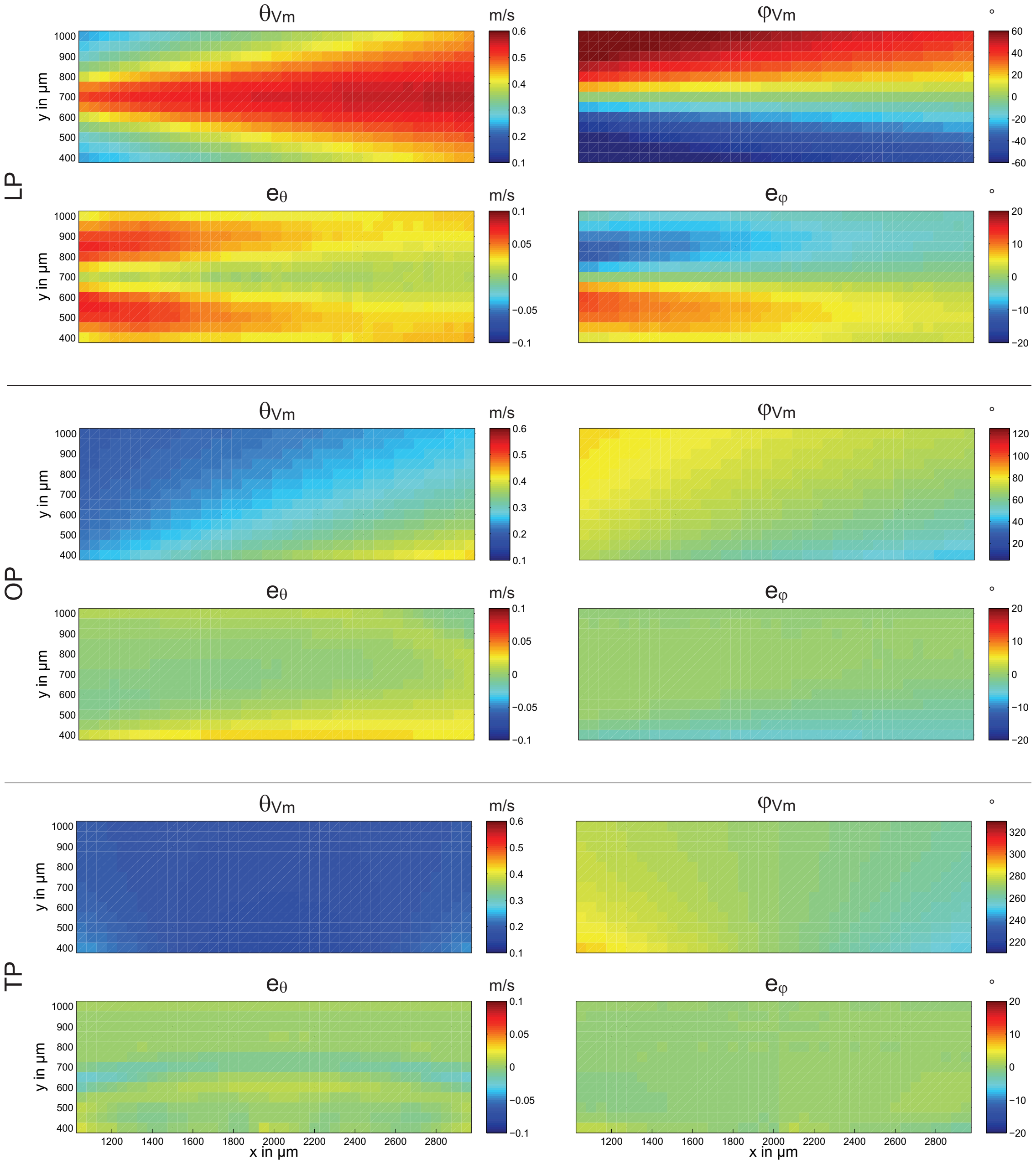

Figure 8.11: Comparison of LCV (magnitude θ and direction φ) computed from transmembrane voltages $\boldsymbol{V}_m$ and from extracellular electrograms $\boldsymbol{\Phi}$. LCV determined from $\boldsymbol{V}_m$ (θ_{Vm}, φ_{Vm}) and deviation in LCV determined from $\boldsymbol{\Phi}$ (e_θ, e_φ) for longitudinal (LP), oblique (OP), and transversal propagation (TP).

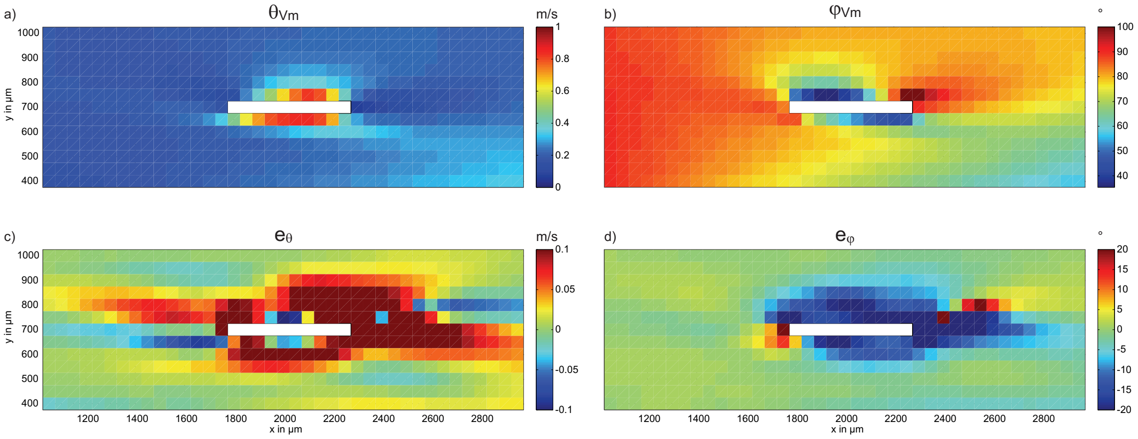

Figure 8.12: Comparison of LCV (magnitude θ and direction φ) computed from transmembrane voltages $\boldsymbol{V}_m$ and from extracellular electrograms $\boldsymbol{\Phi}$ in the vicinity of a microstructural obstacle, indicated by a white rectangle. Oblique elliptic propagation of activation was induced. *a)* Magnitude of LCV θ determined from $\boldsymbol{V}_m$. *b)* Angle of LCV φ determined from $\boldsymbol{V}_m$. *c)* Deviation in θ determined from $\boldsymbol{\Phi}$ (e_θ). *d)* Deviation in φ determined from $\boldsymbol{\Phi}$ (e_φ). Values of e_θ and e_φ were clipped at $e_\theta = \pm 0.1\,\mathrm{m/s}$ and $e_\varphi = \pm 20°$.

Table 8.7: Goodness of fit sse_Φ, r_Φ for Φ obtained from computer simulations using LMCG and MSH kinetic models.

	z(μm)	$x = 0\,\mathrm{mm}$	$x = 10\,\mathrm{mm}$	$x = 20\,\mathrm{mm}$
LMCG	5	0.041, 0.98	0.009, 1	0.009, 0.997
	250	0.111, 0.944	0.009, 1	0.006, 1
	500	0.197, 0.904	0.011, 1	0.008, 0.998
MSH	5	0.025, 0.987	0.008, 0.999	0.075, 0.998
	250	0.032, 0.984	0.018, 1	0.069, 0.988
	500	0.022, 0.99	0.018, 1	0.061, 0.97

beginning, in the middle, and at the end of the fiber in three different distances from the surface. Tables 8.7 and 8.8 list sse_Φ and r_Φ as well as $sse_{\dot{\Phi}}$ and $r_{\dot{\Phi}}$ for electrograms from the LMCG and the MSH model, respectively. The window for the evaluation of sse and r was chosen $3\,t_{dep}$ centered at the LAT.

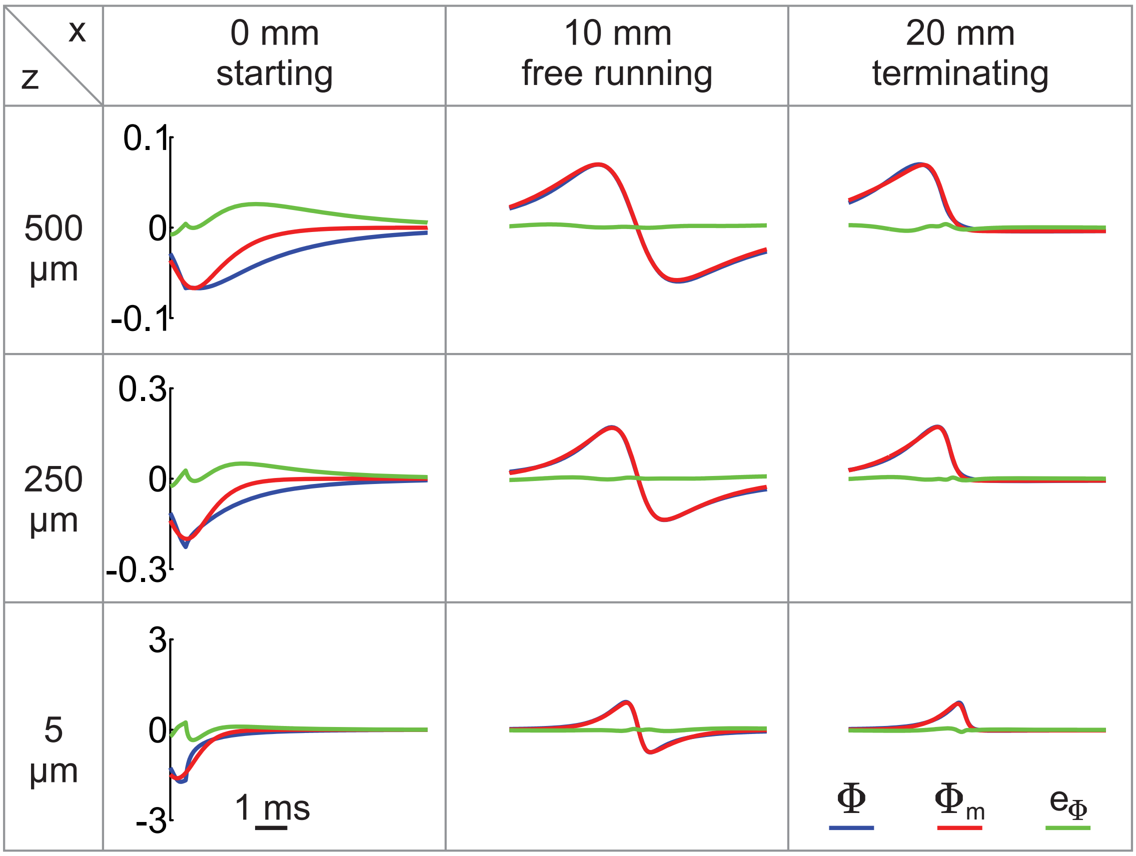

Figure 8.13: Modeling of nonfractionated depolarization waveforms: Simulated waveforms Φ (blue line), modeled waveforms Φ_m (red), and residuals e_Φ (green) at start (recording position I: $x = 0\,\mathrm{mm}$), middle (II: $x = 10\,\mathrm{mm}$), and end of the fiber (III: $x = 20\,\mathrm{mm}$) at distances $z = 5$, 250, and $500\,\mu\mathrm{m}$ from its surface. The amplitude scales are arbitrary and different for different z. Figure adopted from [128].

Table 8.8: Goodness of fit $sse_{\dot{\Phi}}$, $r_{\dot{\Phi}}$ for Φ obtained from computer simulations using LMCG and MSH kinetic models.

	z(μm)	$x = 0\,\mathrm{mm}$	$x = 10\,\mathrm{mm}$	$x = 20\,\mathrm{mm}$
LMCG	5	0.587, 0.651	0.006, 0.997	0.031, 0.986
	250	0.367, 0.795	0.003, 0.999	0.015, 0.993
	500	0.281, 0.85	0.003, 0.999	0.031, 0.984
MSH	5	0.449, 0.742	0.019, 0.991	0.025, 0.997
	250	0.334, 0.82	0.006, 0.998	0.07, 0.963
	500	0.231, 0.889	0.008, 0.997	0.179, 0.9

8.4 Analysis of Vector Loops of CNF Strength

8.4.1 Influence of Unequal Distances between Electrodes and Tissue [9]

Figure 8.14 displays the influence of altered distance (distance deviation Δz) from the tissue surface of one or two electrodes of a CNF sensor on the computed local direction of impulse propagation. The direction was determined on one hand from the CNF strength (φ_E) and on the other hand from the vector of local conduction velocity (φ). The respective deviations from φ_0, the angle determined in the absence of a Δz, (eφ_E and eφ) are shown for different values of Δz. Negative values of Δz indicate simulated breakage of the spacer pillars which maintain the distance z = 50 μm between electrodes and surface of the tissue. The deviation eφ_E increases with increasing Δz. The impact on LAT's and thus on LCV determination is negligible (see right diagrams in Figure 8.14).

The shape of the vector loop of $\boldsymbol{E}$ is impaired by unequal electrode-tissue distances in the way that its opening changes. Figure 8.15 gives an example of the changes in shape of the vector loop of $\boldsymbol{E}$ for longitudinal elliptic propagation (LP). In case of $\Delta z = 0\,\mu$m the vector loop of $\boldsymbol{E}$ is a straight line. With increasing $|\Delta z|$ the opening of the loop increases. This effect is stronger when two electrodes deviate in distance from the tissue surface.

8.4.2 Influence of Power Line Interference [10]

Figure 8.16 shows the deviation in angle e_{φ_E} for varying amplitude of the power line interference signal. The three curves display the results of solely removing the base line (detrend 0), removing linear trend (detrend 1), and removing quadratic trend (detrend 2) prior to the computation of φ_E. The results in Figure 8.16 a) refer to an effective interference in one channel, whereas the results given in Figure 8.16 b) show the case when two channels are perturbed to the same extent.
The deviation in angle increases with increasing amplitude of the interference signal. An effective power line interference in two channels has a stronger effect on e_{φ_E}.

8.4.3 Estimation of Crossing Angle of Fibers [11]

Figure 8.17 a) shows the deviation between the angles of the vector loop of $\boldsymbol{E}$ (φ_1 and φ_2) and the direction of impulse propagation as functions of the crossing angle α of underlying muscle fibers for $\Delta\text{LAT}_1 = 1$ ms and $\Delta\text{LAT}_2 = 1.5$ ms. $e_{\varphi 1}(\alpha)$, the deviation of φ_1 from 180°, and $e_{\varphi 2}(\alpha)$, the deviation of φ_2 from the crossing angle of the fibers α, are not constant over the range of α but have a maximum at $\alpha \approx 120°$. The values of $e_{\varphi 1}(\alpha)$ for ΔLAT_1 and ΔLAT_2 are very similar and the corresponding curves in Figure 8.17 a) are not distinguishable.

---

[9] Methods, see p.63.

[10] Methods, see p.63.

[11] Methods, see p.63.

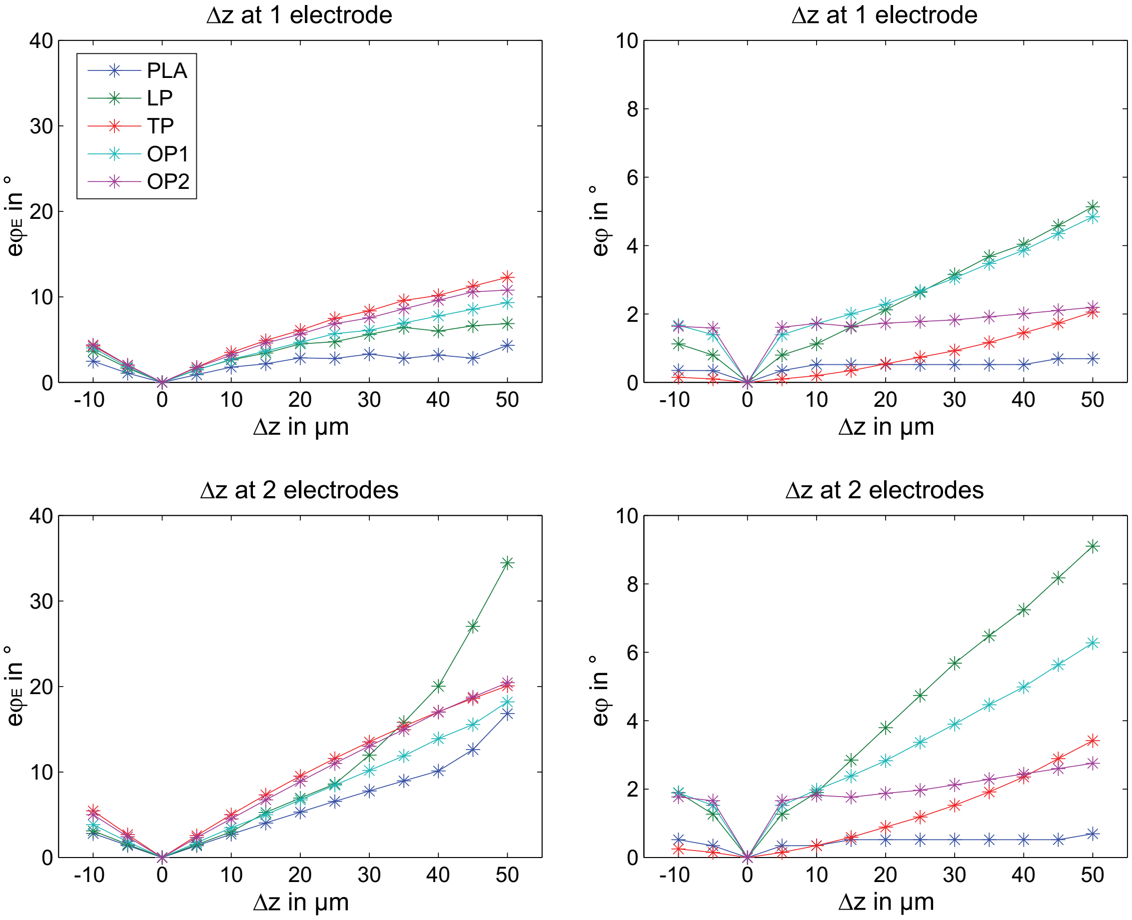

Figure 8.14: Influence of unequal electrode-tissue distances (deviation Δz) of a CNF sensor on the uncertainty of local direction of propagation φ. *Upper row:* Δz affecting one electrode. *Lower row:* Δz affecting two electrodes. *Left column:* eφ_E: Deviation of direction of propagation φ in ° determined from the CNF strength $\boldsymbol{E}$ (*Emag method*). *Right column:* eφ: Deviation of direction of propagation φ in ° determined from the vector of local conduction velocity $\boldsymbol{\theta}$ (*CCF method*). Different directions of propagation are plotted in different colors: *Blue*: planar (PLA), *green*: longitudinal (LP), *red*: transversal (TP), *cyan*: oblique (OP1), *purple*: oblique (OP2) direction of propagation.

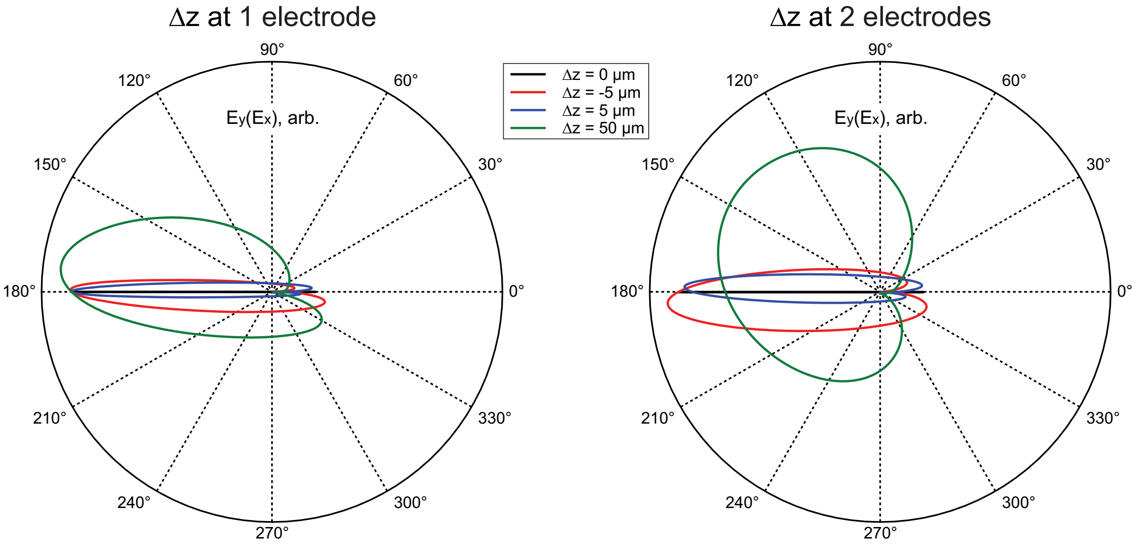

Figure 8.15: Influence of altered electrode-tissue distance one or two electrodes of a CNF sensor on the shape of the vector loop of $\boldsymbol{E}$ in case of LP. *Left diagram:* Δz affecting one electrode. *Right diagram:* Δz affecting two electrodes.

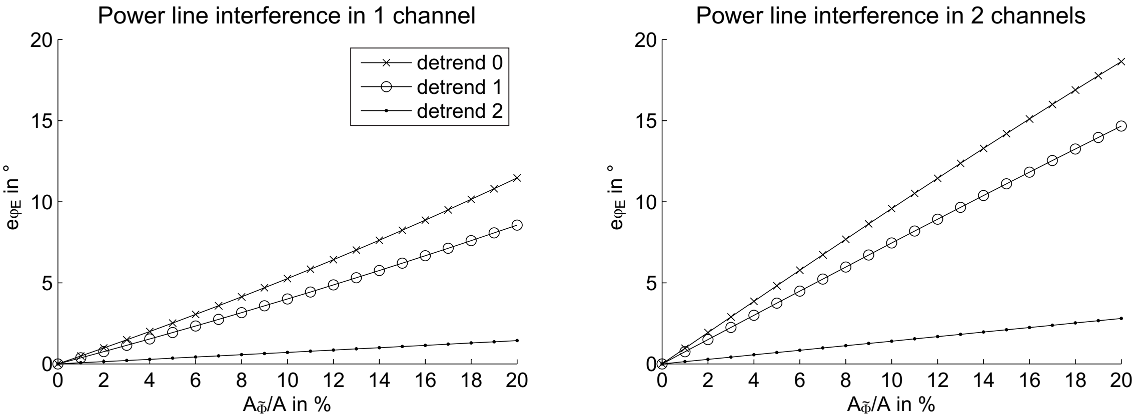

Figure 8.16: Deviation in angle φ_E due to 50 Hz power line interference. *Left diagram:* e_{φ_E} as a function of $A_{\tilde{\Phi}}/A$ after constant (detrend 0), linear (detrend 1), and quadratic (detrend 2) trend removal in case of an effective power line interference on one channel. *Right diagram:* Respective values for effective interference on two channels.

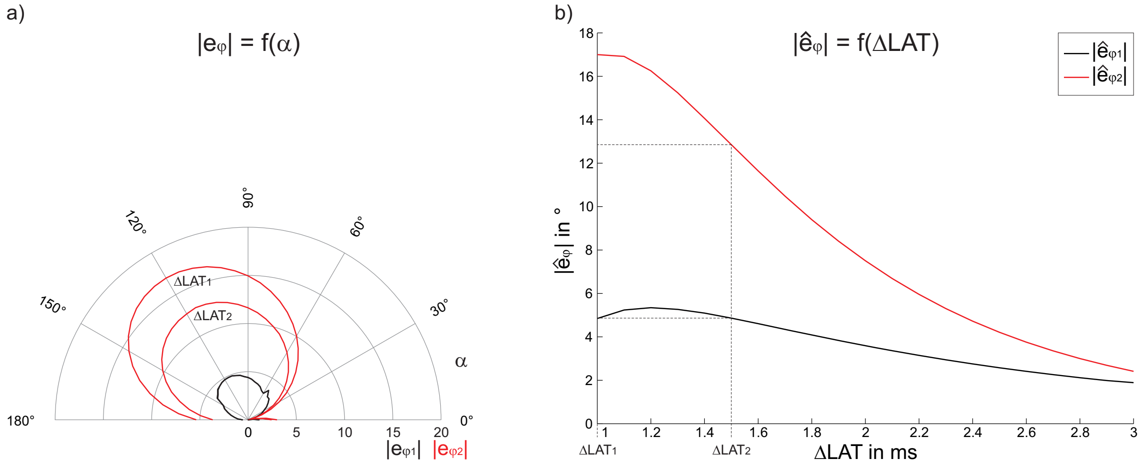

Figure 8.17: *a)* Deviations in angle of components $|e_{\varphi 1}|$ and $|e_{\varphi 2}|$ as functions of fiber crossing angle α for $\Delta\text{LAT}_1 = 1\,\text{ms}$ and $\Delta\text{LAT}_2 = 1.5\,\text{ms}$. Subfigure was adopted from [129]. *b)* Maximum values of $|\hat{e}_{\varphi 1}|$ and $|\hat{e}_{\varphi 2}|$ as functions of ΔLAT.

Figure 8.17 b) displays the maxima $\hat{e}_{\varphi 1}$ and $\hat{e}_{\varphi 2}$ as functions of ΔLAT. The values increase with decreasing ΔLAT until they level off for $\Delta\text{LAT} < 1.2\,\text{ms}$. Below $\Delta\text{LAT} = 1\,\text{ms}$ the activation events in the two fibers are not separable within the CNF strength $\boldsymbol{E}(t)$.

8.5 Evaluation of Fractionated Electrograms [12]

Figure 8.18 displays the results of the evaluation of algorithms *pCt* and *SM* for the detection of the fractionation index (FI). Subfigures 8.18 a) and 8.18 b) show that both algorithms are very robust against noise. The transition zones, where FI varies between 1 or 2 during the 100 runs is very narrow. The minimum ΔLAT for which FI=2 is detected varies with z. The reason for this is that with increasing z also the waveform of Φ gets expanded in time. That means the depolarization time t_{dep} increases linearly with z from $t_{dep} = 0.98\,\text{ms}$ for $z = 50\,\mu\text{m}$ to $t_{dep} = 1.84\,\text{ms}$ for $z = 300\,\mu\text{m}$.
The deviation in amplitude of component Φ_2 (e_{A2}) is solely shown for algorithm *SM* (Figure 8.18 f)), because algorithm *pCt* is not capable of reliably determining the magnitudes of the components, at least not for low values of ΔLAT in relation to t_{dep}.

The algorithm *SM* has been implemented in HARMS for on-line application. The computation time has been evaluated for 340 consecutive heart beats. Apart from the FI, LCV was determined using the *CCF* method (see Section 3.3.2). The computation time per beat (mean ± standard deviation) was $19 \pm 6\,\text{ms}$.

---

[12] Methods, see p.64.

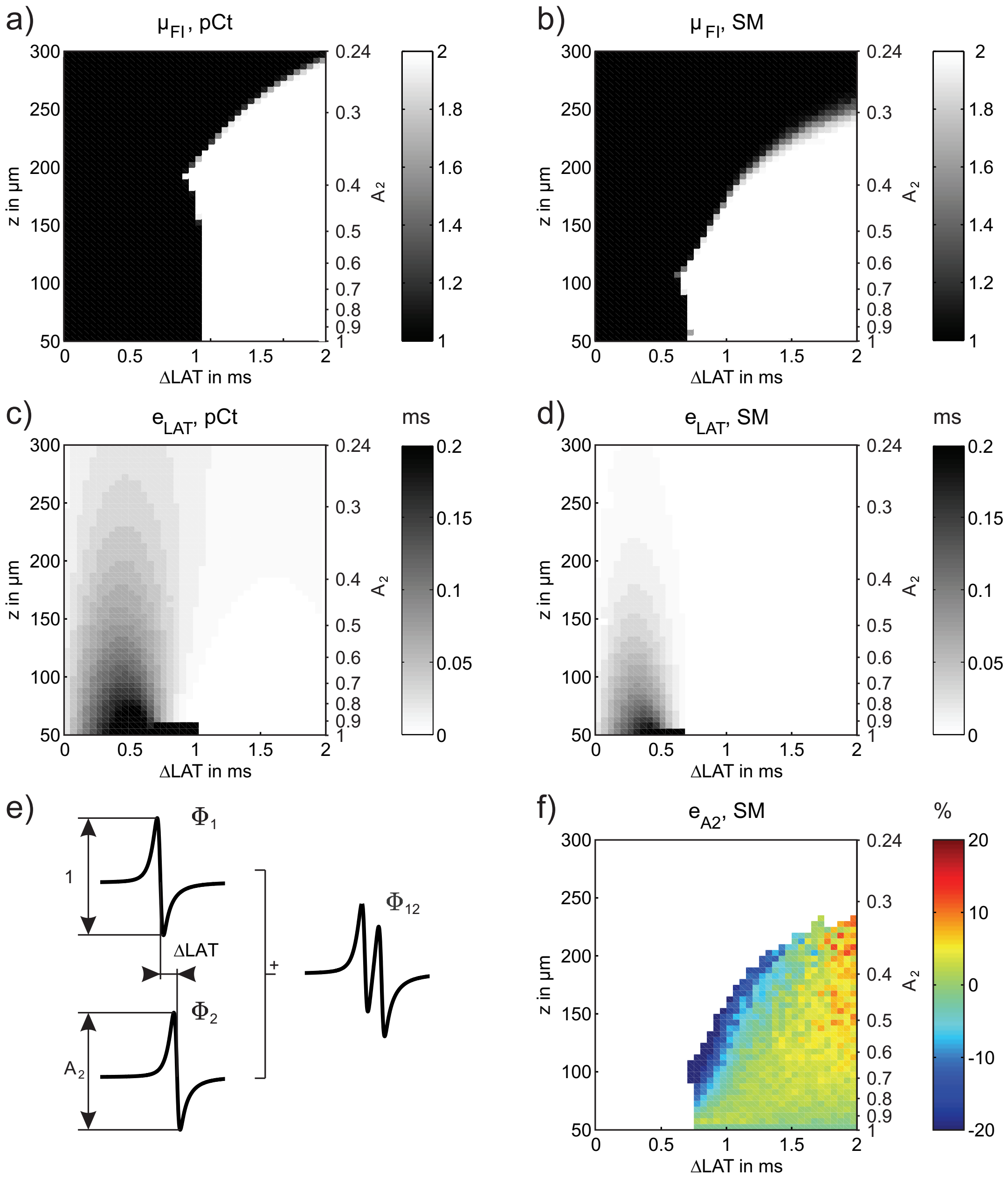

Figure 8.18: Evaluation of algorithms to determine fractionation index (FI). *a)* Mean of fractionation index μ_{FI} from 100 runs with regenerated noise (ANR = 38 dB) for peak count method (*pCt*). *b)* μ_{FI} for signal model-based method (*SM*). *c)* Deviation in local activation time (e_{LAT}) for dominant component Φ_1, *pCt* method. Values were clipped at $e_{LAT} \geq 0.2$. The maximum value $\hat{e}_{LAT}$ was 0.534 ms. *d)* e_{LAT}, *SM* method, $\hat{e}_{LAT} = 0.694\,\text{ms}$. *e)* Generation of fractionated electrograms Φ_{12} from two nonfractionated components (Φ_1 and Φ_2), temporally separated by ΔLAT. *f)* Deviation in amplitude of component Φ_2. Values were clipped at $-20\,\% < e_{A2} < 20\,\%$. Maximum positive deviation $\hat{e}^{+}_{A2} = 12.41\,\%$, maximum negative deviation $\hat{e}^{-}_{A2} = -49.42\,\%$, mean deviation $\mu_{eA2} \pm \sigma_{eA2} = -1.88 \pm 9.09\,\%$.

8.6 Decomposition of Fractionated Electrograms [13]

The synthesis of fractionated electrograms Φ_{12} from the components Φ_1 and Φ_2 and the decomposition into Φ_{m1} and Φ_{m2} are illustrated in Figure 8.19 (a).

Figure 8.19 (b) displays FI for the range of $0.5 \leq \Delta\text{LAT} \leq 3\,\text{ms}$ and $50 \leq z \leq 300\,\mu\text{m}$. The minimum value of ΔLAT for which FI=2 is detected is 0.6 ms for $50 \leq z \leq 95\,\mu\text{m}$, then increases with increasing z (cf. Section 8.5).

For $\Delta\text{LAT} = 1\,\text{ms}$ three sites A), B), and C) with $z = 50$, 100, and $250\,\mu\text{m}$, respectively, were selected. Φ_1, Φ_2, and Φ_{12} as well as Φ_{m1}, Φ_{m2}, and Φ_{m12} for sites A), B), and C) are plotted in Figure 8.19 (c). In point C), FI=1 was detected and therefore only Φ_{m1} was modeled.

For each z, Figure 8.19 (d) shows the respective minimum ΔLAT for which the parameters B_1, b_1, and t_{depm1}, determined from Φ_{m1}, have an error which is within the given tolerance band. $\Delta\text{LAT}_{min,B_1} \leq 0.7\,\text{ms}$ for all values of z, whereas $\Delta\text{LAT}_{min,b_1}$ and $\Delta\text{LAT}_{min,t_{depm1}}$ slightly increase with increasing z.

In Figure 8.19 (e), ΔLAT for the parameters determined from the second component Φ_{m2} are given. From 0.7 ms for $z = 50\,\mu\text{m}$, $\Delta\text{LAT}_{min,B_2}$, $\Delta\text{LAT}_{min,b_2}$, and $\Delta\text{LAT}_{min,t_{depm2}}$ increase with increasing z.

Figure 8.20 depicts the results for the 2D-setup with two embedded obstacles. Isochrones based on local activation time were calculated from transmembrane voltages (Figure 8.20 (a)), which remained nonfractionated throughout the entire sheet, including the vicinity of the obstacles. Their density and curvature reflect the substantial variations in local conduction velocity and direction of propagation around the obstacles. The activation wavefront remains largely undisturbed until encountering with the lower left corner of *obs1* which leads to acceleration of propagation due to reduced electrotonic load downstream and reduced wavefront curvature.

The bold isochrone demonstrates the split of a wavefront into three components, α, β, and γ. For recordings at sites $\mathbf{p_1}$ and $\mathbf{p_2}$ on top of *obs1* and *obs2*, the wavefront components pass by with delays of roughly $0.7\ldots0.8\,\text{ms}$ between α and β as well as between β and γ which is responsible for the fractionation of Φ.

In the vicinity of the obstacles extracellular potentials Φ at $z = 50\,\mu\text{m}$ were fractionated, showing either 2 or 3 distinct components (Figure 8.20 (b)). Within the observation area percentages of Φ with FI=1, 2, and 3 were 33%, 20%, and 47% (N=602). The goodness of fit parameters and their distribution are shown in Figure 8.20 (c)-(f).

The application of the decomposition procedure to an experimentally recorded multivariate electrogram $\boldsymbol{\Phi}$ is demonstrated in Figure 8.21. The fractionated waveform $\boldsymbol{\Phi}$ (FI=3) is decomposed into three components. The comparison between recorded and modeled waveform is presented.

---

[13] Methods, see p.67.

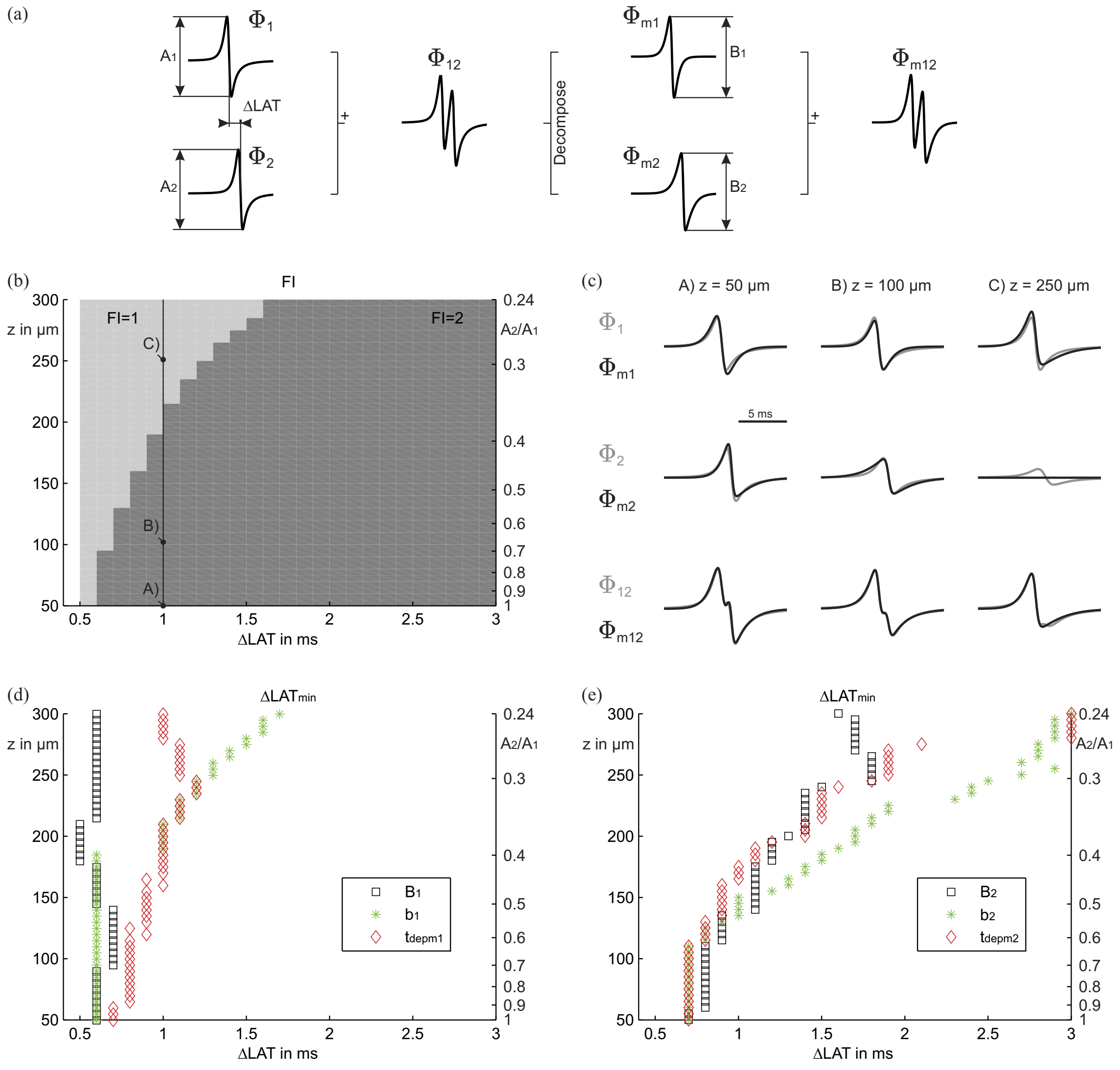

Figure 8.19: Limitations for the decomposition of fractionated local electrograms: *(a)* Principle of synthesizing fractionated electrograms Φ_{12} by adding Φ_1 and Φ_2 as evoked by *strand 1* and *strand 2* and decomposing into Φ_{m1} and Φ_{m2}. *(b)* Fractionation index (FI) for the range of ΔLAT and z. *(c)* Φ_1, Φ_2, and Φ_{12} as well as Φ_{m1}, Φ_{m2}, and Φ_{m12} for points A), B), and C). *(d)* ΔLAT_{min}: Lower limit of ΔLAT for which the errors of amplitude B_1, symmetry b_1, and depolarization time t_{depm1} determined from Φ_{m1} go below the given tolerances ($\pm 20\%$ for B and t_{dep}, ± 0.2 for b). *(e)* ΔLAT_{min} for parameters B_2, b_2, and t_{depm2} determined from Φ_{m2}. Figure adopted from [128].

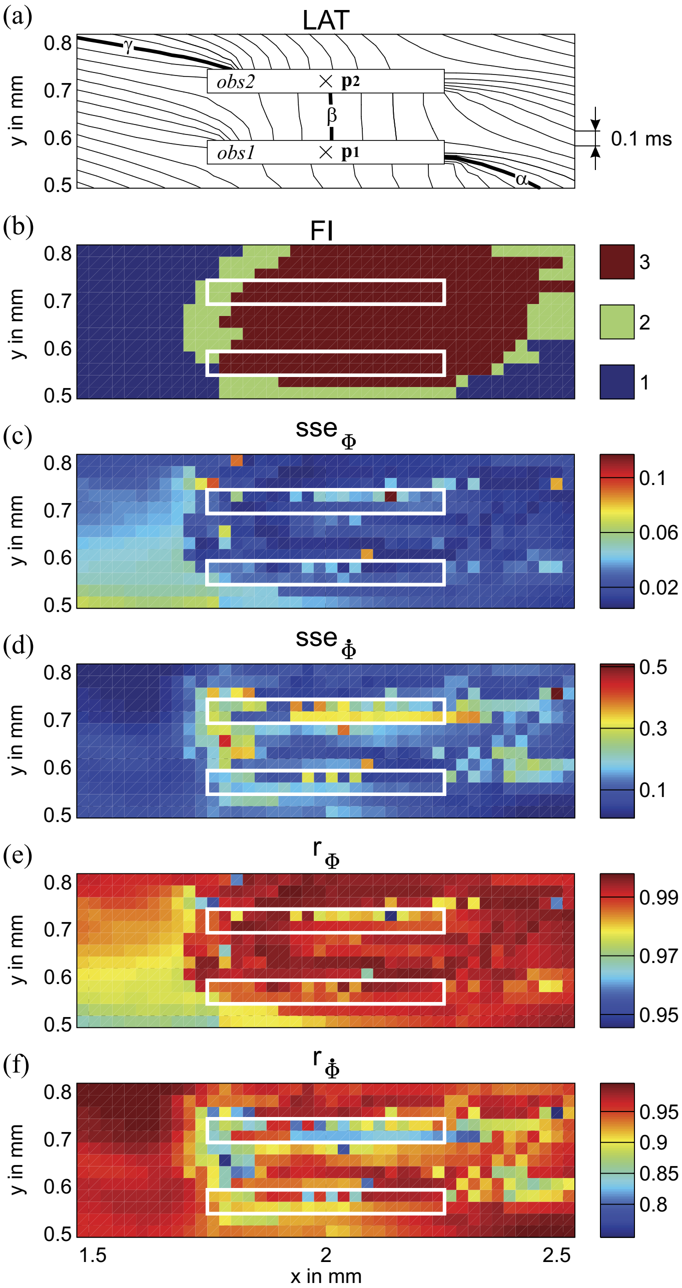

Figure 8.20: Spatial distribution of electrogram fractionation of Φ caused by microobstacles. *(a)* Isochrones of local activation time derived from transmembrane voltages. The bold isochrone highlights wavefront fragmentation into three components α, β, and γ. Delays between components in wavefront arrival are measured at sites $\mathbf{p_1}$ and $\mathbf{p_2}$. *(b)* Fractionation index of Φ (FI). *(c)*, *(d)* Sum of squared errors of Φ (sse_Φ) and $\dot{\Phi}$ ($sse_{\dot{\Phi}}$). *(e)*, *(f)* Correlation coefficient of Φ (r_Φ) and $\dot{\Phi}$ ($r_{\dot{\Phi}}$). Figure adopted from [128].

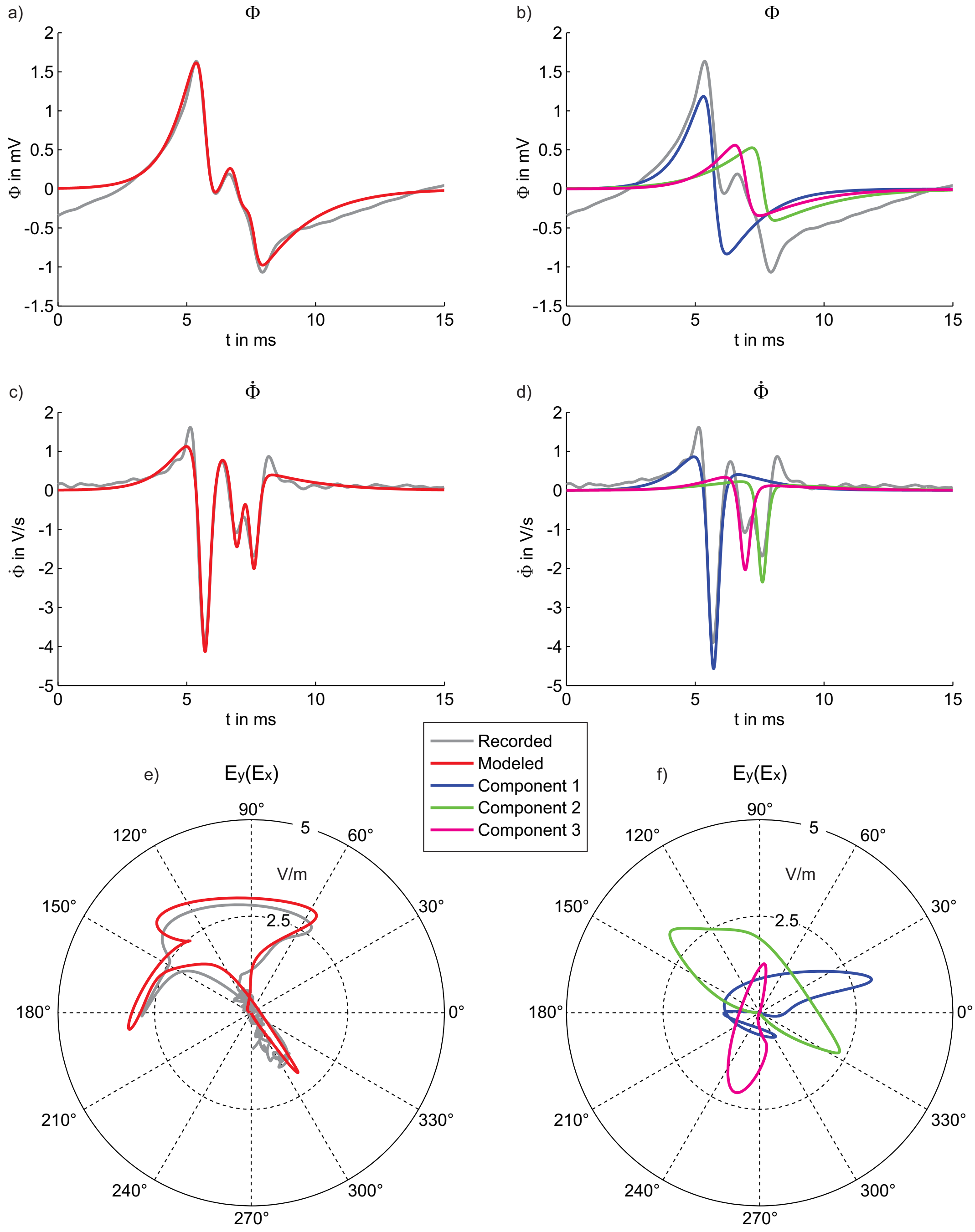

Figure 8.21: Decomposition of an experimentally recorded electrogram $\mathbf{\Phi} = [\Phi_1 \; \Phi_2 \; \Phi_3 \; \Phi_4]^T$ with FI=3. *a)* Recorded electrogram Φ_1 and Φ_{m1} after decomposition and synthesis. *b)* Components $\Phi_{m1,1}$, $\Phi_{m1,2}$, and $\Phi_{m1,3}$ of Φ_{m1}. *c)* Temporal derivatives $\dot{\Phi}_1$ and $\dot{\Phi}_{m1}$. *d)* Temporal derivatives $\dot{\Phi}_{m1,1}$, $\dot{\Phi}_{m1,2}$, and $\dot{\Phi}_{m1,3}$. *e)* Vector loop of $\boldsymbol{E}$ computed from $\mathbf{\Phi}$ and $\mathbf{\Phi}_m$. *f)* Vector loops of $\boldsymbol{E}$ computed from $\mathbf{\Phi}_{m,1}$, $\mathbf{\Phi}_{m,2}$, and $\mathbf{\Phi}_{m,3}$.

Table 8.9: Branching simulation: Local conduction velocities in m/s at recording sites Pos. 1 and Pos. 2 for different stimulus sites (PLA, LP, and OP) and different intracellular conductivities ($0.5\,g_I$ and $1\,g_I$).

	PLA		LP		OP	
Pos.	1	3	1	3	1	3
$0.5\,g_I$	0.444	0.446	0.444	0.409	0.444	0.323
$1\,g_I$	0.628	0.633	0.618	0.430	0.629	0.304

8.7 Discrimination of Local and Distant Activation

8.7.1 Computer Simulation Study [14]

The values of $(\ddot{\Phi}_{pp} : \dot{\Phi}_{pp})(z)$ and $(|\dot{\boldsymbol{E}}|_{pp} : |\boldsymbol{E}|_{pp})(z)$ differ substantially for different fiber diameters as well as for different directions of the propagating activation wavefront with respect to the fiber orientation (see Figure 8.22 a) and b), respectively). The values of $(\ddot{\Phi}_{pp} : \dot{\Phi}_{pp})(z)$ in case of TP, OP1, and OP2 do not show a monotonic decay because they were affected by artifacts which arose in $\ddot{\Phi}$ due to border effects in the simulated tissue sheet.

In Figure 8.23 the measures $(\ddot{\Phi}_{pp} : \dot{\Phi}_{pp})(z)$ and $(|\dot{\boldsymbol{E}}|_{pp} : |\boldsymbol{E}|_{pp})(z)$ obtained at Pos. 1 and Pos. 3 are given for different stimulus settings (PLA, LP, OP), and different intracellular conductivities ($0.5\,g_I$ and $1\,g_I$). The dispersion of both measures is quite high, especially in case of stimulus setting OP.

Table 8.9 lists respective local conduction velocities θ determined from the transmembrane voltages $\boldsymbol{V}_m$. At Pos. 1, θ is equal for different stimulus positions. As expected, for planar wavefront of activation (PLA), θ is equal at Pos. 1 and Pos. 3. For stimulus settings LP and OP, θ at Pos. 3 is reduced but remains widely unchanged when the intracellular conductivity is twice as high.

Figure 8.24 displays the measures $(\ddot{\Phi}_{pp} : \dot{\Phi}_{pp})(d)$ and $(|\dot{\boldsymbol{E}}|_{pp} : |\boldsymbol{E}|_{pp})(d)$ obtained at Pos. 2, between the tissue branches, for stimulus setting OP and intracellular conductivities $0.5\,g_I$ and $1\,g_I$. d represents the distance to the closest current source, which is not directly beneath observation Pos. 2 and calculates as follows: $d = \sqrt{z^2 + (b/2)^2}\,\mu\mathrm{m}$, where $b = 425\,\mu\mathrm{m}$ is the width of the obstacle.

---

[14] Methods, see p.71.

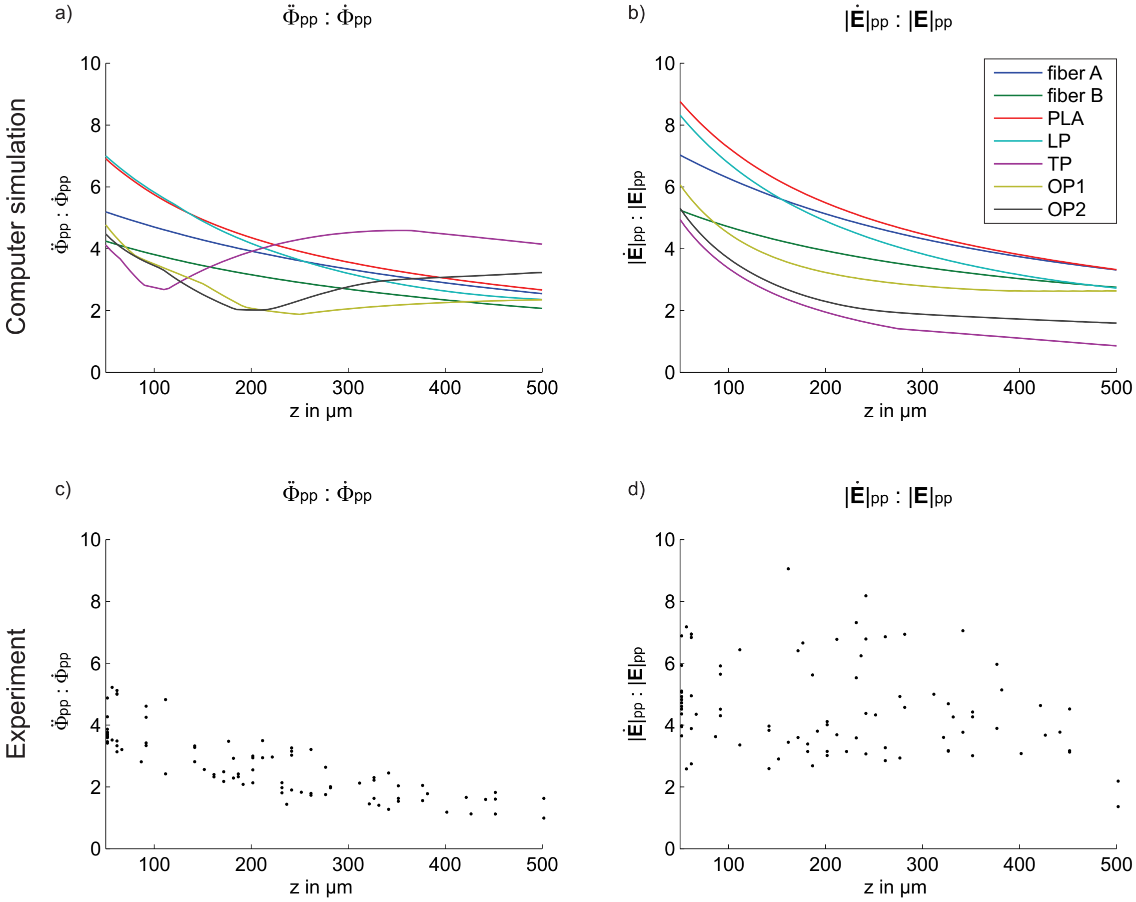

Figure 8.22: Distance measures. *a)* $\ddot{\Phi}_{pp} : \dot{\Phi}_{pp}$ as function of the distance z between tissue surface and point of observation for fiber A, 0.25 mm diameter, (blue line), fiber B, 1 mm diameter, (green), tissue sheet with planar (PLA, red), longitudinal elliptic (LP, cyan), transversal elliptic (TP, magenta), and oblique elliptic (OP1, yellow and OP2, black) propagation of activation. *b)* Respective curves for $(|\dot{\boldsymbol{E}}|_{pp} : |\boldsymbol{E}|_{pp})(z)$. *c)* Experimental results for $(\ddot{\Phi}_{pp} : \dot{\Phi}_{pp})(z)$. *d)* Experimental results for $(|\dot{\boldsymbol{E}}|_{pp} : |\boldsymbol{E}|_{pp})(z)$.

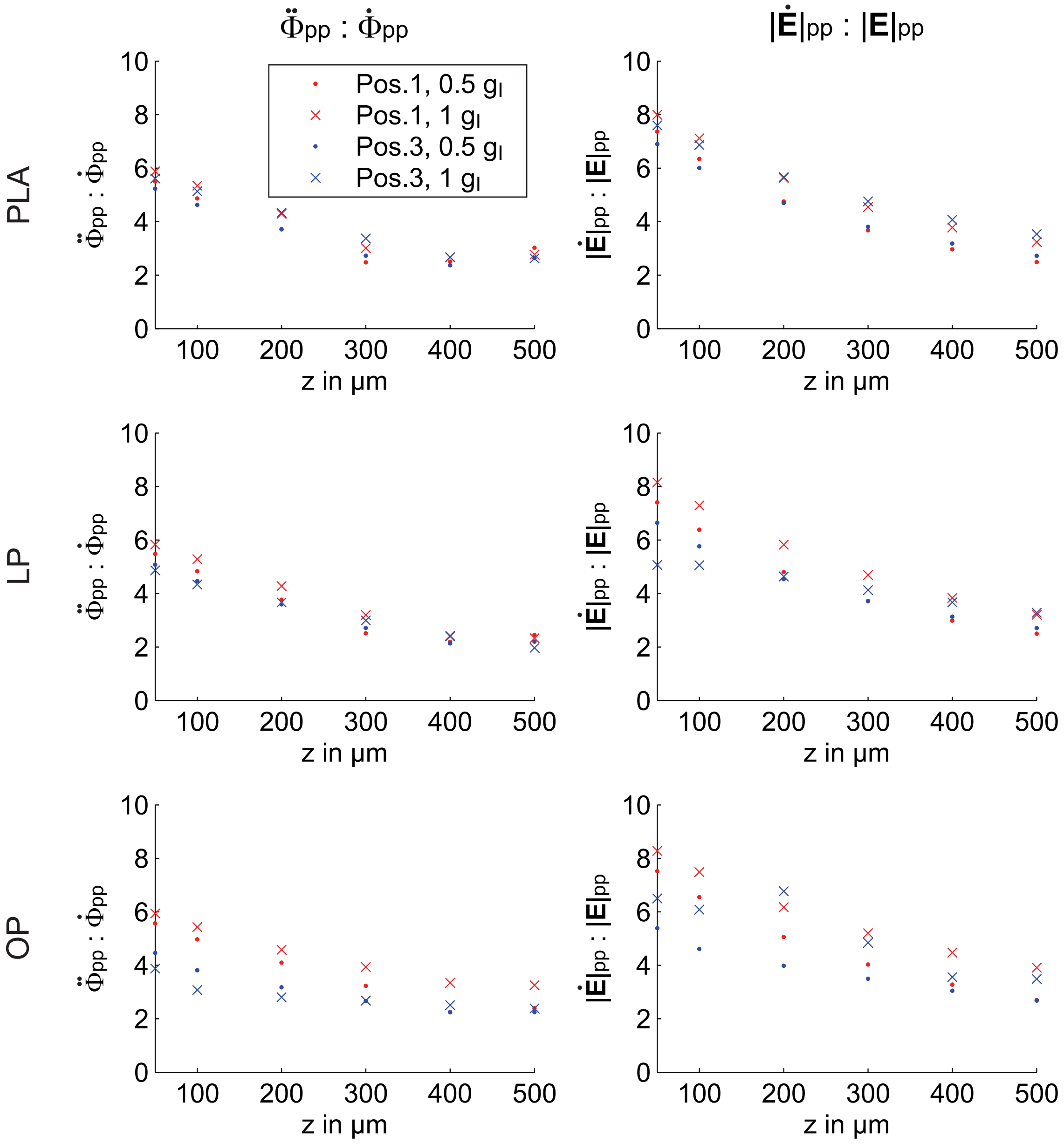

Figure 8.23: Distance measures. *Left column:* $\ddot{\Phi}_{pp} : \dot{\Phi}_{pp}$ as function of the distance z between tissue surface and point of observation for planar (PLA, upper row), longitudinal elliptic (LP, middle row), and oblique elliptic propagation (OP, lower row) determined at Pos. 1 in the thin tissue branch (red markers) and Pos. 3 in the thick tissue branch (blue markers). Different conductivities are marked by dots ($0.5\, g_I$) and crosses ($1\, g_I$). *Right column:* Respective values for $(|\dot{\boldsymbol{E}}|_{pp} : |\boldsymbol{E}|_{pp})(z)$.

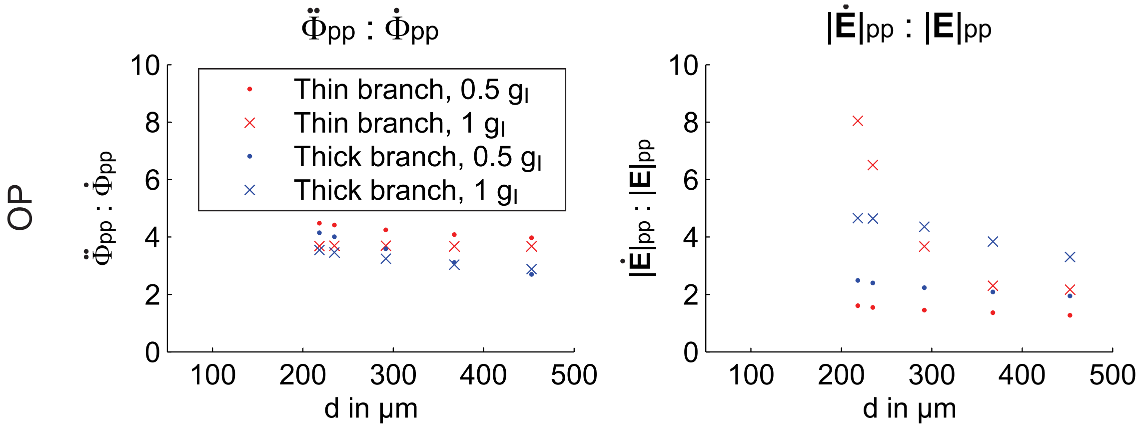

Figure 8.24: Distance measures. *Left diagram:* $\ddot{\Phi}_{pp} : \dot{\Phi}_{pp}$ as function of the distance d between tissue surface and point of observation for oblique elliptic propagation (OP) determined at Pos. 2 between the tissue branches. Red markers indicate the contribution of the thin tissue branch, blue markers the contribution of the thick tissue branch. Different intracellular conductivities are marked by dots ($0.5\,g_I$) and crosses ($1\,g_I$). *Right diagram:* Respective values for $(|\dot{\boldsymbol{E}}|_{pp} : |\boldsymbol{E}|_{pp})(d)$.

8.7.2 Experimental Study [15]

A total number of 94 recordings of $\boldsymbol{\Phi}$ taken from 6 different sites at the surface of 3 different papillary muscles have been analyzed. The collective values of $(|\ddot{\Phi}|_{pp} : |\dot{\Phi}|_{pp})(z)$ and $(|\dot{\boldsymbol{E}}|_{pp} : |\boldsymbol{E}|_{pp})(z)$ are shown in Figure 8.22 c) and d), respectively. The ranges of both measures determined from CNF signals recorded during experiments are in accordance with those determined from signals obtained from computer simulations. For $(|\ddot{\Phi}|_{pp} : |\dot{\Phi}|_{pp})(z)$, the decay with increasing z is comparable to that of signals obtained from computer simulation, whereas $(|\dot{\boldsymbol{E}}|_{pp} : |\boldsymbol{E}|_{pp})(z)$ rather shows arbitrary values. The dispersion of both measures is quite high.

8.8 Classification of Tissue Microstructure through CNF Signals [16]

Figure 8.25 gives examples of determined parameters μ_{FI} and μ_{amp} for three different tissue classes, namely WC, PO, and CO. The diagrams show the results for $M = 12$ and $d = 100\,\mu$m. In an effort to compare the diagrams between the tissue classes, the following observations were made. In well coupled tissue (e.g. WC1), μ_{FI} and ΔFI are relatively low, whereas μ_{amp} and Δamp are high. In tissue with uncoupling structures oriented parallel to the cardiac fibers (e.g. PO1), ΔFI and Δamp are high and μ_{amp} is lower than in case of WC1. In tissue with complex arrangement of uncoupling structures (e.g. CO1), μ_{amp} and Δamp are very low, whereas μ_{FI} is high and ΔFI is moderate.

---

[15] Methods, see p.73.

[16] Methods, see p.74.

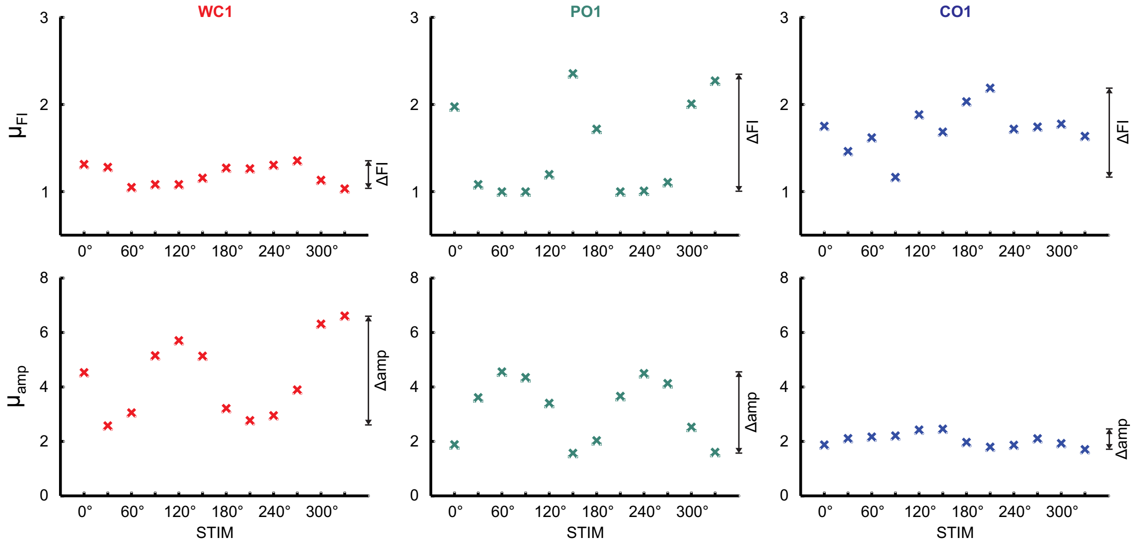

Figure 8.25: Features for the classification. Examples for different tissue classes: WC (diagrams in left column), PO (center column), and CO (right column). *Upper diagrams:* μ_{FI} as function of the stimulus position STIM. *Lower diagrams:* μ_{amp} as function of STIM.

Figure 8.26 shows the samples (m_{FI}, ΔFI, ξ_{amp}) for one configuration ($d = 600\,\mu$m and $M = 3$) in the three-dimensional feature space. The clustering of the samples suggests a good separability into the three classes WC, PO, and CO.

Tables 8.10, 8.11, and 8.12 present the results of the classification. Classification accuracies for each of the three classes (acc_1 for WC, acc_2 for PO, and acc_3 for CO) as well as the overall accuracy acc_{tot} are given. For each sample set, the number of recording sites (i.e. the number of points in the measurement grid) is listed. The number of sample sets results from the number of tissue samples (6), the number of rotations in the arrangement of the stimulus electrodes, and the number of variations in the positioning of the measurement grid.

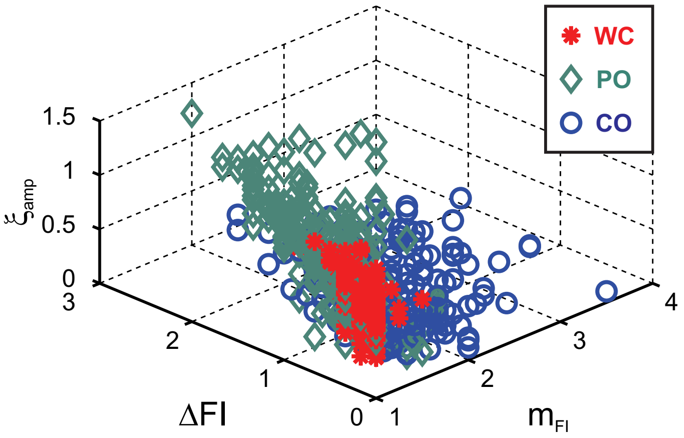

Figure 8.26: Feature space: 3D-plot of m_{FI}, ΔFI, and ξ_{amp} for grid length $d = 600\,\mu$m and $M = 3$ stimulus sites yielding 648 samples. Samples from different classes are indicated by red asterisks (WC), green diamonds (PC), and blue circles (CO).

Table 8.10: Classification results for $M = 12$ stimulus sites, for features obtained from electrograms recorded in a grid with varying length d. Classification accuracies for each of the three classes (acc_1, acc_2, and acc_3) as well as the overall accuracy acc_{tot} are given.

d in μm	Recording sites	Sample sets	acc_1	acc_2	acc_3	acc_{tot}
100	121	6	1.00	1.00	1.00	1.00
200	36	24	1.00	1.00	1.00	1.00
300	15	54	1.00	1.00	1.00	1.00
400	9	96	0.97	0.97	1.00	0.98
600	4	216	0.93	0.91	0.99	0.94

Table 8.11: Classification results for $M = 6$.

d in μm	Recording sites	Sample sets	acc_1	acc_2	acc_3	acc_{tot}
100	121	12	1.00	1.00	1.00	1.00
200	36	48	1.00	1.00	1.00	1.00
300	15	108	0.96	0.96	1.00	0.97
400	9	192	0.98	0.98	1.00	0.98
600	4	432	0.90	0.87	0.99	0.92

Table 8.12: Classification results for $M = 3$.

d in μm	Recording sites	Sample sets	acc_1	acc_2	acc_3	acc_{tot}
100	121	18	1.00	0.83	0.83	0.89
200	36	72	1.00	0.87	0.88	0.92
300	15	162	1.00	0.87	0.89	0.92
400	9	288	0.99	0.84	0.87	0.90
600	4	648	0.90	0.70	0.85	0.82

Chapter 9

Discussion

9.1 Signal and Noise Analysis of CNF Signals

Median and lower quartile of the distribution of the ANR listed in Table 8.1 were considered to represent average ($\mathrm{ANR}_{.50}$) and poor signal quality ($\mathrm{ANR}_{.25}$), respectively. These values were consequently used for the generation of artificial noise added to noise-free waveforms from computer simulations in order to test the robustness of developed signal processing algorithms. The reason for the use of the ANR instead of the noise level is the fact that waveforms from computer simulations have arbitrary magnitude scaling. Previously given numbers for ANR distribution of nonfractionated electrograms were considerably higher, namely $\mathrm{ANR}_{.25} = 54.16\,\mathrm{dB}$, $\mathrm{ANR}_{.50} = 57\,\mathrm{dB}$, and $\mathrm{ANR}_{.75} = 60.35\,\mathrm{dB}$ [76]. The reason for this is that electrograms had mainly been recorded at ventricular tissue preparations showing higher amplitudes. CNF signal amplitudes in the atrium are very low compared to other regions of the heart. This is, on one hand due to the structural complexity and on the other hand due to the functional heterogeneities, especially in the terminal crest where the primary pacemaker area is located. Moreover, measurement in a superfusion bath introduces a huge volume conductor which leads to very low local current densities. In contrast, in the Langendorff perfused isolated heart (see Section 4.1.2) the volume conductor is formed by a thin film of perfusate. The resulting high extracellular current densities result in large amplitudes of the electrograms compared to measurements in a superfusion bath.

The separate statistical analysis of nonfractionated and fractionated electrograms has shown that Φ_{pp}, $\dot{\Phi}_{pp}$, ANR, and $|\boldsymbol{E}|_p$ are on average higher in nonfractionated electrograms. This finding has been considered for the development of dedicated signal processing algorithms.

The very high correlation between Φ_{pp} and $\dot{\Phi}_{pp}$ is due to the fact that signals were recorded at fairly constant distance from the surface of the cardiac tissue (cf. Section 6.7).

From the separate analysis of the PSD of the noise emerging from the amplifier circuit only and from the entire measurement chain, respectively, it is obvious that the major noise source in the measurement chain is the electrode-electrolyte interface. The increased PSD of the measurement noise at low frequencies is due to the 50 Hz power line interference. The Welch method and the frequency resolution of the PSD lead to a smoothing of the PSD curve at these frequencies. Therefore, the interference is not represented by a distinct peak.

The finding that noise power of difference signals of any two channels is not different from that of individual signals is due to the high common mode rejection of the amplifier circuit [54].

Based on the presented results, the noise induced by the measurement chain was represented by additive Gaussian band limited white noise and individually created for each recording channel.

Computer simulations of CNF signals directly acquired at the surface of the tissue have shown that the theoretical maximum frequency component occurs not beyond $f = 10\,\mathrm{kHz}$. According to the sampling theorem, the minimum required sampling frequency f_S to avoid aliasing is $f_S = 20\,\mathrm{kHz}$. The used measurement system contains an anti-aliasing lowpass filter with a cutoff frequency $f_C = 20\,\mathrm{kHz}$. Taking the finite slope in the stopband of the filter into account, the theoretical minimum sampling frequency $f_S = 40\,\mathrm{kHz}$ needs to be exceeded. Sampling rates $f_S \geq 100\,\mathrm{kHz}$ were used in order to resolve the small latencies between the densely packed electrodes with the necessary accuracy. A reduction of this uncertainty, however, can be achieved by digital resampling, as shown in Section 7.2.1. Hence, for the CNF measurement system in use, f_S may be reduced by the factor of 2, i.e. to about $f_S = 50\,\mathrm{kHz}$, without loss of information. For future developments, a further reduction down to $f_S = 20\,\mathrm{kHz}$ is feasible, provided that appropriate anti-aliasing filters are applied prior to the digitalization. The display of smooth vector loops of $\boldsymbol{E}$ can then be achieved by on-line digital resampling. This operation has been implemented in HARMS and has turned out to be feasible as far as computational expense is concerned. Moreover, a reduction by the factor of 5 of the amount of data to be acquired, preprocessed (filtered, etc.), and stored means a significant gain in computational power which can be utilized for computationally intensive on-line signal processing.

9.2 Determination of Local Conduction Velocity

The reasons for uncertainty of LCV are on one hand the limited temporal resolution in LAT latencies, and on the other hand noise.

It was shown that the temporal resolution of Φ can be increased by means of digital resampling. Given an inter-electrode distance of $\mathrm{DD} = 70\,\mu\mathrm{m}$, as in the used CNF sensors,

an interpolation factor M = 20 and thus a temporal resolution of $0.5\,\mu$s is sufficient so that the uncertainty of θ and φ due to the temporal discretization may be neglected, as shown in Figure 8.5.
Hence, the reason for the overall uncertainty of θ and φ may be reduced to the influence of noise.
Two opposed mechanisms determine the robustness of LCV determination in the presence of noise. First, higher conduction velocity is related to higher amplitudes of Φ and thus a higher signal-to-noise ratio. Second, higher conduction velocity means smaller delay between two measurement sites and thus a higher uncertainty in LCV determination.

The uncertainty of θ and φ due to noise increases with increasing ANR. The appropriate cutoff frequency of a lowpass filter for Φ prior to the computation of θ and φ using the *CCF method* or the *dmin method* was determined as $f_C = 1.5\,$kHz. Using the *Emag method* to compute φ, $f_C = 2.5\,$kHz is being suggested. During the experiment it is desirable to be aware of the overall uncertainty of the determined θ and φ which depends on the inter-electrode distance DD, the ANR, and the magnitude θ of LCV. The values displayed in Figures 8.8 and 8.9 may be implemented as lookup tables in HARMS for on-line calculation and display of the uncertainty of θ and φ. At the beginning of an electrophysiological experiment with CNF measurement it is necessary to determine the noise level, i.e. the standard deviation σ_N of a signal representing the noise of the measurement chain. It has turned out that σ_N remains fairly constant throughout the experiment using the described CNF sensors [54]. Thus, along with the on-line determined values of Φ_{pp} and θ, the uncertainty of θ and φ can be determined and displayed from beat-to-beat.

The comparison of LCV (θ and φ) determined from $\boldsymbol{V_m}$ and $\boldsymbol{\Phi}$ has shown considerable differences in regions with strong curvature of the activation wavefront. The reason for this might be that the curvature is reduced with increasing distance from the surface of the tissue due to the spatial integration effect of the volume conductor surrounding the tissue. In case of a fairly planar wavefront of activation, the deviations e_θ and e_ϕ are negligible and LCV determined from $\boldsymbol{\Phi}$ represents well LCV determined from $\boldsymbol{V_m}$.
In the vicinity of microstructural obstacles for impulse propagation, the values of θ and φ determined from $\boldsymbol{\Phi}$ differ dramatically from those determined from $\boldsymbol{V_m}$. This may have two reasons. First, as in the continuous case, the spatial integration effect of the volume conductor which might alter activation times determined from $\boldsymbol{\Phi}$, and second, erroneous LAT's computed from the fractionated electrograms in such areas.

9.3 Analytic Signal Model of Extracellular Electrogram

Exponential functions have been used previously to model bioelectric signals. For instance, Chouvarda *et al.* used a modified Morita function to model the waveform of the transmembrane current in a cardiac muscle fiber [119], or van Veen *et al.* used exponential functions to represent single fiber action potentials of skeletal muscles [134]. The described templates, however, turned out to be not sufficiently versatile for the purpose of modeling the various shapes of CNF signals as the dedicated signal model presented in this work.

Figure 8.13 and Tables 8.7 and 8.8 clearly demonstrate the suitability of the introduced signal model for representing a wide range of wave shapes of nonfractionated electrograms. This includes waveforms emerging from starting, free running, and terminating/colliding wavefronts of activation at different distances from the current sources. As expected, differences in the goodness of fit between atrial and ventricular electrograms were negligible, because the modeling is restricted to the depolarization phase, which has a similar time course in the underlying action potentials. The noticeable residuals e_Φ in the case of a starting wavefront, as shown in the left panels of Figure 8.13, are due to the stimulus artifact. In case of electrograms representing starting activation caused by structural discontinuities like tissue expansions (cf. Section 3.4.1), such stimulus artifacts would not occur.

9.4 Analysis of Vector Loops of CNF Strength

It was shown that altered distance Δz between a single electrode or an electrode pair compared to the remaining electrodes of a CNF sensor with respect to the surface of the tissue has a tolerable influence on the angle of propagation φ_E, determined from $\boldsymbol{E}$. However, even $|\Delta z| = 5\,\mu\text{m}$ may significantly affect the morphology of the vector loop of $\boldsymbol{E}$. The influence of a sensor tilt on φ, determined from $\boldsymbol{\theta}$, is considerably smaller.

Interference signals of the power line may cause a significant bias in the angle of propagation φ, determined from $\boldsymbol{E}$. This may be alleviated by linear or quadratic detrending, when the considered signal window has a length of 10 ms, as in the presented study. The power line interference and the detrending methods were not investigated if Φ is asymmetric, like in case of initiating, terminating, or colliding activation wavefronts or as occasionally seen in fractionated electrograms.

The amplitude of the power line interference $\mathrm{A}_{\tilde{\Phi}}$ in the recorded electrograms may vary during an experiment because of the changes in the cabling and operation of power line driven electric devices in the vicinity of the experimental setup. During test recordings carried out without preparation, $\mathrm{A}_{\tilde{\Phi}} \approx 50\,\mu\text{V}$ was determined. In case of a relation to the signal amplitude $\mathrm{A}_{\tilde{\Phi}}/\mathrm{A} = 20\%$, which was used as maximum value for $\mathrm{A}_{\tilde{\Phi}}/\mathrm{A}$, this corresponds to a CNF signal amplitude $A = 0.25\,\text{mV}$.

The identification of amplitude and phase of the interference signal and consequently its cancellation may be achieved for longer lasting signal recordings. Another option how to reduce or cancel power line interference is the application of an adaptive filter to the

CNF signals before recording [135]. These methods are taken into consideration for future signal recordings.

The CNF technique is limited to detecting propagation of activation in parallel to the surface of the tissue. In thin preparations like the right atrial isthmus (see Section 4.1.2) this can be assumed without risking substantial errors. Nevertheless, it should be emphasized that CNF technique leads to a two-dimensional representation of three-dimensional impulse propagation phenomena. In in-vitro experiments with isolated entire hearts mounted on the Langendorff apparatus and in in-vivo application, however, impulse propagation differing from in parallel to the surface and particularly break-through points, where the activation propagates perpendicularly to the surface of the tissue, need to be taken into consideration. At the ventricles, break-through points are widespread because at the junction of Purkinje fibers with myocardium the activation propagates transmurally[1]. In this case, the CNF strength vanishes if the activation propagates transversal to the tissue surface or the long axis of the sensor, respectively. However, nonfractionated electrograms showing normal amplitudes but unrealistically high values of LCV, low CNF strength, and very small vector loops, respectively, may be potential indicators of break-through points of impulse propagation.

In electrophysiological in-vitro experiments the on-line display of the vector loop of $\boldsymbol{E}$ has turned out to be an excellent tool to quickly gauge the local activation pattern in the adjacency of the recording site. Moreover, its morphology is very sensitive to beat-to-beat changes of activation. However, the morphology of the vector loop of $\boldsymbol{E}$ is influenced by many factors, such as waveform curvature, power line interference and DC offset in the electrograms, relative position of the CNF sensor with respect to the direction of propagation, sensor tilt, and many more. It is therefore difficult to exclusively assess one of these contributions by inspection of the vector loop of $\boldsymbol{E}$.

Electrogram fractionation is also reflected in the vector loop of $\boldsymbol{E}$. Provided that the local activation times of the nonfractionated components are sufficiently different, the individual directions of propagation may be derived from the vector loop of $\boldsymbol{E}$. An approach to separating complex vector loops of $\boldsymbol{E}$ created from fractionated electrograms into simple vector loops by decomposition of the electrograms is presented in Section 7.6.

9.5 Evaluation of Fractionated Electrograms

The basic assumption in the development of algorithms to quantify the fractionation as well as to decompose fractionated electrograms was that such fractionated electrograms emerge from a superposition of nonfractionated components. The number of components,

---

[1] *Transmural* means from the endocardium through the ventricular wall to the epicardium or vice versa.

their amplitudes, and the delay between their LAT's are characteristic parameters of a fractionated electrogram. The developed algorithm *SM* delivers these parameters.

The template-based algorithm *SM* offers a more robust approach to quantifying the presence and degree of fractionation compared to previously applied methods such as a peak counting within the temporal derivative of Φ (algorithm pCt) where the choice of parameters for deciding which peaks to include may cause a significant bias. Further, this novel algorithm allows to detect electrogram fractionation down to smaller differences in LAT's of the wavefront components causing the fractionation. Figure 8.18 shows that the minimum ΔLAT above which two contributing components can be discriminated, i.e. FI=2, increases with z. The minimum ΔLAT that could be resolved was 0.6 ms at $z = 50\,\mu$m, i.e. when both sources were located 50 μm away from the point of observation. The corresponding durations of depolarization of Φ_1 and Φ_2 were $t_{dep1} = t_{dep2} = 0.94\,$ms. Using the pCt method, a minimum ΔLAT of only 1 ms could be resolved. As shown in Figure 8.20, local delays in activation caused by microobstacles can be expected in the range of 0.7 ms which is below the separability threshold of the pCt method, thus underlining the benefits of the *SM* method. Both methods show an increased error in LAT (e_{LAT}) in the range $(\Delta\mathrm{LAT}, z) \approx (0.6\,\mathrm{ms}, 50\,\mu\mathrm{m})$. The reason for this is the assignment of the determined LAT's to the wrong events within the fractionated electrogram, which may occur when peak amplitudes in $\dot{\Phi}$ are very similar.

Although the algorithm *SM* comprises computationally intensive operations like cross correlation, the on-line determination of FI is possible for heart rates of up to 30 Hz (1800 bpm). This enables the examination of FI even during tachycardia in mouse hearts.

9.6 Decomposition of Fractionated Electrograms

Figure 8.19 (d) and (e) demonstrate that with increasing z the minimum ΔLAT for which the errors of B, b, and t_{depm} remain within the given tolerance increases, i.e. the separability decreases. This is due to the broadening of Φ_2 with z, caused by the relative reduction in weight given to local sources. Once a fractionated electrogram is decomposed, the parameters amplitude and duration of depolarization of the decomposed signals may be additional features for the discrimination between local and distant activations. The parameter symmetry factor may allow to discriminate between starting, free running, and terminating/colliding wavefronts. The presented decomposition method enables the estimation of these parameters with satisfactory accuracy, even if they are masked within a fractionated electrogram.

9.6.1 Robustness against Noise

The minimum ΔLAT's in Figure 8.19 (d) and (e) were calculated for noisy waveforms. The respective values for noise-free waveforms (not shown) differ only marginally for the parameters obtained from Φ_{m2} for $z > 200\,\mu$m, i.e. the minimum ΔLAT's are only slightly lower, which suggests that the decomposition method is also well-suited for electrograms recorded under experimental conditions.

9.6.2 Limitations

The decomposition procedure for fractionated electrograms by means of the novel analytic signal model has been developed as a method for detailed analysis of local electrograms during sinus rhythm. The main goal has been to extract information from fractionated electrograms, which allows to elucidate propagation mechanisms and characterize tissue structure at a microscopic scale. The suitability of the methods has been demonstrated for a microscopic size scale. It has not yet been investigated whether the method is applicable to electrograms recorded at a larger size scale, for instance, intracardiac electrograms as recorded with clinical mapping systems. The method has been applied successfully to electrograms recorded experimentally from rabbit atria (see Figure 8.21), however, a careful validation of the decomposition method in an experimental context has not yet been performed.

The most important limiting parameter underlying the presented decomposition method is the time difference ΔLAT between the local activation times of two concurrent activation events relative to their duration of depolarization t_{dep}. When ΔLAT is large enough the decomposition can be achieved more easily by windowing Φ, i.e. by temporal segmentation of the waveform into its components.

Another limiting parameter for a successful decomposition is the maximum value of FI (FI_{max}). In this work, the decomposition has been examined for FI_{max}=3. Although a decomposition is feasible for FI>3, the interpretation of the resulting components is questionable.

9.6.3 Relevance for Electrophysiological Experiments

Pad size and inter-electrode spacing of multielectrode sensor arrays and their distance to the bioelectric sources determine whether or not individual depolarization events can be resolved. The utilized CNF sensors with pad sizes of $18\,\mu$m and inter-electrode spacings of $50\,\mu$m allow to detect the presence of multiple wavefronts in the submillimeter range at a distance $z = 50\,\mu$m away from the tissue surface [54].

From multiple simultaneously recorded electrograms, direction and velocity of propagating wavefronts can be determined in the case of nonfractionated electrograms [62]. The application of the decomposition method to fractionated multivariate CNF signals enables estimating local velocities and directions of each individual nonfractionated component.

Thus, it is expected that parameters obtained by this method allow the following additional characterizations of the microstructure at the recording site:

1) Classification of the microstructural makeup of fibrotic tissue such as a) longitudinally separating inlays of connective tissue, as in patchy fibrosis [22], b) crossing fibers, and c) microscopic obstacles leading to a zig-zag course of propagation.

2) Detection of components representing starting or terminating/colliding wavefronts. Thus, discontinuities in the underlying structure of the tissue, which are considered to be potential sites for unidirectional conduction block [136], may be revealed.

9.7 Discrimination of Local and Distant Activation

The discrimination of local and distant activation within a fractionated electrogram is crucial for the construction of activation maps and for the computation of conduction velocities. In general, no other information about the tissue in the adjacency of the recording site than the electrogram is available. In view of the large variety of possible structural and functional properties of the tissue, it seems unpromising to reconstruct the configuration of current sources or to determine the distance between the recording site and an assumed configuration of current sources.

A different approach to the problem of distinguishing local and distant activation within an electrogram is computing the ratio $\ddot{\Phi}_{pp} : \dot{\Phi}_{pp}$, or $|\dot{\boldsymbol{E}}|_{pp} : |\boldsymbol{E}|_{pp}$ which both fall with increasing distance between current sources and recording site. It had, however, not been examined, if these measures have equal values and fall with the same space constant for different anatomical structures and different patterns of activation.

Figure 8.22 demonstrates that both measures show an exponential decay with increasing distance z from the surface of the tissue, however, with different values for $z = 50\,\mu\mathrm{m}$ and different space constants. Contrary to what was expected, both measures have smaller values for the thicker fiber (cf. blue and green curves in Figure 8.22). The measures are dependent on the conduction velocity, as shown in a simulation of an asymmetric tissue branching with different conductivities (Figure 8.23).

In case of oblique propagation of activation, the tissue branching led to delayed activation of the thick branch and thus fractionated electrograms were recorded between the tissue branches. With neither of the two measures it was possible to distinguish whether a certain deflection within the fractionated electrogram originates from the thick or from the thin tissue branch (see Figure 8.24).

The results of computer simulation and experimental studies clearly demonstrate that both proposed measures are not capable of reliably discriminating local from distant activation. Therefore, any further investigations based only on these measures, like the design of a classifier for local vs. distant activation or an estimator for the distance between current source and recording site, were abandoned.

9.8 Classification of Tissue Microstructure through CNF Signals

The presented computer simulation study is based on a new concept of classifying tissue microstructure through inspection of extracellular electrograms. Fractionation is known to depend not only on the structure of the subjacent tissue but also on the direction of the activation wavefront (cf. Section 3.4.2). Therefore, in order to characterize the microstructure of the tissue under examination, it was assumed that different directions of propagation need to be induced.

The features were selected based on observations during previous computer simulation and experimental studies. Additional features as for instance the LAT dispersion within fractionated electrograms or the symmetry of the electrograms determined by means of the decomposition method presented in Section 7.6 as well as the selection of appropriate features by means of feature ranking algorithms (e.g. [137]) might improve the classification accuracy.

The simple LDA classifier was used because scatter plots of the three-dimensional feature space suggested a good separability by hyperplanes. Nevertheless, other classifiers may lead to a better classification performance.

The leave-one-out method for cross validation was chosen, because in the case of $M = 12$ and $d = 100\,\mu$m, only two samples per class (6 samples in total) were available. Other cross validation methods would presumably deselect all samples of a certain class from the set of training data or test data, respectively, and thus lead to a biased result of classification accuracy. The chosen values for the number of stimulus sites, the grid size, and the number of recording electrodes are considered as technically feasible. Arrays with 32 electrodes with interelectrode spacing of $300\,\mu$m are available (*FlexMEA36; Multichannel Systems*, Reutlingen, Germany).

With regard to the limited number of tissue samples (2 samples per class, 6 samples in total) and the fact that the chosen sections represent clear examples of the respective class, the obtained classification accuracies might be too optimistic. Nevertheless, the results suggest conducting a continuative experimental study.

Chapter 10

Conclusion and Outlook

Cardiac near field technique denotes the acquisition and analysis of local extracellular electrograms at the surface of the heart with high spatial and temporal resolution. Such cardiac near field signals may enable the characterization of the microscopic pattern of activation and thus the identification of regions containing microstructural heterogeneities which are seen as potential substrates for the genesis of arrhythmias. In the following, the main findings presented in this work are summarized.

A robust and accurate method for the computation of magnitude and direction of local conduction velocity (LCV) has been presented. Along with the value of LCV, its uncertainty has been evaluated. Hence, the reliable on-line computation of LCV during electrophysiological experiments has been enabled.

The fractionation index (FI), a quantitative measure representing the degree of fractionation of an electrogram, has been introduced. For the use in template-based CNF signal processing algorithms, an analytic signal model of extracellular electrogram waveform based on sigmoid functions has been developed. A novel approach to analyzing fractionated local electrograms by decomposition into nonfractionated components has been presented.

The computation of the FI by means of an algorithm based on the novel analytic signal model has been realized. This algorithm has been implemented for on-line computation of FI.

The discrimination between local and distant activation reflected within an electrogram has turned out to be unfeasible using measures proposed in the literature.

Finally, based on the observation that fractionation of local electrograms is not only dependent on the microstructure but also on the direction of the activation wavefront, a method for the characterization of microstructure through CNF signals has been presented.

The decomposition method has been evaluated for fractionated local electrograms obtained from computer simulations. In order to validate this method with electrograms recorded during experiments, the assignment of recording positions to the microstructure needs to be enabled. This requires a procedure of generating micrographs from preparations without deforming them. A solution of this problem would also allow the experimental validation of histologically detailed computer models.

The computer simulation study of the classification of different types of fibrosis through CNF signals has yielded promising results. For an experimental study based on the presented findings, two major problems need to be solved. First, heart tissue of different classes of fibrosis is required. Preliminary tests using aged rats or chronic administration of *Cyclosporine A*, an immunosuppressive drug, or *L-NAME*, a nitric oxide inhibitor, have not shown the desired effects. Contrary to the figures presented in literature [138, 139], a significant degree of fibrosis in the treated hearts has not arisen. Second, stimulus electrodes and an array of recording electrodes need to be integrated on a common substrate. Such sensors have been used on a larger size scale [140, 141], however, the requirements on inter-electrode distance and number of electrodes require a new development of a dedicated sensor.

Bibliography

[1] D. Sánchez-Quintana, J. A. Cabrera, J. Farré, V. Climent, R. H. Anderson, and S. Y. Ho. Sinus node revisited in the era of electroanatomical mapping and catheter ablation. *Heart*, 91(2):189–194, Feb 2005.

[2] Mark R Boyett. 'and the beat goes on.' the cardiac conduction system: the wiring system of the heart. *Exp Physiol*, 94(10):1035–1049, Oct 2009.

[3] Oliver Monfredi, Halina Dobrzynski, Tapas Mondal, Mark R Boyett, and Gwilym M Morris. The anatomy and physiology of the sinoatrial node–a contemporary review. *Pacing Clin Electrophysiol*, 33(11):1392–1406, Nov 2010.

[4] J. E. Saffitz, H. L. Kanter, K. G. Green, T. K. Tolley, and E. C. Beyer. Tissue-specific determinants of anisotropic conduction velocity in canine atrial and ventricular myocardium. *Circ Res*, 74(6):1065–1070, Jun 1994.

[5] Harry A Fozzard. The membrane capacitance of heart cells. In Walmor C De Mello, editor, *Electrical Phenomena in the Heart*, Clinical Engineering Series, pages 219–233. Academic Press, New York, 1972.

[6] D. Noble. *The Initiation of the Heartbeat.* Clarendron Press, 2nd edition, 1979.

[7] Bertil Hille. *Ionic channels of excitable membranes.* Sinauer Associates, Sunderland, Massachusetts, 2nd edition, 1992.

[8] Peter Kohl, Christian Bollensdorff, and Alan Garny. Effects of mechanosensitive ion channels on ventricular electrophysiology: experimental and theoretical models. *Exp Physiol*, 91(2):307–321, Mar 2006.

[9] Robert Plonsey and Roger C. Barr. *Bioelectricity; a quantitative approach.* Springer, New York, NY, 3rd edition, 2007.

[10] M. F. Arnsdorf. Basic understanding of the electrophysiologic actions of antiarrhythmic drugs. sources, sinks, and matrices of information. *Med Clin North Am*, 68(5):1247–1280, Sep 1984.

[11] Aman Mahajan, Yohannes Shiferaw, Daisuke Sato, Ali Baher, Riccardo Olcese, Lai-Hua Xie, Ming-Jim Yang, Peng-Sheng Chen, Juan G Restrepo, Alain Karma, Alan Garfinkel, Zhilin Qu, and James N Weiss. A rabbit ventricular action potential model replicating cardiac dynamics at rapid heart rates. *Biophys J*, 94(2):392–410, Jan 2008.

[12] H. T. Shih. Anatomy of the action potential in the heart. *Tex Heart Inst J*, 21(1):30–41, 1994.

[13] F. L. Burton and S. M. Cobbe. Dispersion of ventricular repolarization and refractory period. *Cardiovasc Res*, 50(1):10–23, Apr 2001.

[14] D. Sánchez-Quintana, R. H. Anderson, J. A. Cabrera, V. Climent, R. Martin, J. Farré, and S. Y. Ho. The terminal crest: morphological features relevant to electrophysiology. *Heart*, 88(4):406–411, Oct 2002.

[15] L. Barr, M. M. Dewey, and W. Berger. Propagation of action potentials and the structure of the nexus in cardiac muscle. *J Gen Physiol*, 48:797–823, May 1965.

[16] André G Kléber and Yoram Rudy. Basic mechanisms of cardiac impulse propagation and associated arrhythmias. *Physiol Rev*, 84(2):431–488, Apr 2004.

[17] Miguel Valderrábano. Influence of anisotropic conduction properties in the propagation of the cardiac action potential. *Prog Biophys Mol Biol*, 94(1-2):144–168, 2007.

[18] V. G. Fast and A. G. Kléber. Microscopic conduction in cultured strands of neonatal rat heart cells measured with voltage-sensitive dyes. *Circ Res*, 73(5):914–925, Nov 1993.

[19] Camillo Peracchia. *Biophysics of gap junction channels.* CRC Press, Boca Raton, 1991.

[20] H. J. Jongsma and R. Wilders. Gap junctions in cardiovascular disease. *Circ Res*, 86(12):1193–1197, Jun 2000.

[21] M. S. Spach, W. T. Miller, P. C. Dolber, J. M. Kootsey, J. R. Sommer, and C. E. Mosher. The functional role of structural complexities in the propagation of depolarization in the atrium of the dog. cardiac conduction disturbances due to discontinuities of effective axial resistivity. *Circ Res*, 50(2):175–191, Feb 1982.

[22] Jacques M T de Bakker and Harold M V van Rijen. Continuous and discontinuous propagation in heart muscle. *J Cardiovasc Electrophysiol*, 17(5):567–573, May 2006.

[23] J.J.B. Jack, D. Noble, and R.W. Tsien. *Electric current flow in excitable cells.* Oxford science publications. Clarendon Press, Oxford, 1975.

[24] L. Clerc. Directional differences of impulse spread in trabecular muscle from mammalian heart. *J Physiol*, 255(2):335–346, Feb 1976.

[25] M. S. Spach, W. T. Miller, D. B. Geselowitz, R. C. Barr, J. M. Kootsey, and E. A. Johnson. The discontinuous nature of propagation in normal canine cardiac muscle. evidence for recurrent discontinuities of intracellular resistance that affect the membrane currents. *Circ Res*, 48(1):39–54, Jan 1981.

[26] A. G. Kléber, C. B. Riegger, and M. J. Janse. Electrical uncoupling and increase of extracellular resistance after induction of ischemia in isolated, arterially perfused rabbit papillary muscle. *Circ Res*, 61(2):271–279, Aug 1987.

[27] M. S. Spach and J. M. Kootsey. Relating the sodium current and conductance to the shape of transmembrane and extracellular potentials by simulation: effects of propagation boundaries. *IEEE Trans Biomed Eng*, 32(10):743–755, Oct 1985.

[28] V. G. Fast and A. G. Kléber. Block of impulse propagation at an abrupt tissue expansion: evaluation of the critical strand diameter in 2- and 3-dimensional computer models. *Cardiovasc Res*, 30(3):449–459, Sep 1995.

[29] Sanne de Jong, Toon A B van Veen, Harold V M van Rijen, and Jacques M T de Bakker. Fibrosis and cardiac arrhythmias. *J Cardiovasc Pharmacol*, 57(6):630–638, Jun 2011.

[30] M. S. Spach and J. F. Heidlage. The stochastic nature of cardiac propagation at a microscopic level. electrical description of myocardial architecture and its application to conduction. *Circ Res*, 76(3):366–380, Mar 1995.

[31] H. Windisch, H. Ahammer, P. Schaffer, W. Müller, and D. Platzer. Optical multisite monitoring of cell excitation phenomena in isolated cardiomyocytes. *Pflugers Arch*, 430(4):508–518, Aug 1995.

[32] Vinod Sharma and Leslie Tung. Spatial heterogeneity of transmembrane potential responses of single guinea-pig cardiac cells during electric field stimulation. *J Physiol*, 542(Pt 2):477–492, Jul 2002.

[33] S. Rohr and B. M. Salzberg. Multiple site optical recording of transmembrane voltage (msortv) in patterned growth heart cell cultures: assessing electrical behavior, with microsecond resolution, on a cellular and subcellular scale. *Biophys J*, 67(3):1301–1315, Sep 1994.

[34] S. Rohr, J. P. Kucera, and A. G. Kléber. Slow conduction in cardiac tissue, i: effects of a reduction of excitability versus a reduction of electrical coupling on microconduction. *Circ Res*, 83(8):781–794, Oct 1998.

[35] M. Lavallée, O.F. Schanne, and N.C. Hébert. *Glass microelectrodes*. Wiley, 1969.

[36] M. Novakova, J. Bardonova, I. Provaznik, E. Taborska, H. Bochorakova, H. Paulova, and D. Horky. Effects of voltage sensitive dye di-4-anepps on guinea pig and rabbit myocardium. *Gen Physiol Biophys*, 27(1):45–54, Mar 2008.

[37] H. Windisch, W. Muller, H. Ahammer, and P. Schaffer. Optical micromapping in cardiac tissues and cells. In *Proc. Computers in Cardiology 1993*, pages 137–140, 1993.

[38] P. Schaffer, H. Ahammer, W. Müller, B. Koidl, and H. Windisch. Di-4-anepps causes photodynamic damage to isolated cardiomyocytes. *Pflugers Arch*, 426(6):548–551, Apr 1994.

[39] T. Li, N. Sperelakis, R. E. Teneick, and R. J. Solaro. Effects of diacetyl monoxime on cardiac excitation-contraction coupling. *J Pharmacol Exp Ther*, 232(3):688–695, Mar 1985.

[40] Hao Qin, Matthew W Kay, Nipon Chattipakorn, David T Redden, Raymond E Ideker, and Jack M Rogers. Effects of heart isolation, voltage-sensitive dye, and electromechanical uncoupling agents on ventricular fibrillation. *Am J Physiol Heart Circ Physiol*, 284(5):H1818–H1826, May 2003.

[41] Martin J Bishop, David J Gavaghan, Natalia A Trayanova, and Blanca Rodriguez. Photon scattering effects in optical mapping of propagation and arrhythmogenesis in the heart. *J Electrocardiol*, 40(6 Suppl):S75–S80, 2007.

[42] B. R. Choi and G. Salama. Optical mapping of atrioventricular node reveals a conduction barrier between atrial and nodal cells. *Am J Physiol*, 274(3 Pt 2):H829–H845, Mar 1998.

[43] J. M. Rogers, P. V. Bayly, R. E. Ideker, and W. M. Smith. Quantitative techniques for analyzing high-resolution cardiac-mapping data. *IEEE Engineering in Medicine and Biology Magazine*, 17(1):62–72, 1998.

[44] M. R. Franz. Current status of monophasic action potential recording: theories, measurements and interpretations. *Cardiovasc Res*, 41(1):25–40, Jan 1999.

[45] Masahiko Kondo, Vladislav Nesterenko, and Charles Antzelevitch. Cellular basis for the monophasic action potential. which electrode is the recording electrode? *Cardiovasc Res*, 63(4):635–644, Sep 2004.

[46] P. Colli Franzone, L. F. Pavarino, S. Scacchi, and B. Taccardi. Monophasic action potentials generated by bidomain modeling as a tool for detecting cardiac repolarization times. *Am J Physiol Heart Circ Physiol*, 293(5):H2771–H2785, Nov 2007.

[47] Michael R Franz. What is a monophasic action potential recorded by the franz contact electrode? *Cardiovasc Res*, 65(4):940–1; author reply 942–4, Mar 2005.

[48] Edward J Vigmond. The electrophysiological basis of map recordings. *Cardiovasc Res*, 68(3):502–503, Dec 2005.

[49] Igor R Efimov, Vladimir P Nikolski, and Guy Salama. Optical imaging of the heart. *Circ Res*, 95(1):21–33, Jul 2004.

[50] R. A. Malkin and B. D. Pendley. Construction of a very high-density extracellular electrode array. *Am J Physiol Heart Circ Physiol*, 279(1):H437–H442, Jul 2000.

[51] J. J. Mastrototaro, H. Z. Massoud, T. C. Pilkington, and R. E. Ideker. Rigid and flexible thin-film multielectrode arrays for transmural cardiac recording. *IEEE Trans Biomed Eng*, 39(3):271–279, Mar 1992.

[52] E. Hofer, G. Urban, M. S. Spach, I. Schafferhofer, G. Mohr, and D. Platzer. Measuring activation patterns of the heart at a microscopic size scale with thin-film sensors. *Am J Physiol*, 266(5 Pt 2):H2136–H2145, May 1994.

[53] G. Mohr, E. Hofer, and G. Plank. A new real-time mapping system to detect microscopic cardiac excitation patterns. *Biomed Instrum Technol*, 33(5):455–461, 1999.

[54] E. Hofer, F. Keplinger, T. Thurner, T. Wiener, D. Sánchez-Quintana, V. Climent, and G. Plank. A new floating sensor array to detect electric near fields of beating heart preparations. *Biosensors & bioelectronics*, 21(12):2232–2239, Jun 15 2006.

[55] Koonlawee Nademanee, John McKenzie, Erol Kosar, Mark Schwab, Buncha Sunsaneewitayakul, Thaveekiat Vasavakul, Chotikorn Khunnawat, and Tachapong Ngarmukos. A new approach for catheter ablation of atrial fibrillation: mapping of the electrophysiologic substrate. *J Am Coll Cardiol*, 43(11):2044–2053, Jun 2004.

[56] Li-Wei Lo and Shih-Ann Chen. Three-dimensional electroanatomic mapping systems in catheter ablation of atrial fibrillation. *Circ J*, 74(1):18–23, Jan 2010.

[57] F. M. Weber, C. Schilling, G. Seemann, A. Luik, C. Schmitt, C. Lorenz, and O. Dössel. Wave-direction and conduction-velocity analysis from intracardiac electrograms–a single-shot technique. *IEEE Trans Biomed Eng*, 57(10):2394–2401, 2010.

[58] Gunnar Seemann. *Modeling of Electrophysiology and Tension Development in the Human Heart.* Universitätsverlag Karlsruhe, 2005.

[59] Rodrigo Weber dos Santos, Gernot Plank, Steffen Bauer, and Edward J Vigmond. Parallel multigrid preconditioner for the cardiac bidomain model. *IEEE Trans Biomed Eng*, 51(11):1960–1968, Nov 2004.

[60] Gernot Plank, Manfred Liebmann, Rodrigo Weber dos Santos, Edward J Vigmond, and Gundolf Haase. Algebraic multigrid preconditioner for the cardiac bidomain model. *IEEE Trans Biomed Eng*, 54(4):585–596, Apr 2007.

[61] J.P. Keener and J. Sneyd. *Mathematical physiology: Systems physiology.* Interdisciplinary applied mathematics. Springer, 2nd edition, 2009.

[62] G. Plank and E. Hofer. Model study of vector-loop morphology during electrical mapping of microscopic conduction in cardiac tissue. *Annals of Biomedical Engineering*, 28(10):1244–1252, 2000.

[63] F. X. Witkowski, K. M. Kavanagh, P. A. Penkoske, and R. Plonsey. In vivo estimation of cardiac transmembrane current. *Circ Res*, 72(2):424–439, Feb 1993.

[64] M. S. Spach, R. C. Barr, G. A. Serwer, J. M. Kootsey, and E. A. Johnson. Extracellular potentials related to intracellular action potentials in the dog purkinje system. *Circ Res*, 30(5):505–519, May 1972.

[65] B. M. Steinhaus. Estimating cardiac transmembrane activation and recovery times from unipolar and bipolar extracellular electrograms: a simulation study. *Circ Res*, 64(3):449–462, Mar 1989.

[66] M. S. Spach and P. C. Dolber. Relating extracellular potentials and their derivatives to anisotropic propagation at a microscopic level in human cardiac muscle. evidence for electrical uncoupling of side-to-side fiber connections with increasing age. *Circ Res*, 58(3):356–371, Mar 1986.

[67] B. B. Punske, Q. Ni, R. L. Lux, R. S. MacLeod, P. R. Ershler, T. J. Dustman, M. J. Allison, and B. Taccardi. Spatial methods of epicardial activation time determination in normal hearts. *Annals of Biomedical Engineering*, 31(7):781–792, Jul-Aug 2003.

[68] D. B. Geselowitz, P. E. Crombie, S. M. Smith, and E. J. Berbari. Use of surface laplacian to extract local activation from epicardial electrograms. In *Proc. Computers in Cardiology 1996*, pages 129–132, 1996.

[69] G. Plank and E. Hofer. Use of cardiac electric near-field measurements to determine activation times. *Annals of Biomedical Engineering*, 31(9):1066–1076, Oct 2003.

[70] W. S. Ellis, S. J. Eisenberg, D. M. Auslander, M. W. Dae, A. Zakhor, and M. D. Lesh. Deconvolution: a novel signal processing approach for determining activation time from fractionated electrograms and detecting infarcted tissue. *Circulation*, 94(10):2633–2640, Nov 1996.

[71] I. Chouvarda, N. Maglaveras, J. M. de Bakker, F. J. van Capelle, and C. Pappas. Deconvolution and wavelet-based methods for membrane current estimation from simulated fractionated electrograms. *IEEE Trans Biomed Eng*, 48(3):294–301, Mar 2001.

[72] R. M. Shaw and Y. Rudy. Ionic mechanisms of propagation in cardiac tissue. roles of the sodium and l-type calcium currents during reduced excitability and decreased gap junction coupling. *Circ Res*, 81(5):727–741, Nov 1997.

[73] J. P. Kucera and Y. Rudy. Mechanistic insights into very slow conduction in branching cardiac tissue: a model study. *Circ Res*, 89(9):799–806, Oct 2001.

[74] R. Cabot. A note on the application of the hilbert transform to time delay estimation. *IEEE Trans Acoust Speech Signal Process*, 29(3):607–609, 1981.

[75] S. M. Shors, A. V. Sahakian, H. J. Sih, and S. Swiryn. A method for determining high-resolution activation time delays in unipolar cardiac mapping. *IEEE Trans Biomed Eng*, 43(12):1192–1196, Dec 1996.

[76] T. Wiener, T. Thurner, A. J. Prassl, G. Plank, and E. Hofer. Accuracy of local conduction velocity determination from non-fractionated cardiac activation signals. *Conference proceedings: 29th Annual International Conference of the IEEE Engineering in Medicine and Biology Society.*, 2007:27–30, 2007.

[77] F. X. Witkowski, K. M. Kavanagh, P. A. Penkoske, and R. Plonsey. Epicardial cardiac source-field behavior. *IEEE Trans Biomed Eng*, 42(6):552–558, Jun 1995.

[78] A. H. Kadish, J. F. Spear, J. H. Levine, R. F. Hanich, C. Prood, and E. N. Moore. Vector mapping of myocardial activation. *Circulation*, 74(3):603–615, Sep 1986.

[79] G. Plank, M. Monserrat, J. Saiz, and E. Hofer. Computer simulation of electric fields at the junction terminal crest -pectinate muscle. In *Proc. Computers in Cardiology*, pages 497–499, 2002.

[80] G. Plank, E. Vigmond, L. J. Leon, and E. Hofer. Cardiac near-field morphology during conduction around a microscopic obstacle–a computer simulation study. *Annals of Biomedical Engineering*, 31(10):1206–1212, Nov 2003.

[81] E. Hofer, T. Wiener, A. J. Prassl, T. Thurner, and G. Plank. Oblique propagation of activation allows the detection of uncoupling microstructures from cardiac near field behavior. *Conference proceedings: 29th Annual International Conference of the IEEE Engineering in Medicine and Biology Society.*, 2007:415–418, 2007.

[82] E. Hofer, D. Sanchez-Quintana, G. Plank, and M. Tischler. Normal and fractionated cardiac near fields and their relation to microstructure - an experimental approach. In *Proc. 25th Annual Int Engineering in Medicine and Biology Society Conf. of the IEEE*, volume 1, pages 51–54, 2003.

[83] C. K. Millar, F. A. Kralios, and R. L. Lux. Correlation between refractory periods and activation-recovery intervals from electrograms: effects of rate and adrenergic interventions. *Circulation*, 72(6):1372–1379, Dec 1985.

[84] S. Scacchi, P. Colli Franzone, L. F. Pavarino, and B. Taccardi. A reliability analysis of cardiac repolarization time markers. *Math Biosci*, 219(2):113–128, Jun 2009.

[85] Edward J Vigmond, Vincent Tsoi, Yalin Yin, Pierre Pagé, and Alain Vinet. Estimating atrial action potential duration from electrograms. *IEEE Trans Biomed Eng*, 56(5):1546–1555, May 2009.

[86] Vincent Jacquemet and Craig S Henriquez. Genesis of complex fractionated atrial electrograms in zones of slow conduction: a computer model of microfibrosis. *Heart Rhythm*, 6(6):803–810, Jun 2009.

[87] Jacques M T de Bakker and Fred H M Wittkampf. The pathophysiologic basis of fractionated and complex electrograms and the impact of recording techniques on their detection and interpretation. *Circ Arrhythm Electrophysiol*, 3(2):204–213, Apr 2010.

[88] M. A. McGuire, J. M. de Bakker, J. T. Vermeulen, T. Opthof, A. E. Becker, and M. J. Janse. Origin and significance of double potentials near the atrioventricular node. correlation of extracellular potentials, intracellular potentials, and histology. *Circulation*, 89(5):2351–2360, May 1994.

[89] H. L. Waxman and R. J. Sung. Significance of fragmented ventricular electrograms observed using intracardiac recording techniques in man. *Circulation*, 62(6):1349–1356, Dec 1980.

[90] K. T. Konings, J. L. Smeets, O. C. Penn, H. J. Wellens, and M. A. Allessie. Configuration of unipolar atrial electrograms during electrically induced atrial fibrillation in humans. *Circulation*, 95(5):1231–1241, Mar 1997.

[91] M. S. Spach, R. C. Barr, E. A. Johnson, and J. M. Kootsey. Cardiac extracellular potentials. analysis of complex wave forms about the purkinje networks in dogs. *Circ Res*, 33(4):465–473, Oct 1973.

[92] M. E. Josephson and A. L. Wit. Fractionated electrical activity and continuous electrical activity: fact or artifact? *Circulation*, 70(4):529–532, Oct 1984.

[93] W. S. Ellis, D. M. Auslander, and M. D. Lesh. Fractionated electrograms from a computer model of heterogeneously uncoupled anisotropic ventricular myocardium. *Circulation*, 92(6):1619–1626, Sep 1995.

[94] P. I. Gardner, P. C. Ursell, J. J. Fenoglio, and A. L. Wit. Electrophysiologic and anatomic basis for fractionated electrograms recorded from healed myocardial infarcts. *Circulation*, 72(3):596–611, Sep 1985.

[95] Koonlawee Nademanee, Evan Lockwood, Naoya Oketani, and Brett Gidney. Catheter ablation of atrial fibrillation guided by complex fractionated atrial electrogram mapping of atrial fibrillation substrate. *J Cardiol*, 55(1):1–12, Jan 2010.

[96] Daniel Scherr, Darshan Dalal, Aamir Cheema, Alan Cheng, Charles A Henrikson, David Spragg, Joseph E Marine, Ronald D Berger, Hugh Calkins, and Jun Dong. Automated detection and characterization of complex fractionated atrial electrograms in human left atrium during atrial fibrillation. *Heart Rhythm*, 4(8):1013–1020, Aug 2007.

[97] V. Křemen, L. Lhotská, M. Macaš, R. Čihák, V. Vančura, J. Kautzner, and D. Wichterle. A new approach to automated assessment of fractionation of endocardial electrograms during atrial fibrillation. *Physiol Meas*, 29(12):1371–1381, Dec 2008.

[98] Kurt C Roberts-Thomson, Peter M Kistler, Prashanthan Sanders, Joseph B Morton, Haris M Haqqani, Irene Stevenson, Jitendra K Vohra, Paul B Sparks, and Jonathan M Kalman. Fractionated atrial electrograms during sinus rhythm: relationship to age, voltage, and conduction velocity. *Heart Rhythm*, 6(5):587–591, May 2009.

[99] Robert Arnold, Thomas Wiener, Thomas Thurner, and Ernst Hofer. A novel electrophysiological measurement system to study rapidly paced animal hearts. In *IFMBE Proceedings*, volume 22 of *9*, pages 1145–1148. 4th European Conference of the International Federation for Medical and Biological Engineering, Springer, 2009.

[100] Ernst Hofer, Thomas Wiener, and Robert Arnold. A novel transillumination device allows improved resolution in recon-struction of surface electrode positions with car-

diac tissue topology. In *Proceedings of the 45th annual conference of the german society of biomedical engineering*, 2011.

[101] L. A. Geddes. *Electrodes and the measurement of bioelectric events.* Wiley-Interscience, New York, 1972.

[102] Robert Arnold, Thomas Wiener, and Ernst Hofer. Novel system for stimulation and analysis of cardiac excitation spread under hindered conduction conditions. In *Biomedizinische Technik / Biomedical Engineering - Proceedings*. Walter de Gruyter, 2010.

[103] J. A. Cabrera, D. Sánchez-Quintana, S. Y. Ho, A. Medina, and R. H. Anderson. The architecture of the atrial musculature between the orifice of the inferior caval vein and the tricuspid valve: the anatomy of the isthmus. *J Cardiovasc Electrophysiol*, 9(11):1186–1195, Nov 1998.

[104] J. E. Olgin, J. M. Kalman, A. P. Fitzpatrick, and M. D. Lesh. Role of right atrial endocardial structures as barriers to conduction during human type i atrial flutter. activation and entrainment mapping guided by intracardiac echocardiography. *Circulation*, 92(7):1839–1848, Oct 1995.

[105] J. A. Cabrera, D. Sanchez-Quintana, J. Farre, J. M. Rubio, and S. Y. Ho. The inferior right atrial isthmus: further architectural insights for current and coming ablation technologies. *J Cardiovasc Electrophysiol*, 16(4):402–8, 2005.

[106] Günther Mohr. *Meßsystem zur Echtzeitdarstellung komplexer kardialer Ausbreitungsvorgänge.* PhD thesis, Graz University of Technology, 1998.

[107] H.J. Döring and H. Dehnert. *The isolated perfused warm-blooded heart according to Langendorff.* Methods in experimental physiology and pharmacology. Biomesstechnik-Verlag March, 1988.

[108] Robert Arnold. Dll-wrapper für canon edsdk/ labview-applikation zur steuerung einer canon eos 5d markii. Technical report, Institute of Biophysics, Medical University of Graz, 2009.

[109] Edward J Vigmond, Matt Hughes, G. Plank, and L. Joshua Leon. Computational tools for modeling electrical activity in cardiac tissue. *J Electrocardiol*, 36 Suppl:69–74, 2003.

[110] A.R. Webb. *Statistical pattern recognition.* Wiley, 2nd edition, 2002.

[111] W. J. Karlon, J. W. Covell, A. D. McCulloch, J. J. Hunter, and J. H. Omens. Automated measurement of myofiber disarray in transgenic mice with ventricular expression of ras. *Anat Rec*, 252(4):612–625, Dec 1998.

[112] Fernando O Campos, Thomas Wiener, Anton J Prassl, Helmut Ahammer, Gernot Plank, Rodrigo Weber Dos Santos, Damián Sánchez-Quintana, and Ernst Hofer. A 2d-computer model of atrial tissue based on histographs describes the electro-anatomical impact of microstructure on endocardiac potentials and electric near-fields. *Conf Proc IEEE Eng Med Biol Soc*, 2010:2541–2544, 2010.

[113] MATLAB. *version 7.8.0 (R2009a)*. The MathWorks Inc., Natick, Massachusetts, 2009.

[114] A. Schlögl and C. Brunner. Biosig: A free and open source software library for bci research. *Computer*, 41(10):44–50, 2008.

[115] Mario Bellina. Charakterisierung eines meßverstärkersystems zur in vitro messung kardialer erregungsausbreitung. Technical report, Institute of Medical Engineering, Graz University of Technology, 2009.

[116] Susan M. Blanchard, Ralph J. Damiano, Tetsuo Asano, William M. Smith, Raymond E. Ideker, and James E. Lowe. The effects of distant cardiac electrical events on local activation in unipolar epicardial electrograms. *IEEE Trans Biomed Eng*, 34(7):539–546, 1987.

[117] R. J. Damiano, S. M. Blanchard, T. Asano, J. L. Cox, and J. E. Lowe. Effects of distant potentials on unipolar electrograms in an animal model utilizing the right ventricular isolation procedure. *J Am Coll Cardiol*, 11(5):1100–1109, May 1988.

[118] Ernst Hofer, Ingrid Schafferhofer, Günther Mohr, and Gerald Urban. The discrimination of electrically uncoupled cardiac events by means of a subminiature electrode-array. In P.W. Mactarlane J. Liebman, editor, *Electrocardiology 1996: From the Cell to the Body Surface - Proceedings of the 23rd International Congress on Electrocardiology, Cleveland, Ohio, 31 July-4 August 1996*, pages 109–112. World Scientific, 1997.

[119] I. Chouvarda, N. Maglaveras, C. Pappas, F. J L VAN Capelle, and J. DeBakker. Estimation of distance between a unipolar recording electrode and a myocardial bundle based on signal characteristics. *Ann Biomed Eng*, 32(10):1336–1347, Oct 2004.

[120] T. Kawara, R. Derksen, J. R. de Groot, R. Coronel, S. Tasseron, A. C. Linnenbank, R. N. Hauer, H. Kirkels, M. J. Janse, and J. M. de Bakker. Activation delay after premature stimulation in chronically diseased human myocardium relates to the architecture of interstitial fibrosis. *Circulation*, 104(25):3069–3075, Dec 2001.

[121] Wiebe R. Pestmann. *Mathematical Statistics*. Walter de Gruyter, Berlin, New York, 2nd edition, 2009.

[122] Alan V. Oppenheim, Ronald W. Schafer, and John R. Buck. *Discrete-time signal processing.* Prentice-Hall, Inc., Upper Saddle River, NJ, USA, 2nd edition, 1999.

[123] P.M. Djuric and S.M. Kay. Spectrum estimation and modeling. In V.K. Madisetti and D.B. Williams, editors, *Digital Signal Processing Handbook.* CRC Press LLC, Boca Raton, 1999.

[124] C. S. Henriquez, N. Trayanova, and R. Plonsey. Potential and current distributions in a cylindrical bundle of cardiac tissue. *Biophys J*, 53(6):907–918, Jun 1988.

[125] Richard G. Lyons. *Understanding Digital Signal Processing.* Prentice Hall, Upper Saddle River, NJ, 2nd edition, 2004.

[126] D. S. Lindblad, C. R. Murphey, J. W. Clark, and W. R. Giles. A model of the action potential and underlying membrane currents in a rabbit atrial cell. *Am J Physiol*, 271(4 Pt 2):H1666–H1696, Oct 1996.

[127] J. P. Drouhard and F. A. Roberge. A simulation study of the ventricular myocardial action potential. *IEEE Trans Biomed Eng*, 29(7):494–502, Jul 1982.

[128] Thomas Wiener, Fernando O. Campos, Gernot Plank, and Ernst Hofer. Decomposition of fractionated local electrograms using an analytic signal model based on sigmoid functions. *submitted to Biomed Tech*, x:x, 2012.

[129] Thomas Wiener, Fernando O. Campos, and Ernst Hofer. Cardiac electric near field behavior at sites of complex microstructure and during wave collision. In *Biomedizinische Technik / Biomedical Engineering - Proceedings.* Walter de Gruyter, 2010.

[130] R.O. Duda, P.E. Hart, and D.G. Stork. *Pattern classification.* Pattern Classification and Scene Analysis: Pattern Classification. Wiley, 2001.

[131] C.M. Bishop. *Pattern recognition and machine learning.* Information science and statistics. Springer, 2006.

[132] A. Schlögl, J. Kronegg, J.E. Huggins, and S.G. Mason. Evaluation criteria for bci research. In G. Dornhege, editor, *Toward brain-computer interfacing*, pages 327–342. The MIT Press, 2007.

[133] A. Brandt. *Noise and Vibration Analysis: Signal Analysis and Experimental Procedures.* John Wiley & Sons, 2011.

[134] B. K. van Veen, H. Wolters, W. Wallinga, W. L. Rutten, and H. B. Boom. The bioelectrical source in computing single muscle fiber action potentials. *Biophys J*, 64(5):1492–1498, May 1993.

[135] B. Widrow and S.D. Stearns. *Adaptive signal processing.* Prentice-Hall signal processing series. Prentice-Hall, 1985.

[136] V. G. Fast and A. G. Kléber. Cardiac tissue geometry as a determinant of unidirectional conduction block: assessment of microscopic excitation spread by optical mapping in patterned cell cultures and in a computer model. *Cardiovasc Res*, 29(5):697–707, May 1995.

[137] Hanchuan Peng, Fuhui Long, and C. Ding. Feature selection based on mutual information criteria of max-dependency, max-relevance, and min-redundancy. *IEEE Trans Pattern Anal Mach Intell*, 27(8):1226–1238, 2005.

[138] Alessandra Stacchiotti, Francesca Bonomini, Antonio Lavazza, Luigi Fabrizio Rodella, and Rita Rezzani. Adverse effects of cyclosporine a on hsp25, alpha b-crystallin and myofibrillar cytoskeleton in rat heart. *Toxicology*, 262(3):192–198, Aug 2009.

[139] O. Pechánová, I. Bernátová, V. Pelouch, and P. Babál. L-name-induced protein remodeling and fibrosis in the rat heart. *Physiol Res*, 48(5):353–362, 1999.

[140] E. Macchi, M. Cavalieri, D. Stilli, E. Musso, S. Baruffi, G. Olivetti, P. R. Ershler, R. L. Lux, and B. Taccardi. High-density epicardial mapping during current injection and ventricular activation in rat hearts. *Am J Physiol*, 275(5 Pt 2):H1886–H1897, Nov 1998.

[141] Stefano Rossi, Silvana Baruffi, Andrea Bertuzzi, Michele Miragoli, Domenico Corradi, Roberta Maestri, Rossella Alinovi, Antonio Mutti, Ezio Musso, Andrea Sgoifo, Donatella Brisinda, Riccardo Fenici, and Emilio Macchi. Ventricular activation is impaired in aged rat hearts. *Am J Physiol Heart Circ Physiol*, 295(6):H2336–H2347, Dec 2008.